LI-S BATTERIES CATHODE AND ANODE WITH FUNCTIONALIZED CARBON NANOTUBE SPONGES

A Dissertation

by

JIAN TAN

Submitted to the Graduate and Professional School of
Texas A&M University
in partial fulfillment of the requirements for the degree of

DOCTOR OF PHILOSOPHY

Chair of Committee,	Choongho Yu
Co-Chair of Committee,	
Committee Members,	Perla B. Balbuena
	Ying Li
	Matt Pharr
Head of Department,	Bryan Rasmussen

May 2022

Major Subject: Mechanical Engineering

ABSTRACT

Lithium-ion batteries are widely used in portable electronics, electrical vehicle, stational power grid and many other applications, owing to the high energy density, high power density and good cyclability. The rapidly increasing demand for advanced energy storage system has motivated the research community to deliver the next-generation battery system beyond the Li-ion batteries (LIB) because LIB have reached the theoretical limit of the power and energy density. Li-S batteries have a higher theoretical capacity based on sulfur (1675mAh/g) and a higher energy density (2567 Wh/kg), benefiting from the conversion-type cathode material compared to the intercalation-type of traditional Li-ion battery cathode. Besides better energy storage performances, the low-cost raw material (sulfur) makes Li-S batteries the very promising candidate beyond LIB system. LIB which requires expensive metals, such as cobalt, titanium, nickel. Introducing of polysulfide anchoring materials provided a potential solution to the practical application of lithium sulfur battery. However, the practical application of Li-S batteries is impeded by several drawbacks including insulating sulfur/polysulfides deposited on the surface of electrodes, polysulfide shuttle in electrolytes, volume expansion while charging and discharging, lithium dendrites. Carbonaceous material has been considered as a promising candidate for LSB scaffold attribute to the outstanding electrochemical stability, electrical conductivity and mechanical strength.

This research starts with improving the performance of lithium-sulfur battery by introducing functional sites on the CNT with mechano-chemical treatment. Combining

with lithium-infused anode, the cell exhibited a strikingly high areal capacity as high as 13.3 mAh/cm^2 at an areal current density of 1.6 mAh/cm^2, and maintained at 11.0 mAh/cm^2. Furthermore, MnO_2 decorated CNT anode was proposed to alleviate lithium dendrite formation on the electrode surface. In-operando and DFT calculation has shown that lithiophilic particle embedded in the porous and conductive medium could effectively suppress the lithium dendrite formation. The functionalized anode shows outstanding accumulative capacity over 10,000 mAh^2/cm^2, which considers both cycling lifetime and areal capacity, even with large Li plating/stripping capacity of 6 mAh/cm^2 for more than 1800 hours. Additionally, parameters of lithium sulfur battery are investigated with experiments and simulation. The thickness-dependent study shows that thickness need to be carefully selected to avoid polarization, especially on high c-rate. The limitation factors for thick electrode, with high loading and high c-rate are investigated. The findings provide a methodology to optimize the performance of rate-capability, cycling life, and loading of active material.

ACKNOWLEDGEMENTS

I would like to thank my committee chair, Dr. Yu, and my committee members, Dr. Balbuena, Dr. Li, and Dr. Pharr, for their guidance and support throughout the course of this research.

Thanks also go to my friends and colleagues and the department faculty and staff for making my time at Texas A&M University a great experience.

Finally, thanks to my mother and father for their encouragement, patience and love.

CONTRIBUTORS AND FUNDING SOURCES

Contributors

This work was supervised by a dissertation committee consisting of Professor Choongho Yu [advisor], Ying Li and Matt Pharr of the Department of Mechanical Engineering and Professor Perla B. Balbuena of the Department of Chemical Engineering.

The analyses depicted in Chapter 4.2 were conducted in part by Professor Perla B. Balbuena and Dr. Fernando A. Soto of the Department of Chemical Engineering and being prepared for publication.

All other work conducted for the thesis (or) dissertation was completed by the student independently.

Funding Sources

Graduate study was supported by a fellowship from Texas A&M University.

This work was also made possible in part by NSF under Grant Number [insert grant number]. Its contents are solely the responsibility of the authors and do not necessarily represent the official views of the [name of awarding office].

TABLE OF CONTENTS

Page

LIST OF FIGURES

Page

1. INTRODUCTION

Lithium sulfur battery (LSB) has attracted wide attention due to its high energy density and power, but severe polysulfide shuttle effect and lithium dendrite formations on lithium (Li) metal anode have been the major hurdles for practical application of LSB. This research starts with performance-oriented exploration, followed by direct observation of electrode evolution and theoretical simulation, finally proposed electrode design with improved performance. A novel mechano-chemical method was proposed to create trenches on the surface of carbon nanotubes (CNTs) in free-standing 3D porous CNT sponges without collapsing their structures. Our Li-S cells made by the manufacturing-friendly sulfur-sandwiched cathode and lithium-infused anode using the mechano-chemically treated electrodes exhibited a strikingly high areal capacity as high as 13.3 mAh cm-2, which was only marginally reduced even with ten-fold increase in the current density (16 mA cm-2), demonstrating both high “cell-level” energy density and power (or fast charge/discharge). In order to investigate the failure/degradation mechanisms and limiting factors of our lithium sulfur (Li-S) batteries, in-operando study of Li-S batteries has been conducted for direct observation of end product nucleation and lithium dendrite formation, analysis of polysulfide shuttling and adsorption while battery is being discharged and charged. A multi-scale computational methodology is developed to optimize the morphology of the pores and surface area of the cathode. In-operando observation is conducted to validate the computational result. We finally present a stable, long-cycle-life Li metal anode enabled by a MnO2-functionalized 3D porous CNT framework (MO-CNT). The MO-CNT offered a large specific capacity as high as

3089 mAh/g and a very long cycle for more than 1875 hours even at a high areal capacity of 6 mAh/cm^2.

1.1. Current Development of Lithium Sulfur Battery

Sustainable and clean energy solutions become increasingly important in the modern society. Converting energy from renewable energy sources such as wind and solar energy has been regarded as a promising substitute for fossil fuels. Storing the clean energy in the electrical form is the most effective way for practical use. As electric vehicles are expected to be popular near future to replace automobiles with internal combustion engines, efficient electrical energy storage systems with high energy density are in urgent need. Rechargeable batteries stand out for this option due to their high energy density and long cycle life. Li-ion batteries have enabled revolution in portable electronics since their introduction in 1991. The current Li-ion batteries have been improved to a level of performance close to their theoretical limit, but the energy density of Li-ion batteries is still too low to meet the high demand from the market. New battery chemistry with much higher energy densities have been recently suggested. Among them, Li-S batteries are believed to be the best candidate for practical use near future. Although impressive results for Li-S batteries have been reported in literature, none of them has been commercialized mainly because of either complicated synthesis/manufacturing processes or low areal loadings of sulfur (active cathode material). The former undermines the benefit of reduced cost resulting from inexpensive sulfur, while the latter would give rise to low actual energy density (i.e., low cell-level energy density rather than energy density per sulfur). In summary, the poor cyclability

and cell-level energy density, especially at strict testing conditions, hindered the commercial application of LSB at current stage.

Development of LSB is challenging by several issues. 1) Large portion of host material is needed to ensure fast conversion between S and Li_2S, alleviate polysulfide shuttling effect, and guarantee enough surface area for even distribution of active material. 2) Excessive amount of electrolyte is required in lab-scale research, which is not applicable in the industry. Mass of electrolyte is considered "dead" weight of the system since it has no direct contribution to energy storage. 3) Safety problems also arise due to application of flammable and volatile ether-based electrolyte, and highly active lithium metal anode. Failure mechanism of lithium metal has been widely reported. Short-circuit caused by dendrite formation is extremely dangerous for LSB when applying on electrical vehicle and portable electronics. If lithium metal is unavoidable for LSB, an anode with mild, predictable, safe failing process is urgently needed. 4) Cycling of LSB involve large volume expansion on anode and cathode. Mechanical properties of the electrode need to be well-considered to avoid cracking and pulverization.

Carbon-based materials have been considered as an ideal framework material for LSB due to its high electrical conductivity, adequate pore volume, and strong mechanical properties. Carbon nanotubes (CNT) with micro-meso-porous structure could provide large polysulfides storage space. Super-aligned carbon nanotubes shows outstanding performance due to straight tunnel for fast ion diffusion and short path for charge transfer.[1-3] Binder-free, highly conductive, and flexible LSB cathode can be

synthesized by carbonizing polyacrylonitrile (PAN).[4] However, the CNT has weak interaction with polysulfides since it is dominated by van der Waals force.

Beyond engineering the morphology, CNT is versatile to embed functional group for better adsorption of polysulfides. Numerous functional groups have been reported to enhance polysulfide retention and electrochemical kinetics, including heteroatoms, redox mediators, metal oxide, etc. Acid-treatment of CNT could generate uniformly distributed oxygen-containing functional groups, such as hydroxyl group, carbonyl group, carboxyl group, etc. Yang, et al, reported a trench-wall feature created by mechano-chemical method, which works effectively as polysulfide reservoir for high loading and high current density LSB.[5] Vacuum filtration has been reported as an effective way to grafted oxygen-containing group on CNT.[6] High adsorption to polysulfides is attributed to a strong covalent bond between sulfur and functionalized CNT. Other than oxygen-containing group, nitrogen-doped CNT drew wide attention, benefitting from the formation of pyridine nitrogen, pyrrole nitrogen and graphite nitrogen. The nitrogen-doped CNT attract polysulfide through dipole-dipole interaction.[7-9] Deng, et al, reported amorphous Al_2O_3 embedded on nitrogen-doped porous CNT by carbonizing MOF-Al. The electrode shows higher electrical conductivity, faster lithium ionic diffusion, and improved charge transfer, resulting it low capacity decay.[10] Catalytic material attracted a lot of attention, not only attribute to the good adsorption to polysulfide, but also improved electrochemical kinetics. MnO_3 can be synthesized on CNT with facile hydrothermal method.[11] MnO_3 shows good polysulfides adsorption and promoted kinetics. Especially in lean electrolyte condition, electrocatalysis can interact with

polysulfide to form thiosulfate-polysulfide complexes.[12-18] VO_2 could oxidize polysulfides to thiosulfates without forming electrochemically inactive sulfate, according to Liang et al.[17] Thiosulfate formation could be promoted by metal oxide when its redox potential lies just above the redox voltage of polysulfide.[17] Otherwise, the oxide might over-oxidize to generate inactive sulfate group and weak polar interaction. Cobalt sulfides has been demonstrated to improve the cycling stability.[19] Main advantages of utilization these additives is to enhance reactions kinetics of converting high order polysulfide to lower order counterparts. Fast conversion could result in precipitated end product, thus anchor the active material in cathode. However, not all the metal oxides are applicable as catalyst since strong adsorption could result it surface passivation and over-oxidation.[20]

Metal-organic framework (MOF) shows interesting performance as an additive in carbon-based material.[21-24] MOF reveals a great potential in tackling the challenges of polysulfide shuttling effect, benefitting from its abundant porosity, high surface area, and strong interaction to polysulfides.[25-27] However, the poor electrical conductivity of MOF still hinders the wide application of such material in energy storage devices. Stability, crystallinity, and pore tunability are greatly improved according recent reports.[28] Mao et al. presented a hierarchical porous structure, combining MOFs and CNT thin film, as flexible Li-S electrode. The interaction between positively charged open metal sites in MOF and negatively charged polysulfides is facilitated by electrostatic attraction. Additionally, the CNT thin film as conductive framework shows good flexibility.

1.2. In-operando Observation of Li-S Battery

Extensive research has been conducted on LSB system. Traditionally, electrochemical techniques are widely used to study the reaction mechanism, including cyclic voltammetry (CV), galvanostatic discharge/charge cycling, electrochemical impedance spectroscopy (EIS), galvanostatic intermittent titration technique, etc. However, these techniques only establish the outcome of design philosophy, while it is very difficult to clearly find out how the reaction progresses while the cell is being discharge/charged. It is essential to understand how polysulfide is distributed while cycling, how Li is being deposited on anode, and the mechanism of capacity degradation. Especially when designing porous Li metal anode, it is essential to observe how Li is inserted into the porous structures with conventional coin cells or pouch cells. Numerous ex situ techniques have been devoted to investigate the characteristics of the battery, such as scanning electron microscopy (SEM), energy-dispersive x-ray spectroscopy (EDS), transmission electron microscopy (TEM), X-ray diffraction (XRD), etc. Inspection after disassembling these cells has provided only fragmentary information at that particular point. The morphology changes, chemical state variation, volume expansion at different cycling stages are hard to inspect. In-operando study provides direct evidence about polysulfide shuttling, end product deposition, lithium insertion process, dendrite growth, and volume change whereas conventional electrochemical testing with coin cells conjectures possible outcomes in an indirect way.

Recently, a lot of techniques are modified to conduct in situ/operando characterization of LSB, such as X-ray photoelectron spectroscopy (XPS), X-ray

absorption spectroscopy (XAS), X-ray tomography (XRT), X-ray radiography (XRR), X-ray fluorescence (XRF), Fourier transform infrared spectroscopy (FTIR), ultraviolet–visible (UV–vis) absorption spectroscopy, Raman spectroscopy, transmission electron microscopy (TEM), atomic force microscopy (AFM), nuclear magnetic resonance (NMR), etc.[29-36]

Inside information provided by in situ/operando techniques greatly improved the understanding of complex polysulfide evolution process. Toney and Cui reported that crystalline Li_2S appear before the end of discharge process, which completely differed from previous theorem.[37] Furthermore, in situ XRD result shows a two-step process where Li_2S was formed at the end of first potential plateau around 2.15V.[38] The end product was a mixture of Li_2S and Li_2S_2. Dong and co-workers revealed that elemental sulfur can hardly recovered with in situ Raman.[39] S_8 conversion was impeded due to kinetically unstable Li_2S_8. Accordingly, the author immobilized the unstable species with Lewis base, which has strong affinity to polysulfides. Polysulfides were promoted to convert to S_8, which provide insight to improve the coulombic efficiency. Polysulfide are mixture of Li_2S_x ($1<x<8$), while the ratio of each component is unknown, especially during cycling. This is a critical information needed to design proper polysulfide attractive material. In-situ UV-vis demonstrated that Li_2S_2 and Li_2S_3 are dominant species during cycling.[40] Additionally, concentration of Li_2S_8 remain low during cycling, especially after first plateau. Accordingly, confinement of Li_2S_2 and Li_2S_3 in the cathode could achieve greater performance improvement.

Deeper understanding of the reaction mechanism and conversion pathways between end products needs contributions of various in situ/operando techniques. However, in situ/operando characterization of LSB requires combination of electrochemical and spectroscopic instruments. The enclosed battery system needs more novel customization of above instruments. Nevertheless, the rational design and improvement of LSB greatly rely on the in situ/operando investigation.[41]

1.3. Theoretical simulation of Li-S battery

The Main Objective of the proposed research is to develop a multi-scale computational methodology to optimize the morphology of the pores and surface of the cathode in Li-S batteries and conduct in-operando observation to validate the computational result. Recent studies demonstrated that 3-dimensional (3D) porous CNT electrodes are very promising. Therefore, the proposed research will be focused on electrodes made of CNT frameworks, and the results can be readily applied to other types of electrodes. The current simulation methods are focused on either atomistic calculation such as density functional theory (DFT) or macro-scale finite element method (FEM). Their length scales are either too small or too large to compute the characteristics of mass/ion diffusion through pores and overall charge transfer on the surface of electrodes in Li-S batteries.

The atomic-level information of LSB charge/discharge can be investigated by Molecular dynamics (MD) simulation, which is based on first-principles methode.[42] Ma et al. investigated lithiation and de-lithiation process of LSB by ab initio molecular

dynamics (AIMD) simulation. The dissolution of lithium polysulfides is revealed in the simulation, attribute to the strong interaction between polysulfide and electrolyte through lithium bond. AIMD is also employed to evaluate sulfur reduction kinetics and mechanism.[43] Dangling bonds on the edge of carbon sheet shows strong sulfur-carbon and lithium-carbon interaction, thus reactivity enhanced. Balbuena et al. reported that the edge of graphene sheets rearranges into multilayer structure as Li_2S growing around them.[44] The simulation demonstrated that polysulfide trapping capabilities could be improved by creating defects in graphene.

Density functional theory has been widely used in the calculations of binding energy between polysulfide and cathode material. Cui, et al. have reported the binding energy versus carbon material,[45] functional groups[46], polymer[47], and transition metal chalcogenide[48]. Graphene has promising application in energy storage device. The binding energy versus graphene and N-doped graphene[49] has been reported by Lu, et al. Beyond the graphene framework, research has been done to calculation the interaction between difference configurations of sulfur cluster Li_2S_x (x=1,2,4,8) and slab surface of metals and metal/graphene composite.[50] The dissolution of polysulfide into electrolyte is the main reason that active material detaches from electrode framework. Balbuena, et al.[51] took solvation effect into the calculation, which revealed the strong interaction between polysulfide and electrolyte, and related binding energy of MoS_2 and MnO_2.

2. FUNCTIONAL CARBON NANOTUBE SPONGE FOR LSB ELECTRODES

Developing high-energy-density and low-cost batteries has been driven by the increasing market demand for use in transportation, portable device, as well as the electric grid. The high price and relatively low energy density of the currently widely used Li-ion batteries do not meet the demand. We have recently developed Li-S batteries whose energy density is at least two-fold higher with a much lower cost. The cathode of our battery is enabled by a sponge-like CNT bulk. With high electrical conductivity as a result of seamless electron transport across the junctions between CNTs in addition to self-standing nature and high porosity, our Li-S batteries have achieved superior performance compared to commercial Li-ion batteries with the same size. We made and tested pouch cells in comparison to tiny coin cells in typical research labs, so our technology is very close to actual commercial production. Our process of producing the key material, CNT sponge is low-cost and scalable. The main ingredient, sulfur in our battery is at least 300 times cheaper than the counterpart (cobalt) in Li-ion batteries, so this technology has great potential in deploying various systems consuming or storing electrical energy such as electric vehicles, drones, airplanes, and solar cells.

We have developed a facile and scalable way of producing Li-S batteries using carbon nanotube sponges developed in the group as a key cathode scaffold material, which enables high areal loadings of sulfur and stable cycling performances. The simple synthesis process can be readily adapted to the typical production line of carbon nanotubes. The high energy density as well as low manufacturing cost of our Li-S

batteries compared to current Li-ion batteries make us believe substantial opportunities for commercialization.

2.1. Large scale synthesis of carbon nanotube sponges

Carbon nanotube (CNT) has been investigated for decades since it was discovered. It opened a new era and drew a lot of attention due to its outstanding mechanical and electrical properties. More importantly, the properties of this nanomaterial can be tuned by modifying its structure, such as length, diameter, number of layers, functionalized surface, etc. CNT can be synthesized by arc discharge, laser ablation, chemical vapor deposition (CVD), and many other methods. CVD is popular because of the high yield and quality. However, applications of CNT were limited by its powdery form and manufacturing scale. As of now, commercially available CNTs are all in a powdery form. Such powdery CNT requires additional processes to make tangible bulk materials such as a free-standing structure for practical applications. Our lab has developed a facile, one-step CVD process to fabricated cylinder type free-standing CNT sponge. Nevertheless, this process is not continuous, meaning that the process needs to be stopped to get the sponge out of the reaction chamber. During the reporting time period, efforts have been made to develop a process and setup to continuously synthesize CNT in a form of porous films so that the films can be directly used as electrodes for battery applications.

2.1.1. Design and Fabrication of Continuous Synthesis Setup

To develop a continuous roll-to-roll process, we have designed the key components, including rectangular furnace tubing, heaters with controllers, housing,

roller systems with controllers, heating elements, catalyst and gas delivery system. The structure of the setup was accomplished by computer-aided design in parts and assemblies. The furnace setup is divided into three major components, inlet housing, reaction tunnel, outlet housing. The inlet and outlet housing were designed and fabricated using stainless steel sheets. A four feet reaction tubing with two sealing flanges on each end was manufactured, which provided enough length for pre-heating zone and reaction zone. Heat transfer analysis was carried out to estimate heating power required. We designed a removable plate with proper connection and gasket to hold gas inlet tube and catalyst injection tube for assembly and maintenance. Safety and function tests were carried out after assembling the setup. All the parts are designed and fabricated. The system has been assembled and tested for air tightness and water leakage. Air tightness test is conducted by passing compressed air through the inlet/outlet and checking all the connection with soapy water. Proper gaskets and sealants were installed at all the connections. The rollers system was tested with a flexible wire, which shows that there is no interference with the housing.

The design of a roll-to-roll CNT synthesis system is schematically demonstrated in Figure 1. Each part of the system is fabricated with stainless steel sheets and tubes, as shown in Figure 2. The whole system was assembled and tested for air tightness and roller functions. There was no gas leakage when testing all the connections with soapy water. The roller system worked as designed with a soft substrate testing.

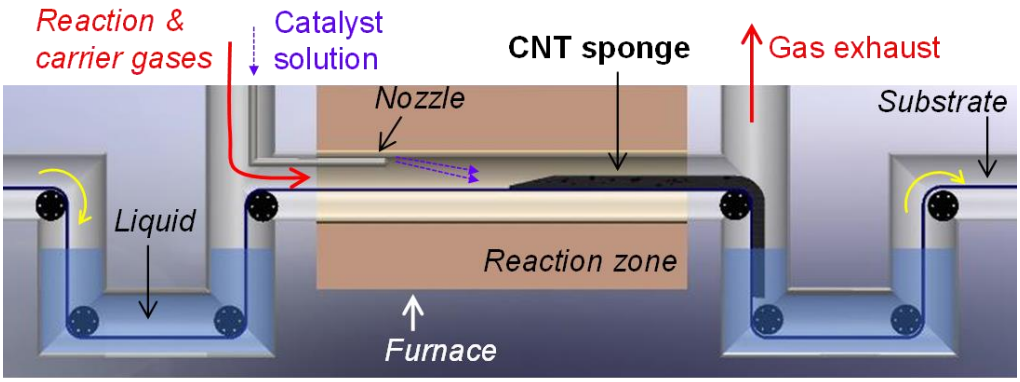

Figure 1. Schematic illustration of roll-to-roll CNT synthesis setup.

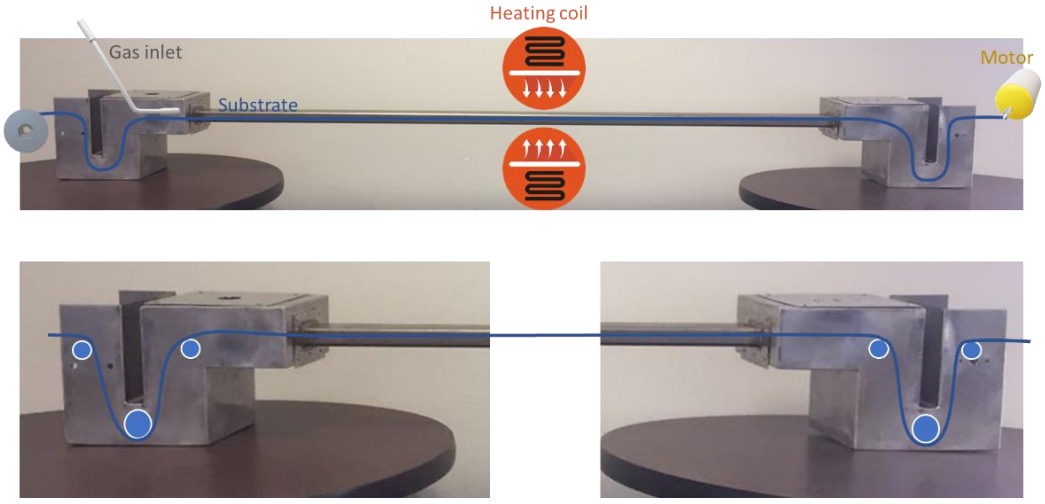

Figure 2. Photograph of the roll-to-roll system assembly.

The roll-to-roll CVD process involves gas inlet and outlet, catalyst injection, continuously moving substrate and heating system. We designed a series of rollers to guide the substrate, which is driven by a programmable motor at the end of the system. The feeding speed of substrate can be controlled by a controller. This is a small demo system and a large-scale production system for commercial applications can be realized using the same design. For the CVD process, a combination gas of hydrogen, ethylene, argon or nitrogen are passed through the system, among which the hydrogen and

ethylene are flammable. Water reservoirs are also used in the setup. We put extra time to make sure proper gaskets are installed on the screw holes, roller mounting holes and housing connections. The required liquid height (h) was calculated from the chamber pressure (p) using $h>p/\rho g$, where ρ and g are mass density of the liquid and gravitational acceleration, respectively. The catalyst injection tubing, gas inlet and outlet are mounted and connected by through-wall Yor-Lok fittings to prevent leakage. The system was run with inert gas and heating system to test sealing and gasket performance before operating the CVD process. Pre and post-treatment segments can be integrated before and after the CVD setup, in such way the system can manufacture ready-to-use products from a pristine substrate.

2.1.2. Substrates for continuous CNT Synthesis

In order to continuously grow free-standing CNT films in the roll-to-roll setup, we need proper substrates compatible with the delivery system, CVD process, and favorable for CNT growth. The substrate carries the continuously grown CNT through the roll-to-roll system. It is very important to select a proper substrate and necessary treatment for following reasons. First, it needs to be flexible and strong as a carrier in the roll-to-roll system. As it goes through all the roller system, the substrate needs to be flexible to maintain the path guided by the rollers and strong enough to hold the tension driven by the motor. Secondly, to efficiently grow CNT on the substrate, the surface should be favorable for CNT growth as a seeding layer. Iron, nickel, cobalt and many other metals have been reported as a catalyst for CNT growth in the CVD process. A thin metal layer can form small islands within nanometer scale during the heating

process. As more and more carbon dissolved in such metal islands, the CNT starts to grow from the saturated carbon-metal mixture. Electroplating a controllable method to deposit such thin seeding layer, which is also a viable solution in the industry and can be integrated into our system. Since the ferrocene is the catalyst for the CVD process, it is essential to select a metal that can attract iron particle at the reaction zone. Thirdly, the as-prepared free-standing product is expected to be directly used as a functional material, such as electrode, CNT-polymer composite, etc. The final product needs to be either compatible with such applications or easily peeled off from the substrate. For the application as electrodes of batteries, copper and aluminum are ideal candidates. We have tested CNT growth on different substrates with modified CVD chamber to mimic the environment of the roll-to-roll setup. Since the reaction tubing of the roll-to-roll system is made of stainless steel, we inserted a stainless-steel shim along the inner wall of quartz tube for all the experiments conducted with quartz tube. Stainless steel and other metal mesh can be good candidates due to their surface area, good flexibility and strength. We have tested brass, nickel, copper, stainless steel as potential candidates. The substrates were cleaned and placed in the prepared quartz tube, following by a typical CVD process for 30min. The substrates also need to be favorable for fast and efficient CNT growth. Pre-treatment of the substrates with proper seeding catalytic layers was necessary for this purpose. Different catalysts loading methods were investigated, including spray coating ferrocene, electroplating iron and nickel. Spray-coating of ferrocene powders on the substrate was expected to function as a seeding layer for CNT growth. Electroplating seeding layers provided a controllable methodology. Nickel

electroplating showed good results in terms of the CNT growth rate and quality. We further investigated the outcome with different electroplating thicknesses, current and time. We are currently investigating suitability of Al substrates and conditions for faster CNT growth.

CNT growth on different substrates have been tested. The image of the sample, Figure 3(a), shows a thin black film on the stainless-steel substrate. As shown in Figure 3(b-c), the SEM images displays a typical 3D CNT structure with a tube diameter around 50nm.

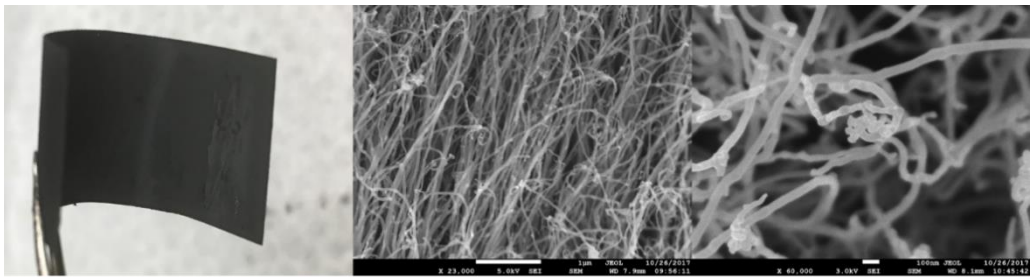

Figure 3. CNT growth on stainless steel substrate inside a quart tube. (a) Digital image of the CNT grew on stainless steel substrate. (b) SEM image with a scale bar of 1μm. (c) SEM image with a scale bar of 100nm.

CNT was successfully grown on a stainless-steel substrate, while the production rate is low. To promote the growth rate, we decide to coat a thin catalyst film on the substrate. Among several different electroplating conditions, the sample in Figure 4 shows the best CNT quality in terms of purity and tube geometry. An approximately 600nm nickel was electroplated on the stainless-steel plate (Figure 4a), with a current density of 8mA/cm2 for 4 minutes. As shown in Figure 4b,c, the CNT growth rate is

improved comparing with the result of Figure 3. The quality will be further improved to reduce amorphous carbon and impurities.

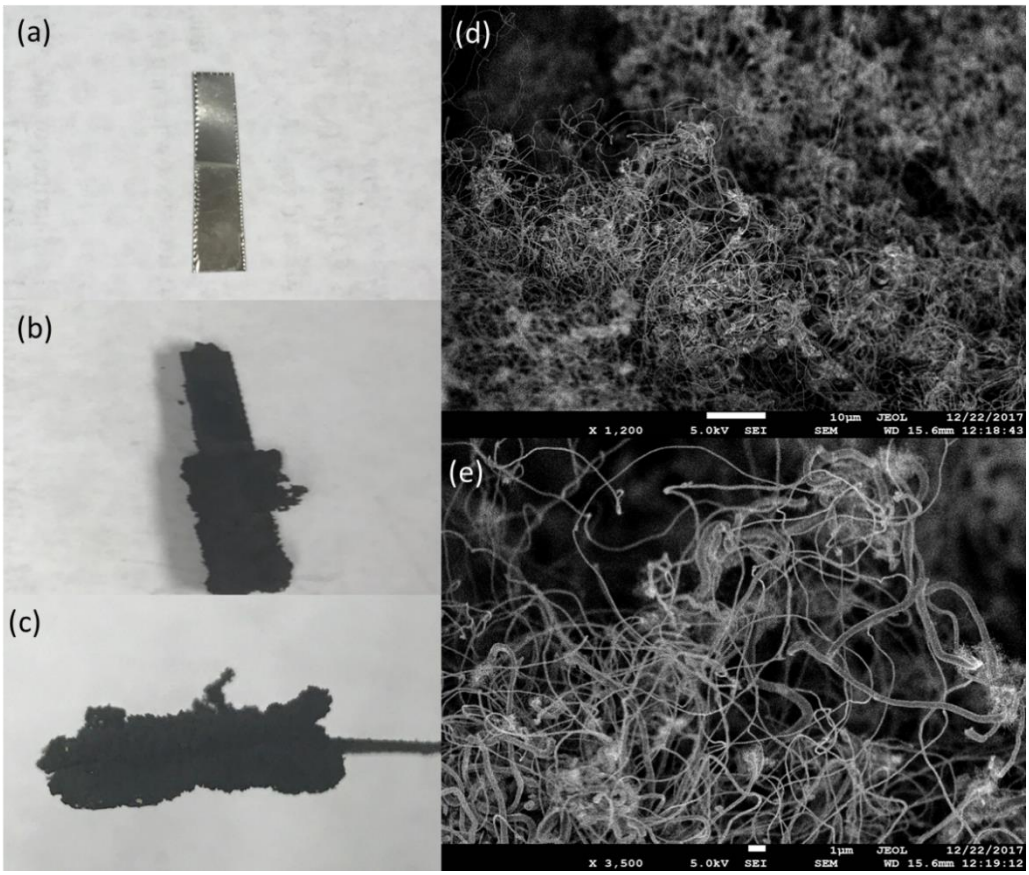

Figure 4. CNT grown on nickel electroplated stainless steel. (a) Lower part of the substrate is electroplated with nickel. (b-c) after 30min of CVD growth. (d-e) SEM images of CNT growth on nickel electroplated stainless steel.

The same electroplating treatment was also carried out on copper substrate. As shown in the Figure 5 below, the growth rate was significantly improved while the CNT quality was not as good as the one on stainless steel.

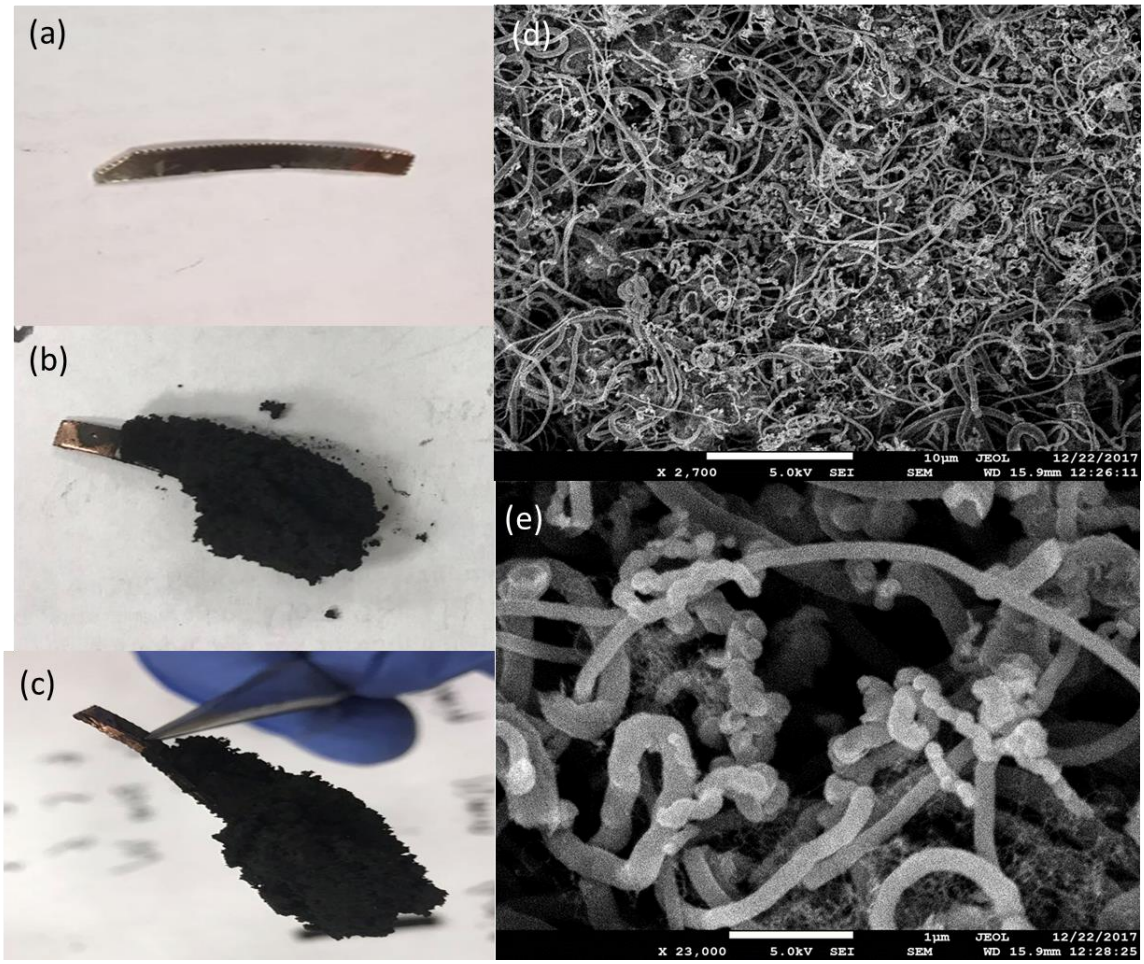

Figure 5. CNT grown on nickel electroplated copper. (a) Lower part of the substrate is electroplated with nickel. (b-c) after 30min of CVD growth. (d-e) SEM images of CNT grown on nickel electroplated copper.

In summary, different candidate substrates have been tested, including nickel, aluminum, copper, brass, stainless steel foil and mesh. Stainless-steel can be a good candidate in current stage considering the production rate, CNT quality and mechanical properties as a roll-to-roll carrier. Electroplating a seeding layer significantly improved the production rate. We electroplated different thickness of iron and nickel on stainless steel foils and meshes. After a set of comparative experiments, the stainless-steel mesh

sample, with about 600nm nickel electroplated by a current density of 8mA/cm2 and 4 minutes electroplating time, showed the best results. Aluminum and copper substrates were also tested with low temperature CVD process.

2.1.3. Improved catalyst delivery method

Catalyst plays an important role for CNT growth, which controls the diameter of tubes, number of walls, length of tubes, porosity and tortuosity of the 3D structure, which are crucial characteristics for various applications. The catalyst was delivered by injecting ferrocene solutions. We tested various solvents such as hexane, benzene, xylene, ethanol and so on to dissolve ferrocene for continuous catalyst delivery. It needs to consider solubility, boiling point, decomposed product in the reaction zone. The solvent can be decomposed to hydrocarbon at the heating zone, which can be a carbon source for CNT growth. The concentration and volume of the catalyst solution can determine the catalyst particle size in the reaction chamber. The properties of CNT film can be tuned by controlling the particle size of the catalyst. It is important to select proper carbon source to catalyst ratio for efficient fabrication without compromising of the product quality. Ferrocene catalysts need to be continuously delivered to the reaction zone where CNTs are growing. Solid state powdery ferrocene cannot be easily delivered to the reaction zone due to the high temperature and air-tight design to prevent gas leakage. Therefore, ferrocene was dissolved in a solvent and sprayed into the reaction zone by a nozzle, which provide a controllable manner to deliver catalyst. Hexane has demonstrated good ferrocene solubility and compatibility to the CNT synthesis. The ferrocene functioned not only as a catalyst, but also performed as a carbon source upon

decomposition. When the concentration of ferrocene in the catalyst solution was low, randomly and rapidly grown CNTs were obtained with relative rough surfaces. CNT films were more compact and smoother when ferrocene in the solution was concentrated. In addition, the catalyst solution was injected into the CVD chamber by a syringe-pump system as well. With a concentration of 10 mg/mL, the solution was injected into the pre-heating zone when the furnace was turn on. For a 30min growth, 15mL solution was injected to provide sufficient catalyst.

To further improve the CNT quality and deliver catalyst with a controllable manner, a liquid delivery system was tested. Ferrocene was dissolved in hexane and injected by a syringe-pump system. The SEM, Figure 6a-c showed that the CNT quality was better than the one with floating catalyst method in Figure 4. The CNT grown on a nickel electroplated stainless steel mesh has evenly distributed tube diameters, even though an agglomerated catalyst particle was detected. The further research will be conducted with stainless steel and liquid delivery system.

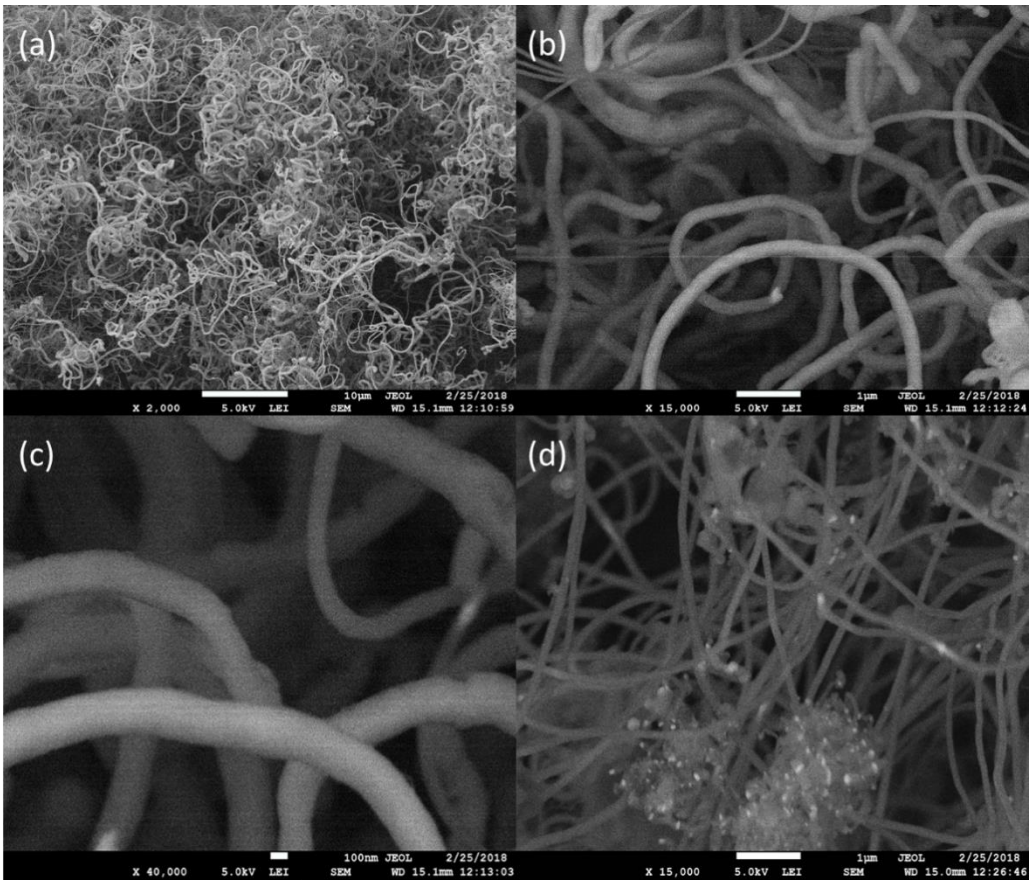

Figure 6. (a-c) CNT grown on nickel electroplated stainless-steel substrate with liquid catalyst delivery system. (d) CNT grown on nickel electroplated stainless-steel mesh.

The catalyst solution is designed to deliver by a syringe-pump system. Hexane shows good performance among the solvent candidates in terms of ferrocene solubility, boiling point, cost of material and product quality. Among different combinations of concentration and volume, the result with a concentration of 10mg/mL and a volume of 15mL showed compact free-standing structure and smooth product surface. Further research will focus on tuning the CNT properties by controlling catalyst solution conditions.

2.1.4. Modified CVD condition for low-temperature synthesis

The CVD condition, including pre-heating and reaction temperature, gas constituent, substrates moving speed, catalyst delivery and gas flow spoiler are modified according to different substrates and further improved for efficient production. Pre-heating temperature controls the sublime rate of catalyst. Elevated reaction temperature can provide sufficient kinetic energy for the nucleation of CNT tube, while it might also cause the agglomeration of catalyst particles. Since ethylene is the main carbon source for the CNT growth, the flow rate and partial pressure significantly influence the properties of CNT. Substrate moving speed determines the thickness of the CNT film. It is important to improve the growth efficiency as a commercially viable solution. To find out how much reaction gases are not participating in the growth, we tested different flow constrictions and measured film thicknesses. Based on the results, we will design a proper flow constriction to make the gas flow more accessible to the substrate, which will not only increase the production rate but also reduce the production cost and time. CVD conditions, such as temperature, gas flow rate, catalyst amount, substrate orientation, can be modified for more efficient growth of CNT. For a 30 minutes growth, 15mL and 30mL catalyst solution with a concentration of 10mg/mL were injected with typical CVD conditions. The result showed similar amount of product, which proved that 15mL catalyst solution was sufficient for current conditions. It was found that the ratio of catalyst to carbon source was important in the growth rate and quality of CNT. Low temperature CVD process is under investigation for a substrate with a low melting point, such as aluminum. The lower reaction temperature of 600℃ and 620℃ were

tested on bare aluminum and electroplated aluminum substrates. We also a partially blocked the furnace tube in order to identify how much gases and catalysts were wasted, which provide an angle between the substrate and gas flow. With more carbon source and catalyst accessible, tilted mesh substrates demonstrated improvements on the CNT growth rate and morphology.

2.1.5. Summary

A CNT film was successfully grown on a nickel electroplated stainless steel mesh, as shown in Figure 7. The size of the CNT film is 2cm×4cm. Thickness is about 2mm. This sample is ready for further research purpose, such as battery electrodes, microbial fuel cell, carbon-polymer composite, etc. With the results above, we demonstrated the functions of the roll-to-roll CNT synthesis setup, feasibility of growing CNT film on flexible electroplated substrates, potential to further improve the quality and growth rate of the CNT. By finalizing the roll-to-roll setup, such as heating elements, driving motor and structural supports, we will be able to build a prototype that can demonstrate feasibility to commercialize in the industry.

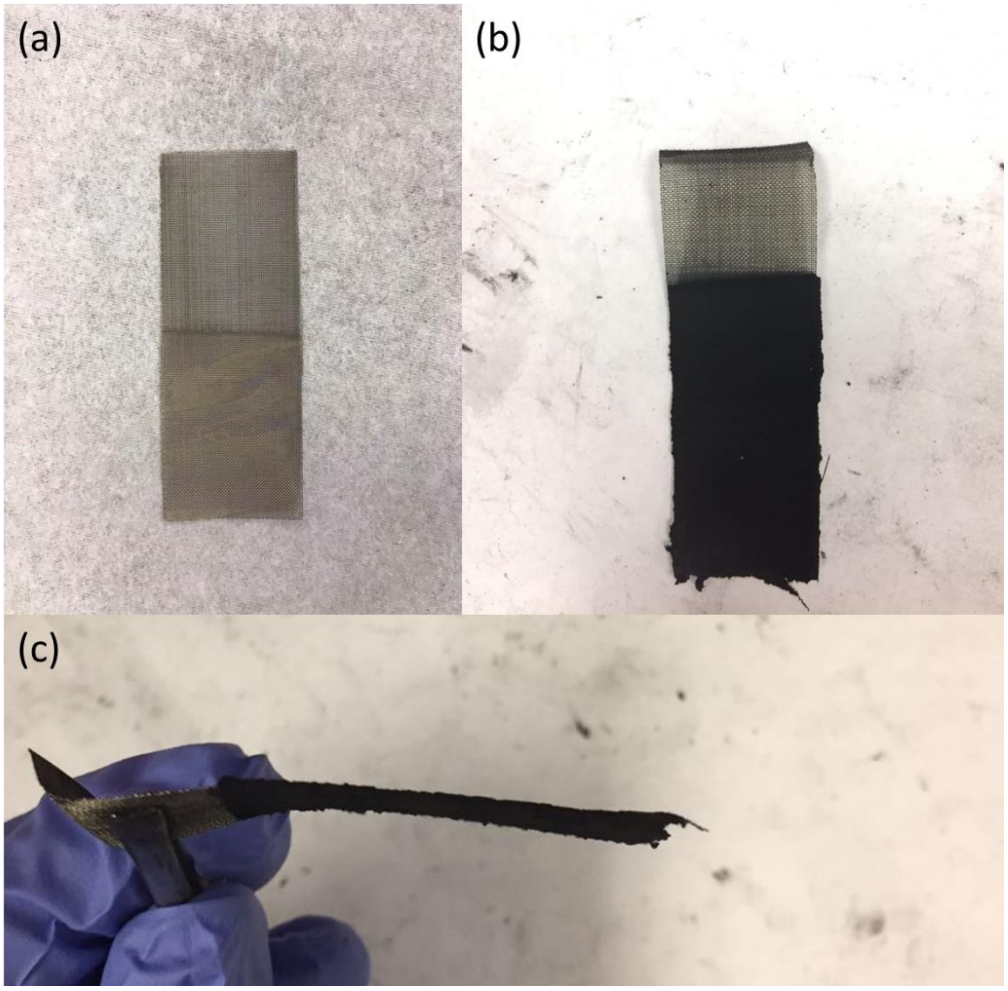

Figure 7. CNT grown on nickel electroplated stainless steel mesh. (a) Nickel electroplated stainless steel mesh. (b) Top view and (c) side view of the sample after CVD process.

The roller-to-roller synthesis setup is manufactured and assembled. Working functions have been tested. The roller system works as designed. CNT film was successfully synthesized on electroplated stainless-steel mesh. The CNT film is free-standing, which can be peeled off from the substrate. The current results indicate that our design is feasible to commercialize the technology. For the next step, we will finalize the synthesis setup, assembling heating elements and driving motor, test different substrate

for specific purposes, further improve CNT film quality and production rate. With those researches accomplished, a prototype of continuously growing CNT film system will be demonstrated for commercializing the technology.

Since the discovery of carbon nanotubes (CNTs), there have been extensive amount of studies for CNT over several decades. Although CNT has been turned out to have various exceptional properties compared to conventional materials such as high strength, high electrical conductivity, and high thermal conductivity, it has been difficult to utilize them practically for many reasons. One of the reasons is the difficulty in making tangible bulk structures out of the nanoscale CNT materials. Successfully implementation of our roll-to-roll design will bring CNT to a practical material. Our CNT sponge is 3D bulk with a free-standing structure so this can be utilized for various other applications that have not been accomplished by powdery CNTs. Carbon nanotubes have many application fields in material science, including structure material, battery, fuel cell, supercapacitor, thermoelectric, and so on. However, they were not practical due to the price and product forms. The limitation will be overcome by our mass production of free-standing 3D CNT bulks, which will significantly impact other disciplines.

3. THEORETICAL SIMULATION OF LI-S BATTERIES

The Main Tasks of the proposed study are to investigate the lithium-sulfur electrochemical reactions in a multicomponent electrolyte system, concentrations distribution of reactants and products in the porous medium, morphology evolution during charge and discharge, and influence of above factors on the capacity of the cell. Finally, the simulation results will be compared with the in-operando cells, which unveiled the evolution of polysulfide species.

3.1. Introduction

Among many Li-S battery electrode materials, CNT is one of the most popular materials since it has outstanding electrical properties, high surface area, and capability to accommodate large volume expansion. The meso-scale structures of the CNT framework such as pore size, tortuosity, and surface area and the micro-scale features such as functional groups on the surface of electrodes directly influence the macro-scale battery performances including capacity, cycle life, C-rate performances particularly during fast charging/discharging and a large number of cycling processes. However, the relations between the multi-scale behaviors have been barely studied so far.

Many researchers have conducted theoretical atomistic scale calculations such as binding energy calculations between polysulfides and functional groups on electrode surfaces so as to identify better choices for attracting polysulfides with a hope of minimizing the polysulfide shuttle. For example, the atomistic calculation provide insight about better functional groups, but it is unclear how much improvement in the actual battery performance the functional group can provide. On the other hand, cell-

level macro-scale calculations do not entail the important information about the electrodes such as the pore morphology in the electrodes and functional groups on the electrode surface.

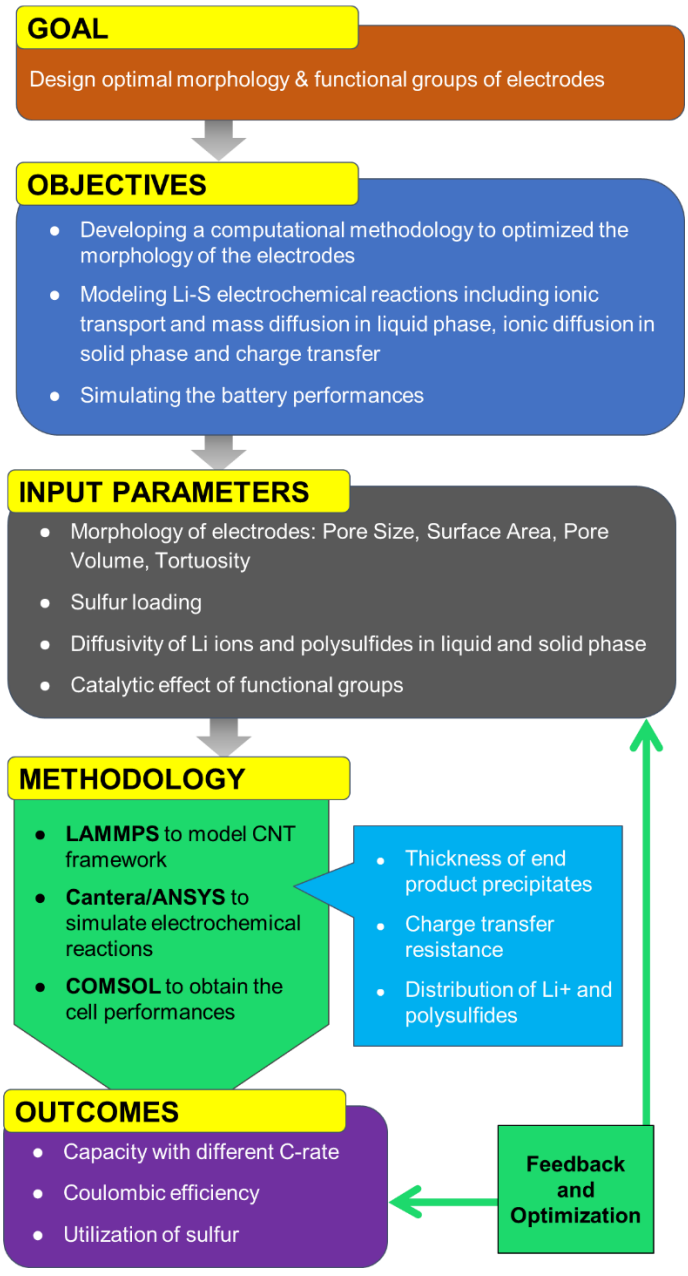

Figure 8. Overview of the proposed computation and experiment strategy.

Currently the connections between the two dissimilar scale modeling methods are missing, to the best of our knowledge, but it is essential to properly design optimum battery electrodes. Here the proposed research is to study how to link the multi-scale modeling methods. Successful studies will make it possible to convey the detail information from atomistic calculation to micro/meso-scale simulations that contain larger scale information, which will then be integrated into macro-scale calculations for the actual cell-level battery performances. The results from the multi-scale simulation have significant impacts on battery research in practice because they will enable rational approaches for designing optimal morphology of the electrodes for the high cell-level performances of Li-S batteries. The computation and experiment flow chart can be seen in Figure 8.

3.2. Computational Methodology

3.2.1. Micro-Scale Modeling of Electrode Materials

CNT, CMK-3, carbon black, and other carbon-based nanomaterials are widely used in Li-S research community, benefiting from its outstanding electrical properties, porous structure, excellent framework for nanoparticles and functional groups. The binding energy of polysulfide and functional sites has been widely studied. Here we will utilize these atomistic simulation results to study a more “realistic” case beyond the atomistic level simulation, but details such as functional groups embedded in a conducting framework, which influence the kinetics of Li-S electrochemical reactions, will be taken into consideration.

We will firstly start from a simpler system, a bundle of straight framework, to mimic the simplistic electrochemical reaction inside the nanomaterials (Figure 9a). Then, the CNT network will be modeled by LAMMPS (Figure 9b) with proper force fields and potentials, in such a way that the physical properties, pore size, tortuosity, surface area, and CNT diameters in the electrode can be defined.

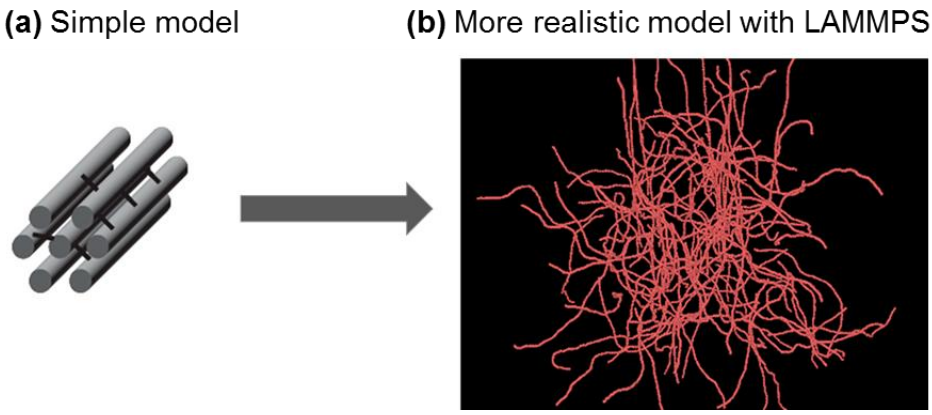

Figure 9. The modeling of electrode framework.

In addition, the functional groups and nanoparticles attached to the framework are now being actively studied with tangible outcomes such as the adsorption of polysulfides and catalytic effects for promoting the electrochemical reactions. Here we will model not only the morphology, but also include the functional groups and nanoparticles in the model. The micro-scale structure modeled in this step will provide a base framework, which will be one of the important variables in the subsequent research.

3.2.1.1. DFT simulation

Theoretical calculation of the binding energy between the anchoring materials and polysulfide species is a crucial step toward rational design and screening of the

candidate materials for Li-S battery research. MnO_2 is a one of the metal oxide candidates that have been reported in the experimental studies. Through first-principles calculations, this project reported the binding energy between α-MnO_2 and Li_2S_6. It is worth noting that the lithium polysulfide was positioned vertically in this system, which is based on the assumption of strong interaction between Li and O. This report provided a comparison of binding energy with different orientation of lithium polysulfide with current literatures. By first-principle calculations, the anchoring effect was theoretically described and quantitively compared within the system. The results provided the fundamental rationales to design the cathode materials.

The challenge of lithium-sulfur application is the shuttle effect, which would cause significant capacity degradation during the cycling.[52] The intermediate reagents species Li_2S_x ($4 \leq x \leq 8$) is soluble in the electrolyte. Due to the dissolution effect and concentration difference, the polysulfide species would diffuse to the anode if the adsorption to the polysulfide was not introduced in the cathode. The diffusion of polysulfide causes loss of active cathode material, which leads to drastic capacity degradation. To overcome this challenge, researchers have developed various approaches, such as functionalized cathode material, embedding adsorbing nanoparticles, polysulfide repelling separator and so on. Among these approaches, the polysulfide absorbing materials have been widely explored. However, experimental exploring the candidate materials would be less-effective. First-principle calculations provided a way to fundamentally understand the binding effect and to evaluate the

expected performance of such material, which can help to efficiently screen the candidates and improve the outcome by optimizing the binding energy.

3.2.1.2. Literature Survey

The mechanism of interaction between nanoparticles and polysulfide need to be explored. The coordination of polysulfide ions and functional sites remained unclear. In particular, the orientation of polysulfide and phase of nanoparticles need to be further studied. Extensive researches have been conducted on carbon-based materials, due to the porous structure and outstanding conductivity. However, the nonpolar carbon-based materials interact weakly with polar Li_2S_x species, which would cause the severely shuttle effect and poor kinetics. Polar materials have been introduced to the carbon-based cathode, such as oxygen functional groups, nitrogen groups, polymer, metal oxide, and transition metal chalcogenide. The selection of such candidates was intensively empirical work due to the lack of fundamental understanding about the interaction between polysulfide and potential materials. Simulations have been carried out on the adsorption effect of anchoring materials. However, it is still unclear how the conditions of anchoring materials and orientation of Li_2S_x affect the binding energy. This report is based on MnO_2 and Li_2S_6, which is a high-order soluble species in the Li-S battery. MnO_2 have been extensively studied by experimental approach and some simulation work. The phases of MnO_2 also significantly affect the properties. This work started the concept or studying the influencing factors of binding energy, in particularly the orientation of Li_2S_6 and phase of MnO_2.

3.2.1.3. Result

Systemically studies of lithium-sulfur clusters have been reported[49, 53], shown in Figure 10. Among the polysulfide clusters, Li_2S_6 is the most important species because it is the high-order polysulfide that starts to dissolve in the electrolyte during the discharge. Thus, the Li_2S_6 is selected to be the calculation object.

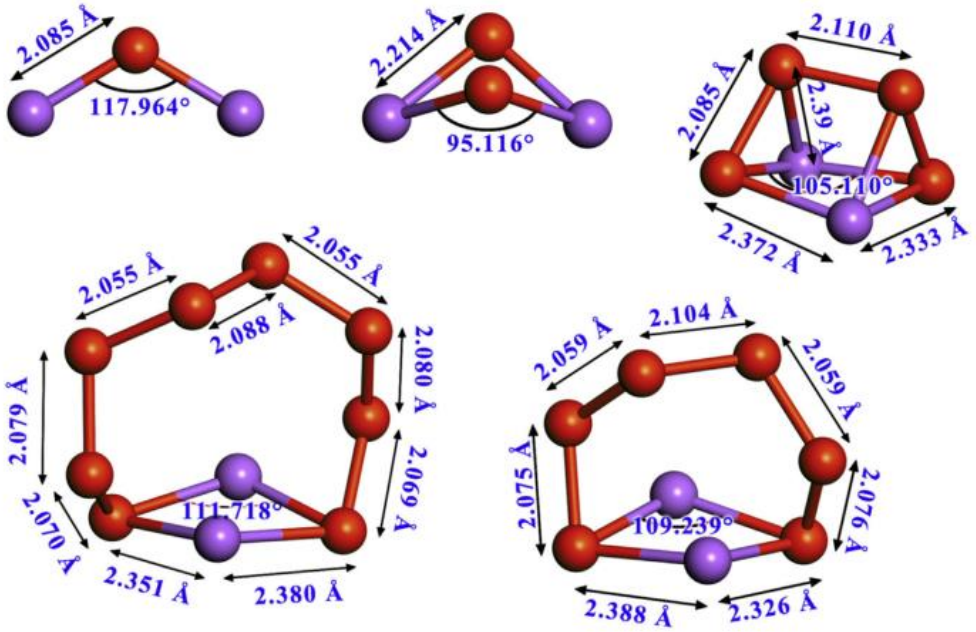

Figure 10 The geometric structures of Li2Sn (n = 1, 2, 4, 6, 8). Red balls represent S atoms, and purple balls are Li atoms.

Li_2S_6 was modeled with lithium ion facing downward, as shown in Figure 11, considering the strong interaction of lithium and oxygen. The Li_2S_6 structure was firstly relaxed in vacuum condition. The density functional theory (DFT) computation were performed via Vienna ab initio simulation (VASP) package.[54] The projected augmented wave (PAW)[55, 56] pseudopotential was used to describe the ion-electron interactions. The

generalized gradient approximation (GGA) was described by Perdew-Burke-Ernzerhof (PBE) exchange correlation function. The numerical convergence was accomplished with thresholds of 10^{-5} eV in energy under the cutoff energy of 400eV. The k-mesh grids were 2 × 2 × 2. The structure of Li_2S_6 was relaxed in a 20 × 20 × 20 Å box. The bond length between lithium and sulfur, sulfur and sulfur are 2.328 Å and 2.057 Å in the vacuum condition, respectively. Furthermore, van der Waal interaction was also considered with (vdW-DF2) functions.

MnO_2 was reported, by Nazar's group,[57] with outstanding polysulfide binding energy, which facilitate a high current cycling performance. α- MnO_2 was constructed in VESTA with a tetragonal structure, of which the lattice constants are a=b=9.865 Å, c=2.897 Å. The slab was built with 2 × 2 × 1 of the unit cell in a 20 × 20 × 20 Å supercell to avoid the interaction of periodic ions. The structure was relaxed in the same condition as the polysulfide cluster. The bond length between Mn and O is 1.743 Å.

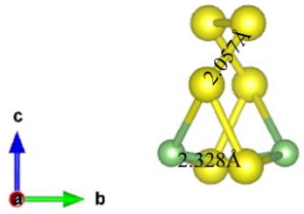

Figure 11 Structure of Li2S6

Li_2S_6 was modeled with lithium ion facing downward, as shown in Figure 11, considering the strong interaction of lithium and oxygen. The Li_2S_6 structure was firstly relaxed in vacuum condition. The density functional theory (DFT) computation were performed via Vienna ab initio simulation (VASP) package.[54] The projected augmented wave (PAW)[55, 56] pseudopotential was used to describe the ion-electron interactions. The generalized gradient approximation (GGA) was described by Perdew-Burke-Ernzerhof (PBE) exchange correlation function. The numerical convergence was accomplished with thresholds of 10^{-5} eV in energy under the cutoff energy of 400eV. The k-mesh grids were 2 × 2 × 2. The structure of Li_2S_6 was relaxed in a 20 × 20 × 20 Å box. The bond length between lithium and sulfur, sulfur and sulfur are 2.328 Å and 2.057 Å in the vacuum condition, respectively. Furthermore, van der Waal interaction was also considered with (vdW-DF2) functions.

MnO_2 was reported, by Nazar's group,[57] with outstanding polysulfide binding energy, which facilitate a high current cycling performance. α- MnO_2 was constructed in VESTA with a tetragonal structure, of which the lattice constants are a=b=9.865 Å, c=2.897 Å. The slab was built with 2 × 2 × 1 of the unit cell in a 20 × 20 × 20 Å supercell to avoid the interaction of periodic ions. The structure was relaxed in the same condition as the polysulfide cluster. The bond length between Mn and O is 1.743 Å.

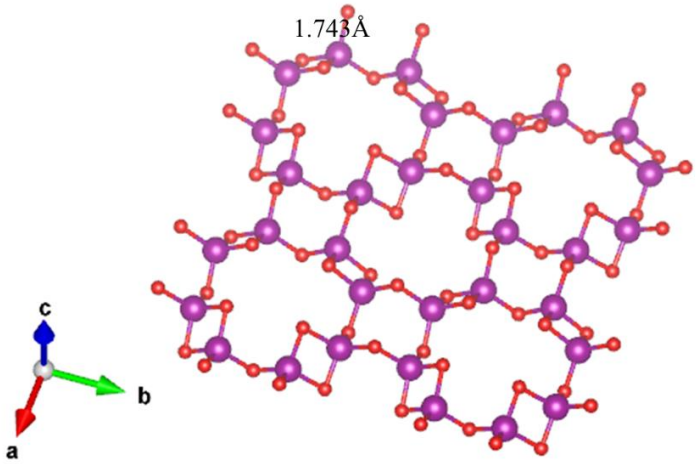

Figure 12 Structure of MnO2

After relaxation of each structure, the polysulfide cluster and MnO_2 crystal are combined into a supercell to relax at the same condition.

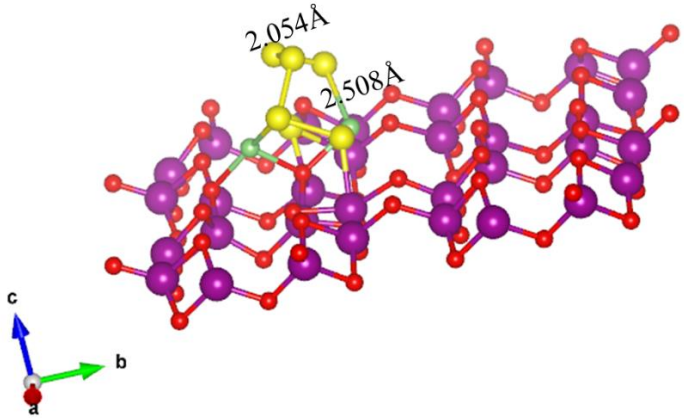

Figure 13 Final position of Li2S6 and MnO2

After the relaxation, the coordination structure of polysulfide and MnO_2 can be seen in Figure 15. The S-S bonding slightly reduce from 2.057 Å to 2.054 Å. However, the Li-S

bonding significantly increased from 2.328 Å to 2.508 Å. The elongation of Li-S bonding can be attributed to the strong binding force of Li-O. The coordination of Li-Mn can also be seen from the structure, which further proved that MnO_2 has a strong binding energy to polysulfide.

The binding energy (E_b) of polysulfide on MnO_2 slab can be calculated by the equation: $E_b = E_{PSMnO} - E_{PS} - E_{MnO}$, where E_{PSMnO}, E_{PS}, $and\ E_{MnO}$ are the total energy of polysulfide and MnO_2 coordinated system, polysulfide and MnO_2, respectively. For the system described above, the binding energy is:

$$E_b = E_{PSMnO} - E_{PS} - E_{MnO}$$

$$= -758.496\ eV - (-737.232\ eV) - (-31.511\ eV) = 10.247\ eV$$

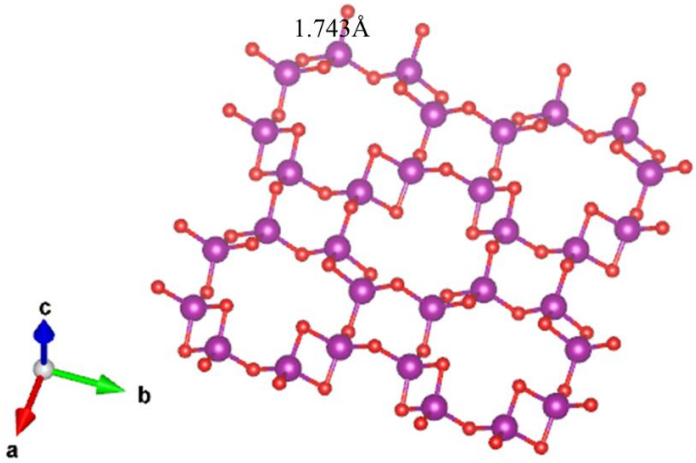

Figure 14 Structure of MnO2

After relaxation of each structure, the polysulfide cluster and MnO_2 crystal are combined into a supercell to relax at the same condition.

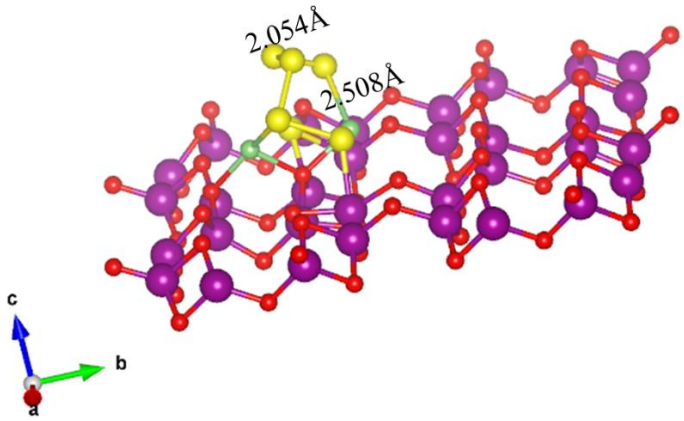

Figure 15 Final position of Li2S6 and MnO2

After the relaxation, the coordination structure of polysulfide and MnO_2 can be seen in Figure 15. The S-S bonding slightly reduce from 2.057 Å to 2.054 Å. However, the Li-S bonding significantly increased from 2.328 Å to 2.508 Å. The elongation of Li-S bonding can be attributed to the strong binding force of Li-O. The coordination of Li-Mn can also be seen from the structure, which further proved that MnO_2 has a strong binding energy to polysulfide.

The binding energy (E_b) of polysulfide on MnO_2 slab can be calculated by the equation: $E_b = E_{PSMnO} - E_{PS} - E_{MnO}$, where $E_{PSMnO}, E_{PS}, and\ E_{MnO}$ are the total energy of polysulfide and MnO_2 coordinated system, polysulfide and MnO_2, respectively. For the system described above, the binding energy is:

$$E_b = E_{PSMnO} - E_{PS} - E_{MnO}$$

$$= -758.496\ eV - (-737.232\ eV) - (-31.511\ eV) = 10.247\ eV$$

3.2.1.4. Discussion

The result reported the theoretical binding energy between a vertically aligned lithium polysulfide and MnO_2 slab, based on the assumption that strong interaction between lithium and oxygen. The outcome shows that the Li-S bond length was elongated due to the interaction of Li-O, which explained the strong binding energy of polysulfide and MnO_2. Surprisingly, the S atom at the end of polysulfide also has a tendency of binding to the manganese. Additionally, the study of different orientations of lithium polysulfide and phases of MnO_2 need further investigation. The DFT calculation need to be further improved to simulate empirical condition, such as solvation effect of electrolyte, more accurate iteration, and so on. The electronic structure calculation needs to be carried out for a better understanding of interaction, charge transfer, and adsorption configuration.

3.2.2. Meso-Scale Study to Simulate the Electrochemical Reaction

After the framework is modeled, the properties of necessary parameters will be defined to carry out meso-scale simulations. The electrochemical reaction can be limited by (1) ion and mass diffusion in liquid phase, (2) ion diffusion in solid phase, (3) electrolyte accessibility, and (4) charge transfer. By studying the diffusion limitation, precipitation/dissolution of insulating end products, volume of electrolyte, concentration of polysulfides, and other reaction conditions, we will be able to predict the electrochemical reaction kinetics with a given electrode design. This study will make it feasible to properly design and optimize the morphology of electrodes for improving the utilization of end products, the kinetics with suppressed shuttle effects.

The initial simulation will be conducted on a single CNT network defined in a simplified 3D model. The nucleation of S8 or Li2S can be demonstrated through Cantera, which is an open-source software for problems involving chemical kinetics, thermodynamics and transport process. The S8 or Li2S nucleation begins when thermodynamics favor the solid phase in particle form over the ionic phase, which associated with the concentration of the species in the electrolyte. The nuclei size depends on the critical cluster size, which is related to the formation rate of such species. For example, with low current density, a large sulfur particle would be expected on the CNT surface, while a smaller particle will be formed with high current density because of more nucleation energy. Besides current density, we will carry out the simulation based on several variables, such as functional groups, surface area, tortuosity, and so on. This meso-scale simulation step will reveal the critical connection between micro-scale

morphology and macro-level battery performance. With such detail information behind the mechanism, we will be able to analyze and address the issue on the battery performance and to optimize it by adjusting the morphology and improving the kinetics.

3.2.3. Macro-Scale Simulation of Battery Performances

In this step, the battery performance will be simulated in COMSOL with meso-scale results. For example, the electrical resistance will depend on the thickness of end products depositions, which will be fed from the meso-scale simulation, as a function of depth of charge/discharge. The local concentration around the electrode will be achieved by monitoring the electrochemical reaction rate. The electrolyte accessibility will also be modeled according to the morphology of end products' nucleation.

3.2.3.1. Thoery

Two of representative reactions of a lithium sulfur battery are listed below: Eq (1) and Eq (2).

$$\boldsymbol{S_8^0 + 4e^- \leftrightarrow 2S_4^{2-}} \qquad \textbf{Eq (1)}$$

$$\boldsymbol{S_4^{2-} + 4e^- \leftrightarrow 2S^{2-} \downarrow + S_2^{2-}} \qquad \textbf{Eq (2)}$$

For a multicomponent electrolyte system in a porous medium, the material balance on an individual species is given by:

$$\frac{\partial \varepsilon C_i}{\partial t} = -\nabla \cdot N_i + r_i - R_i$$

where ε is the pore volume of the electrode, C_i is the concentration of the species i, $-\nabla \cdot N_i$ represents the flux of species into the system, r_i indicates the productions or

consumption of the species by electrochemical reactions, and R_i is the precipitation rate of the species.

For the flux term N_i, diffusion and migration are both considered:

$$\frac{N_i}{\varepsilon} = -\, D_i\, \nabla\, C_i \;-\; z_i\, \frac{D_i}{RT}\, F C_i\, \nabla\, \varphi_2$$

where z_i is the charge number and φ_2 is the liquid phase potential.

The reaction rate of species i, r_i, is determined by the current density of related electrochemical reactions j :

$$r_i = -\, a \sum_j \frac{s_{i,j}\; i_j}{n_j F}$$

where $s_{i,j}$ is the stoichiometric coefficient for species i in reaction j, i_j is the current density, n_j is the number of electrons transferred, a is the surface area of the porous electrode, which described in this relation:

$$a = \; a_0 \left(\frac{\varepsilon}{\varepsilon_0}\right)^{\xi}$$

in which, a_0 is the initial surface area, ε_0 is the initial porosity, and ξ is the empirical parameter describing the morphology of the precipitate, which is set to 1.5 in this work. The current density of related electrochemical reaction j, i_j, is determined by Bulter-Volmer equation:

$$i_j = \; i_{0,\, jref} \left\{ \prod_i \left(\frac{C_i}{Ci,ref}\right)^{p_{i,j}} \exp\left(\frac{\alpha_{aj} F}{RT}\eta_j\right) - \prod_i \left(\frac{C_i}{Ci,ref}\right)^{q_{i,j}} \exp\left(\frac{\alpha_{cj} F}{RT}\eta_j\right) \right\}$$

where the overpotential for reaction j is given by:

$$\eta_j = \varphi_1 \; - \varphi_2 \; - \; U_{j,ref}$$

in which φ_1 is the potential in solid phase, φ_2 is the potential in liquid phase, and $U_{j,ref}$ is the open circuit potential for reaction j at the reference concentration $C_{j,ref}$.

$$U_{j,ref} = U_j^{\theta} - \frac{RT}{n_j F} \sum_i s_{i,j} ln\left[\frac{C_{j,ref}}{1000}\right]$$

Current density (i_j) depends upon the difference between the potential of the electrode (φ_1) and the potential in the solution adjacent to the electrode surface (φ_2) relative to the open-circuit potential for reaction ($U_{j,ref}$) evaluated at the surface concentrations of species ($C_{j,ref}$).

The liquid phase current density, i_e, is related to the flux of the species:

$$i_e = F \sum_i z_i N_i$$

Additionally, the charge can only be enter or leave the liquid phase by electrochemical reactions at the solid/liquid interface:

$$\nabla \cdot i_e = a \sum_j i_j$$

The solid phase charge-transfer is purely by electronic conduction, which is defined by Ohm's law:

$$i_s = -\sigma \nabla \varphi_1$$

Considering charge is conserved in the cathode, the charge leaving one phase must be qual to the one entering the other phase:

$$\nabla \cdot i_e + \nabla \cdot i_s = 0$$

Finally, the rate of production of consumption of species i due to precipitation and dissolution, R_i, is defined:

$$R_i = \sum_k \gamma_{i,k} \, R'_k$$

where R'_k is the rate of precipitation of the solid species k, $\gamma_{i,k}$ is the number of moles of ionic species i in the solid species k.

$$R'_k = \; k_k \varepsilon_k \left(\prod_i C_i^{\gamma_{i,k}} - K_{sp,k} \right)$$

where $K_{sp,k}$ is the solubility product of k in the electrolyte and k_k is the rate constant.

As the precipitate occupies the pore volume of the electrode, the porosity change can be defined as:

$$\frac{\partial \varepsilon}{\partial t} = - \sum_k \tilde{\mathrm{V}}_k \, R'_k$$

where $\tilde{\mathrm{V}}_k$ is the partial molar volume.

3.2.3.2. Boundary conditions

At the cathode/current collector interface ($x = L$), the flux of all the species are zero.

$$N_i = 0 \; at \; x = L$$

At the cathode/current collector interface ($x = L$), all the current density is carried by the solid phase, which is equal to the external current density applied to the system. This means that the solution phase current density at this boundary is zero.

$$- \sigma \, \nabla \, \varphi_1 = I_{app} \; at \; x = L$$

$$i_e = 0 \; at \; x = L$$

At the separator/cathode interface ($x = L_s$), the flux of each species is continuous

$$N_{i,separator} = N_{i,cathode}\ at\ x = L_s$$

At the separator/cathode interface ($x = L_s$), all the current is carried by solution phase alone, which is also continuous.

$$i_{e,separator} = i_{e,cathode}\ at\ x = L_s$$

$$-\sigma\,\nabla\,\varphi_1 = 0\ at\ x = L_s$$

At the anode/separator interface, we assume there is no polysulfide shuttle effect, which means that there is only Li^+ transported over the separator.

$$N_i = 0\ at\ x = 0$$

For Li^+, the flux boundary condition of the concentration of Li+ written as:

$$N_1 = \frac{i_1}{F}\ at\ x = 0$$

i_1 is given by Butler-Volmer equation for the anode reaction.

The potential of anode is set to 0.

$$\varphi_1 = 0\ at\ x = 0$$

Because the only species with nonzero flux at this boundary is Li^+, the liquid-phase current density at $x = 0$ is given by

$$i_e = FN_1\ at\ x = 0$$

3.2.3.3. Results

The 1D configuration was modeled in COMSOL (Figure 16a). Voltage profile (Figure 16b) shows typical two plateaus on the discharge profile. Charge time is less than discharge time, which indicates coulombic efficiency is less than 100%. This could be due to shuttling effect.

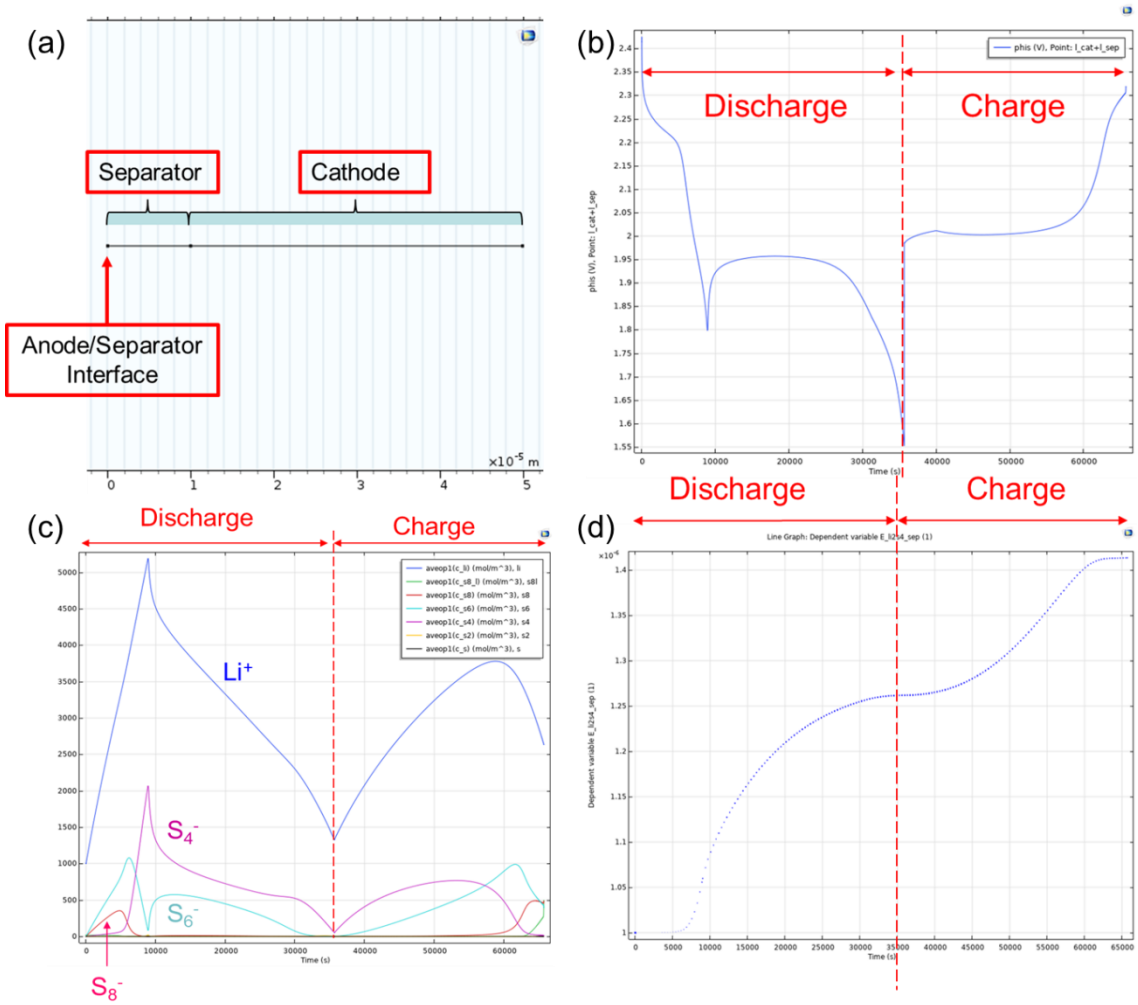

Figure 16. (a) 1D configuration of LSB in COMSOL (b) Voltage profile of discharge and charge (c) Average concentration of species (d) Concentration of Li_2S_8 in the separator

Concentration of Li^+ is significantly increased during first plateau and gradually reduced during the second plateau, as shown in Figure 16c. This is due to high-order PS dissolved in the electrolyte. At the end of discharge and charge, concentration of Li^+ and PS are higher than initial state, which indicates PS dissolved in the electrolyte and reactions are not completed. The large fluctuation of Li^+ concentration could cause polarization of the cell if ionic diffusion is not sufficient. Concentration of Li_2S_8 (Figure 16d) in the separator increases during the whole cycle. It demonstrates that PS diffused into separator cannot be recovered. The increased concentration gradient could cause PS shuttling effect to the anode.

Further performance results will be obtained such as capacity, utilization of active material, Columbic efficiency and C-rate performances.

4. MANGANESE OXIDE DECORATED CNT FOR LONG LIFETIME AND LARGE CAPACITY LITHIUM METAL ANODE*

4.1. Abstract

Graphitic carbon materials are commonly used for storing Li ions owing to outstanding electrochemical stability and electrical conductivity, and their 3D porous structures are promising in achieving high capacity anodes by depositing Li metal beyond lithiation. However, lithiophobicity and high conductivity of the graphitic surface engender dendrite formation on the outer surface of the electrode rather than insert Li metal into the pores. Here, we grafted mossy MnO_2 uniformly on the entire surface of carbon nanotubes (CNTs), concurrently providing lithiophilic and dendrite-less surfaces. Our MnO_2-decorated CNT can deliver the outstanding performance parameter, which considers both areal capacity and lifetime over 10,000 mAh^2/cm^2, which is the highest to our best knowledge, due to a super-long lifetime over 1800 hours for repeated Li plating/stripping at a high areal capacity of 6 mAh/cm^2. The striking improvement can be attributed to low overpotential due to superior lithiophilicity and electrolyte wetting characteristics of MnO_2, large surface areas from the mossy structures (low local current density), distributed Li insertion into MnO_2/CNT for suppressing dendrite formation, and porous CNT frameworks with high conductivity according to our electrochemical impedance spectroscopy and density functional theory calculation results. We anticipate our results give rise to subsequent research about

---

* Reprinted with permission from J. Tan, F. A. Soto, J. Noh, P. Wu, D. R. Yadav, K. Xie, P. B. Balbuena and C. Yu, *Journal of Materials Chemistry A*, 2021, **9**, 9291-9300.

mossy structure coatings on porous structures with various metal oxides and Li attracting groups for further improving the energy density of Li batteries.

4.2. Introduction

The current graphite-based anode used in Li-ion batteries cannot meet the growing demands for high energy storage. As the cathode materials in Li-ion batteries are approaching their theoretically highest energy densities, Li metal has drawn wide interest owing to its high specific capacity (3860 mAh g^{-1}) and lowest reduction potential (-3.04 V vs. standard hydrogen electrode). If Li metal can be substituted for the graphite anode, the specific energy density could be significantly increased by more than 70%.[58] Li metal anode is also essential to the next-generation batteries such as Li-S and Li-O batteries. However, it is still challenging to use Li metal as an anode due to uncontrolled dendrite formation, active mass loss due to extensive solid-electrolyte interphase (SEI) reactions, and large volume changes during Li plating/stripping.

Quite a few strategies for regulating Li plating/stripping behaviors have been suggested such as lowering overpotentials,[59-61] reducing local current densities,[62-64] and accommodating volume changes.[65-67] In particular, porous conducting media could significantly distribute the deposition sites of Li ions so as to significantly alleviate preferential Li depositions on local areas. However Li metal is prone to be deposited on the outer surface of the porous electrode because the diffusion of Li ions through small pores is unfavorable particularly when the surface of the electrode is conducting and lithiophobic, as demonstrated with straight pores with different diameters on copper electrodes[68] and randomly oriented carbon nanotube (CNT) scaffolds.[69] To mitigate this

problem, insulating and inert materials such as aluminum oxides have been coated on the outside of the electrode,[61] but it is required to separately prepare conducting inner surfaces to deposit Li metal in the inside of the pores. Perhaps, the best remedy for alleviating these problems is to develop a facile method to make porous electrodes whose inner surfaces are lithiophilic with low charge transfer resistance and large surface areas for attracting Li ions into the pores as well as outer surfaces are coated with low conductivity materials for preventing dendrite formation. Then the large surface areas in the porous structure can be utilized for accommodating large Li plating/stripping, which is especially important in fast charge/discharge with high current density.

Carbonaceous materials such as CNT,[70-72] graphite,[73, 74] graphene,[75-78] and carbon cloth[79, 80] have been widely adopted for fabricating anodes due to their high electrical conductivity and electrochemical stability. However, their poor affinity to Li ions necessitates introduction of lithiophilic functional sites on their surfaces or pre-lithiation for lowering the overpotential of lithium nucleation. Zhang *et al.* reported a low current density during lithium deposition on nanostructured graphene flakes,[62] and investigated the function of nitrogen groups on graphene as lithiophilic sites, showing a lower overpotential compared to those of pristine graphene and copper.[81] Mukherjee *et al.* demonstrated lithiophilic defects in porous graphene networks could work as seeding sites for distributing lithium growth.[65]

Lithiophilicity considerably alters the wetting behavior of molten Li. The wetting phenomena of molten Li on several metals and metal oxides have been studied by Cui

group, showing the wetting is strongly dependent on thermodynamically favorable negative Gibbs free energy.[82] Róg *et al.* investigated the Gibbs free energy of formation of lithium manganese oxides, as described below.[83]

$$Li + 2MnO_2 = LiMn_2O_4 \quad (3)$$

$$Li + LiMn_2O_4 = 2LiMnO_2 \quad (4)$$

The standard Gibbs free energy at 298 K was calculated to be –469 kJ mol^{-1} and –332 kJ mol^{-1} for reaction (3) and (4), respectively. The areal Gibbs free energy is $-17.3 \times t \times 10^9$ J m^{-2} and $-14.3 \times t \times 10^9$ J m^{-2}, where t is the thickness of the interface, and MnO_2 has more negative areal Gibbs free energy compared with Au ($-15.6 \times t \times 10^9$ J m^{-2}), Ag ($-4.5 \times t \times 10^9$ J m^{-2}) and TiO_2 ($-9.5 \times t \times 10^9$ J m^{-2}).[82] Therefore, MnO_2 is one of the best candidates as functional particles on CNT.

Here we present a stable, long-cycle-life Li metal anode enabled by a MnO_2-functionalized 3D porous CNT framework (MO-CNT), as illustrated in Figure 17a. The MnO_2 flakes grafted on CNT not only greatly improved the lithiophilicity of the framework but also increased the surface area of the electrode for lowering the local current density. The improved lithiophilicity was demonstrated by the molten lithium infusion experiments. Molten lithium was attracted into MO-CNT (Supporting video S1) whereas P-CNT repelled molten lithium (Supporting video S2). More importantly, our theoretical calculations show that MnO_2 improves the wetting of the electrolyte as well as distribute Li plating sites. These merits enable uniform Li metal deposition on the MO-CNT surface, as shown in Figure 17b. The mesoporous scaffold provides sufficient

volume to accommodate lithium deposition while CNT offers excellent electrical conductivity for fast charge transfer. As a result, dendrite formation on the electrode surface can be greatly mitigated. On the contrary, when MnO_2 was not coated on CNT (Figure 17c), Li metal was non-uniformly deposited like metal particles (Figure 17d), which often leads to dendrites and dead Li, and thereby results in a low capacity and short cycling. To quantify the performance, two of the most important properties, areal capacity per cycle and total lifetime were considered along with their multiplication to account for both together. This multiplication parameter becomes important because high performances were often claimed with a low areal capacity for demonstrating long lifetime. However, low areal capacities, which are often around 1 mAh/cm^2 or smaller, would not be viable options for fabricating battery cells in practice. Our MO-CNT offered a very long lifetime for more than 1875 hours even at a high areal cycling capacity of 6 mAh/cm^2.

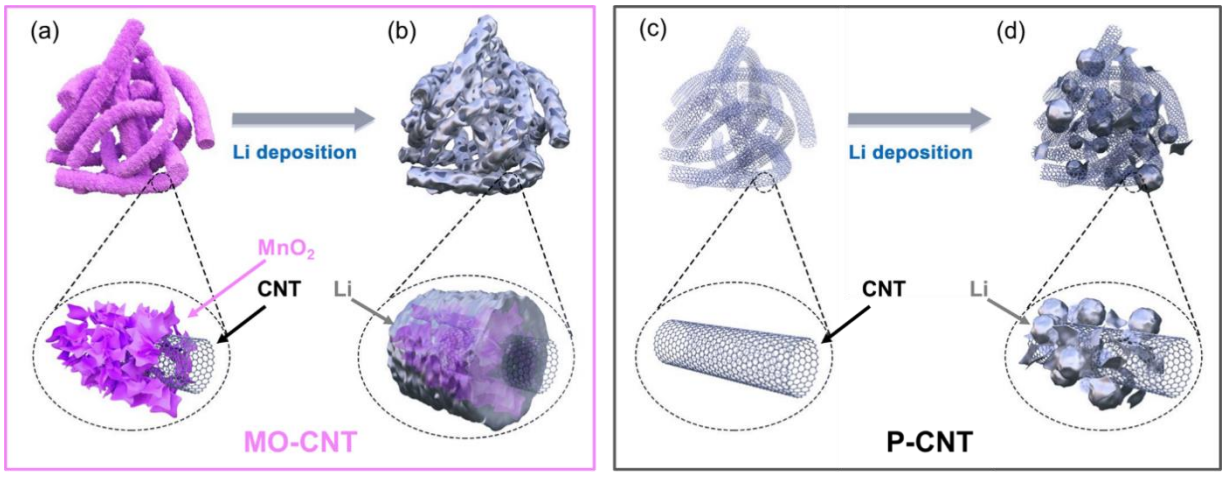

Figure 17. Schematic illustration of (a) MO-CNT, (b) Li-deposited MO-CNT, (c) pristine CNT (P-CNT), and Li-deposited CNT.

4.3. Results and Discussion

4.3.1. Material Synthesis and Characterization

Mossy manganese dioxide was hydrothermally synthesized on the surface of CNTs which were grown to form porous 3D structures using a chemical vapor deposition method.[84, 85] Pristine CNT (P-CNT) initially has a smooth graphitic surface on the tube, as illustrated in Figure 18a and displayed in the scanning electron microscopy (SEM) image of Figure 18d. The synthesis process was initiated with unzipping the graphitic layer of CNT by an oxidative exfoliating agent made of an acidic $KMnO_4$ solution (Figure 18b), showing scrapes on the surface of the tube (Figure 18e). The exfoliation on CNT increases the amount of dangling carbon bond in addition to the surface area, facilitating the manganese ester formation process (Figure 18c). MnO_4^{-1} anion and carbon in CNT can be connected because the bonding energy is found to be lower than that of the separated state. [86, 87] After a short reaction time, manganese ester uniformly covered the surface of CNT and confirmed by the SEM image in Figure 18f and S2b. Transmission electron microscope (TEM) images also show the uniform coverage of MnO_2 on CNT (Figure 18g) and polycrystalline grains of MnO_2 (Figure 18h and S2c). Figure 18i displays MnO_2 clusters with d-spacing of ~0.64 nm along the growth direction of (110) on CNT whose d-spacing between graphitic layers is ~0.33 nm. After synthesis of MnO_2 flakes on CNT, the porous structure still maintains (Fig. S2d), which ensures migration paths for Li ions and electrolyte as well as sufficient volume to accommodate lithium metal depositions.

MO-CNT was further characterized by X-ray diffraction (XRD) and thermogravimetric analysis (TGA). To have clear XRD peaks, the sample was annealed at 200 ℃ for one hour under an argon environment. The diffraction peaks found at 2θ = 12.7°, 18.1°, 28.8°, 37.5°, 42°, 50°, 60.3°, and 65.6° correspond to (110), (200), (310), (211), (301), (411), (521), and (541) crystal planes of α-MnO_2 JCPDS data (44-0141), as displayed in Figure 18j. TGA result indicates ~81 wt% of CNT and ~16 wt% of MnO_2 (see Fig. S3), suggesting the CNT framework is maintained after MnO_2 coating so as to have excellent charge transfer through CNT.

The unique "flake" features on MO-CNT enlarged the surface area and thereby allowed for reducing charge/discharge current per surface area (i.e., current density) compared with P-CNT. The thin layer (a few 10's nm) of MnO_2 appeared to be covalently bonded to graphitic layer of CNT from TEM images, providing stable and lithiophilic nucleation sites for lithium metal plating/stripping without noticeably increasing charge transfer impedance. Density functional theory (DFT) calculation results show that the Mn_8O_{16} particle interacts with a CNT-like surface through O atoms, forming Mn-O-C chemical bonds (Fig. S4), which provides a molecular basis for understanding the MnO_2 synthesis on CNT.

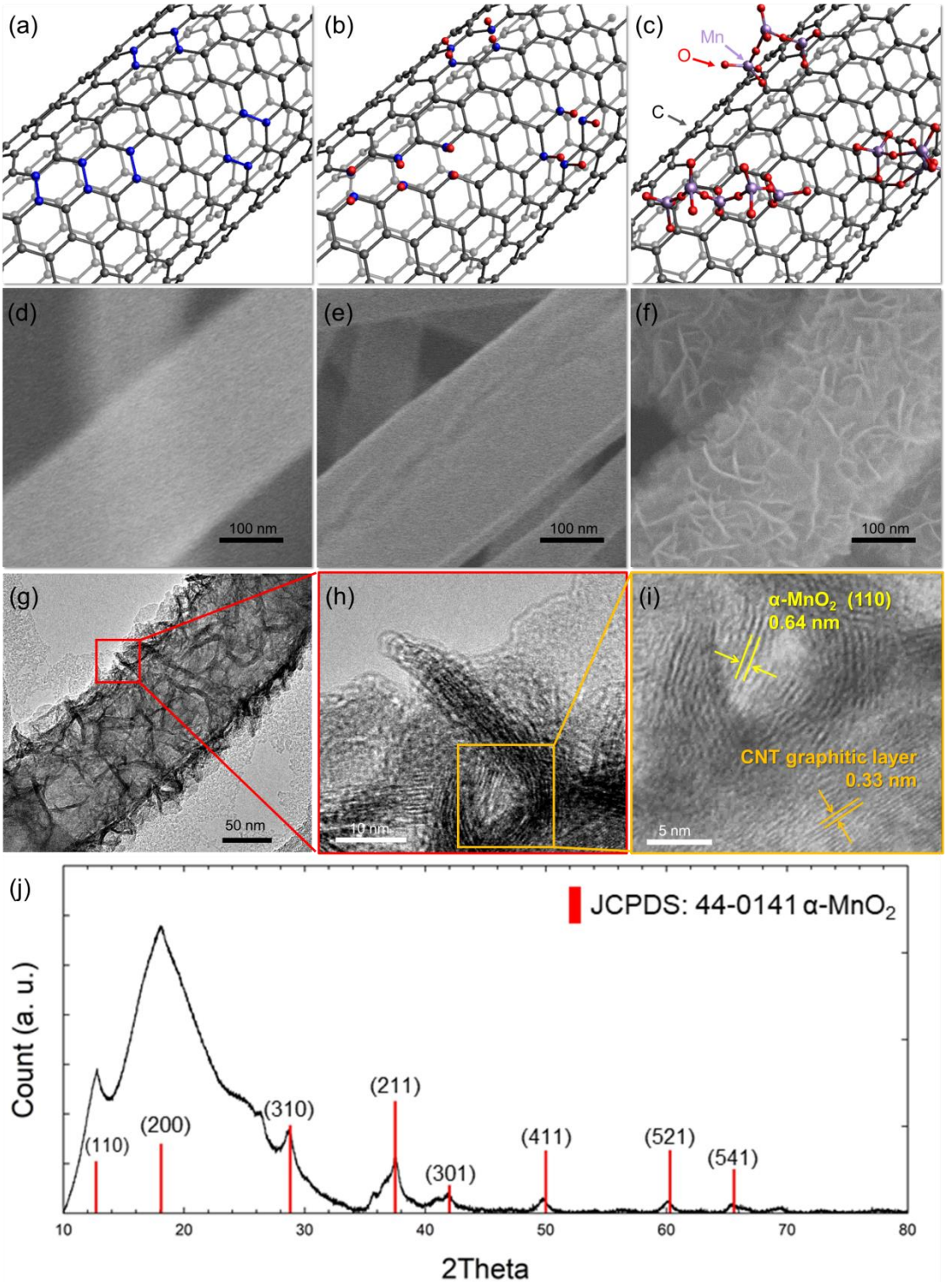

Figure 18. (a-c) Schematic illustration of MnO_2 synthesis on CNT, (d-f) SEM images of MO-CNT synthesis process, (g-i) TEM images of MO-CNT, (j) XRD pattern of MO-CNT after annealing and the corresponding planes for α-MnO_2.

To investigate how lithium is plated and stripped, in-operando studies have been conducted on MO-CNT in addition to CNT and Li metal for comparison with a current density of 1 mA/cm^2 using a pouch cell configuration (Fig. S5). The black MO-CNT and CNT became reddish and volume expanded during the initial lithiation process. Then Li was plated on the CNT electrode until the capacity became 8 mAh/cm^2. The MO-CNT electrode (Figure 19b) did not show dendrites on the outer surface of the electrode whereas the P-CNT (Figure 19f) had Li metal dendrites for the same capacity. Upon Li stripping, the reddish color electrodes turned into black, indicating Li de-intercalation. Li particles were not observable on the outer surface of the MO-CNT electrode (Figure 19c), but the Li dendrites on the P-CNT electrode were seen after de-lithiation (Figure 19g). It should be noted that some of Li particles (bright spots) are firmly attached to the top glass slide rather than those in the electrodes. These immobile particles are readily distinguished when the volume was slightly changed during lithiation/de-lithiation. After running pouch cells, the surface of the P-CNT electrode was covered by Li dendrites (Figure 19h), but MO-CNT electrode did not show noticeable Li layers (Figure 19d).

As a comparative study, we also tested pristine nonporous Li metal (Figure 19i) with the same cycling condition. Repeated plating and stripping caused porous layers with pulverized Li particles (Figure 19j,k), which induces dead Li and large overpotentials and thereby forms Li dendrites easily.[88, 89] The black area in Figure 19l also shows the pulverized Li metal after cycling.

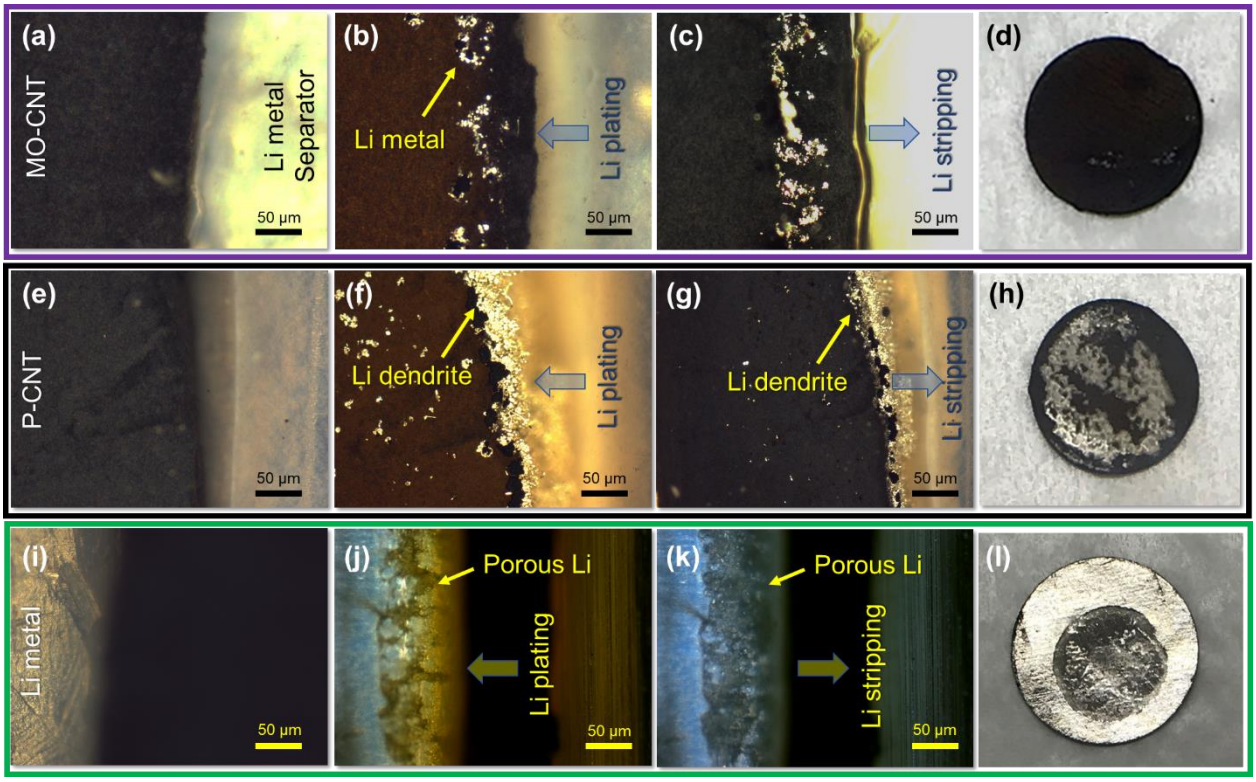

Figure 19. In-operando optical micrographs of MO-CNT, P-CNT, Li metal electrodes (a,e,i) prior to and (b,f,j) after Li deposition, and (c,g,k) after Li stripping, respectively. (d,h,l) Photographs of the electrodes after multiple Li deposition/stripping.

We found that the highly textured surface of MO-CNT (Figure 20a) became smoother after Li deposition (Figure 20b), indicating Li was inserted into the spaces between the mossy structures. We observed that Li was also deposited on P-CNT as the straight outer surface from the graphitic layer of P-CNT (Figure 20e) became wavy after Li deposition (Figure 20f). The cross-section and outer surface (facing the separator) of MO-CNT and P-CNT electrodes were inspected after Li was inserted into the electrodes until the areal Li capacity became 8 mAh/cm^2 with Li metal as counter electrodes in pouch cells. We noticed sharp dendrites emerged from the P-CNT electrode (Figure 20g)

but there was no sign of dendrites on the MO-CNT surface (Figure 20c). Li was densely deposited on the outer surface of the P-CNT electrode, preventing further insertion of Li due to the closed pores (Figure 20h). As the pores get smaller, the migration of Li ions becomes sluggish, leading to drastic lithium dendrite growth on the electrode surface according to Sand's time model.[90] Conversely, the pores in the MO-CNT electrode were visible after the same amount of Li deposition (Figure 20d). This dissimilar Li insertion behaviors could be attributed to more rigorous charge transfer between Li ions and the outer surface (facing Li metal counter electrode) of the P-CNT electrode, compared with MO-CNT. Furthermore, lithiophilic MO-CNT can attract Li ions into the pores while Li insertion into the pores made of lithiophobic P-CNT is comparatively unfavorable.[69] The spherical lithium metal particles on the P-CNT electrode (Figure 20h) were witnessed, which are often caused by nucleation on lithiophobic surfaces.[91]

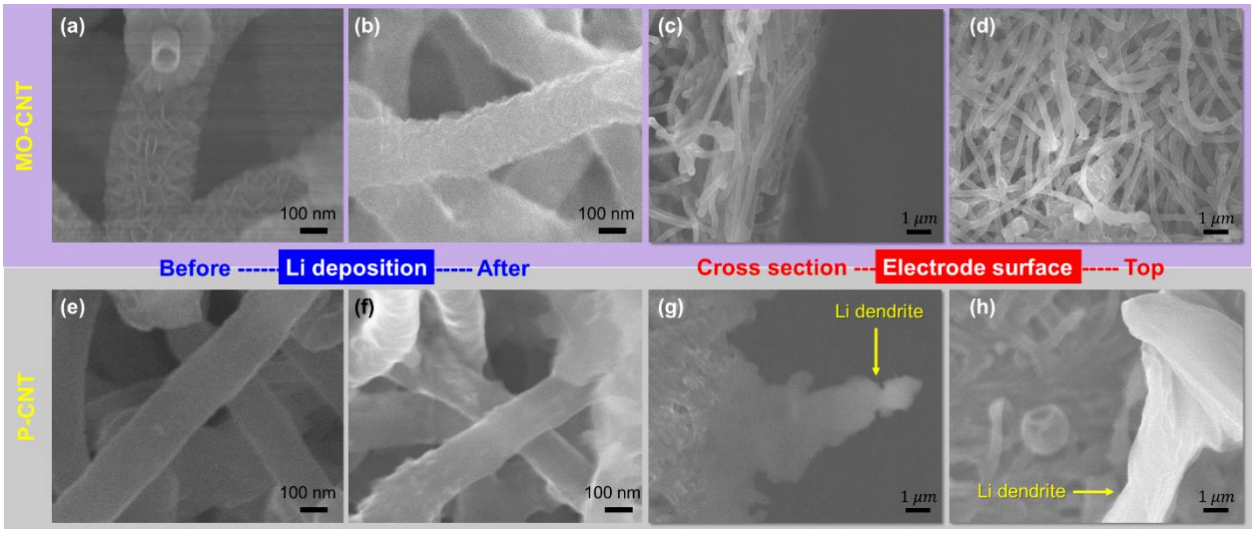

Figure 20. SEM images of MO-CNT and P-CNT (a,e) before and (b,f) after Li deposition, respectively. Cross-sections and electrode surfaces of (c,d) MO-CNT

and (g,h) P-CNT electrodes after Li deposition of 8 mAh/cm^2 with Li metal as counter electrodes. The electrode surfaces face the separator and counter electrode.

4.3.2. Electrochemical Performances and Density Functional Theory (DFT) Calculation

Li plating and stripping performances on the MO-CNT electrode were tested and compared with those of the P-CNT and bare Li metal electrodes by galvanostatic cycling of MO-CNT/Li, CNT/Li, and Li/Li cells with a current density of 1 mA/cm^2. The capacities were set to 1 mAh/cm^2 for the first 10 cycles, then 3 mAh/cm^2 for the following 10 cycles, and then 6 mAh/cm^2 for the rest of testing until the cells failed, as shown in Figure 21a. The MO-CNT/Li cell was able to cycle with stable overpotentials about 40 mV for ~1875 hours (Figure 21a). During the initial cycles with 1 mAh/cm^2, the MO-CNT/Li cell showed very low overpotential (~30 mV), compared with CNT/Li (~60 mV) and Li/Li (~120 mV) (Fig. S6a,b). As the capacity was raised to 3 mAh/cm^2, the Li/Li cell showed drastic voltage fluctuations, but the MO-CNT/Li and P-CNT/Li cells did not have noticeable changes (Fig. S6c,d). Large volume changes in Li metal during stripping/plating due to the limited reaction surface area often cause recurrent formation of new SEI, which could significantly increase the overpotential.[92, 93]

As the capacity was further increased to 6 mAh/cm^2, the CNT/Li and Li/Li cells failed due to the short circuit, which was indicated by the sudden drop of voltage and then flattened voltage profiles, as shown in the insets of Figure 21a. The sudden decrease in voltage and the following square voltage profiles typically indicate cell failures due to short circuit.[94] Rigorous Li plating on the outer surface of P-CNT often causes

catastrophic failure (see Figure 20g). Repeated Li plating/stripping on Li metal also gives rise to porous structures with volume expansion (see Figure 19j,k), resulting in short circuit due to dendrites.[92, 95, 96] We witnessed enlarged overpotentials for MO-CNT before they failed (Figure 21a, S7a,b), indicating MO-CNT was not short-circuited during the long testing time.

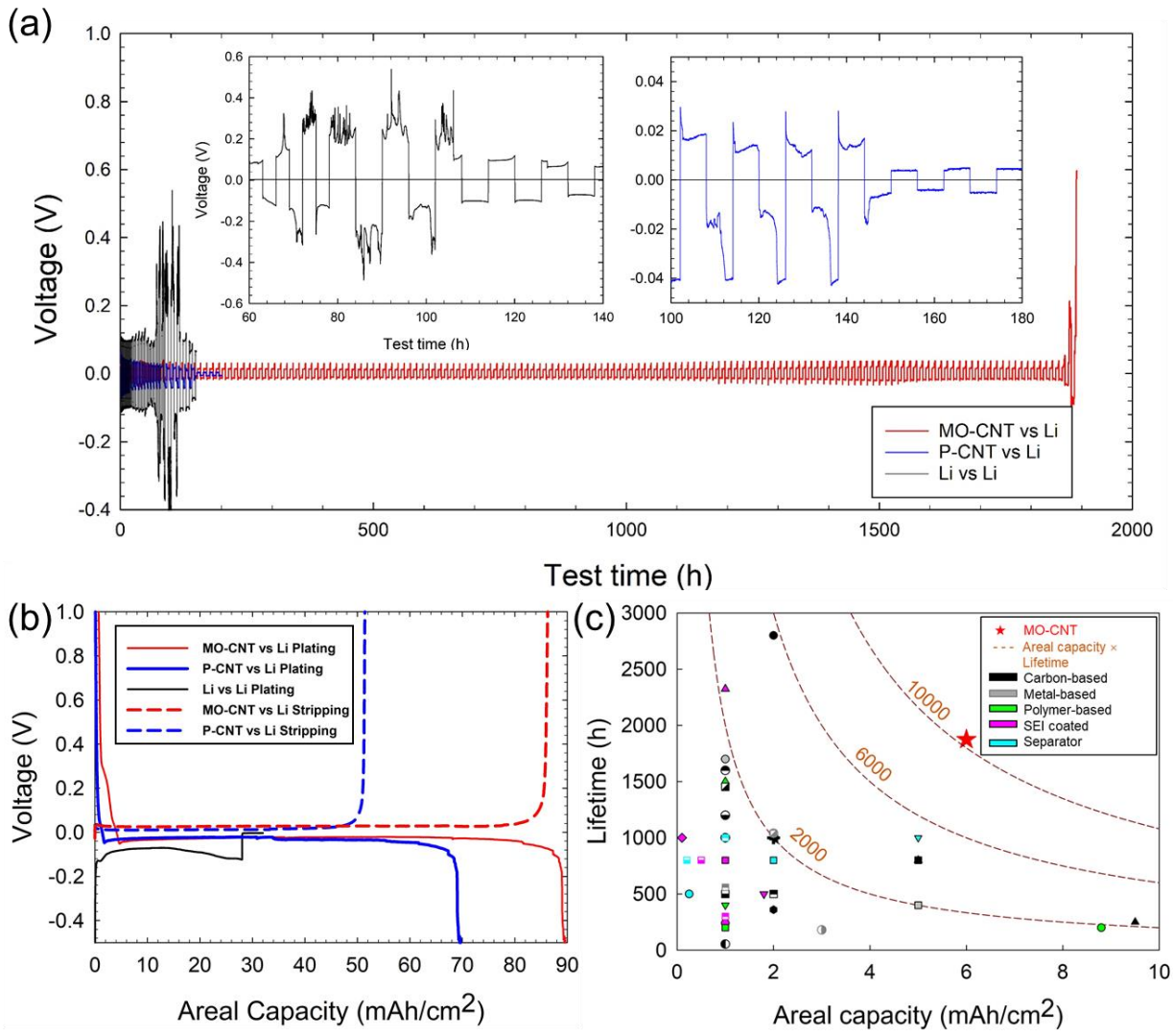

Figure 21. (a) Long-term cycling performances of Li||Li, CNT||Li, and MO-CNT||Li at a current density of 1 mA/cm^2. The charge/discharge capacity started with 1 mAh/cm^2 for 10 cycles, then increased to 3 mAh/cm^2 for another 10 cycles, and

further increased to 6 mAh/cm^2 for the rest of test until the cell failed. The insets show cycling performances of Li||Li and CNT||Li cells when they failed. (b) Voltage profiles during lithium plating/stripping until they were short-circuited or their overpotentials are larger than 500 mV for plating and 1V for stripping so as to test their maximum areal capacities. (c) Performance of MO-CNT, which considers both areal capacity and cycling lifetime. For comparison, literature values for carbon-based,[66, 72, 84, 97-109] metal-based,[68, 110-119] and polymer-based materials,[120-124] SEI-coated Li metal,[123, 125-130] and separator[131-133] were plotted together. More details of literature comparison are included in Table S1.

In the cycling experiments, the capacity was limited up to 6 mAh/cm^2, but there are more rooms for Li to be inserted into the porous structures. To investigate the maximum Li capacity and failure mechanism of these electrodes, Li was deposited on MO-CNT, P-CNT, and Li with a current density of 1 mA/cm^2 until the cells reached overpotential > 500 mV or became short-circuited (Figure 21b). The Li metal electrode can accommodate only 28 mAh/cm^2 of Li, yet CNT and MO-CNT can take Li up to ~69 mAh/cm^2 and ~89 mAh/cm^2, respectively. It is worth noting that 96.6% (86 mAh/cm^2) of Li can be stripped from lithiated MO-CNT electrode, while the Coulombic efficiency is only 72.5% (50 mAh/cm^2) for P-CNT. More importantly, the large amount of Li depositions did not cause short circuit for MO-CNT and P-CNT (only large overpotentials) in contrast to the short-circuit failure of Li metal. Large overpotentials prior to failure allow for taking precautionary measures but unexpected short circuit brings out serious safety concerns in practical application.

When anode performances are evaluated, both cycling lifetime and corresponding areal capacity should be considered at the same time. It is not useful to have long cycling with a small limiting capacity and large capacity lasting only a short period of time. Here, we assess a parameter given by multiplication of areal capacity and

lifetime,[134, 135] as shown in Figure 21c. We compared the capacity-considered lifetime of MO-CNT with other anodes made of carbon-based,[66, 72, 84, 97-108] metal-based,[68, 110-119] and polymer-based materials,[120-123] SEI-coated Li metal,[123, 125-130] and separator.[131-133] Performance of metal-based lithium metal anode is compromised by either low areal capacity or short lifetime due to the low surface area and poor lithiophilicity. Conductive polymer shows advantage for high areal capacity, while the lifetime is too short for practical application. Even though the resilient polymer framework could accommodate volume fluctuation, poor electrical conductivity could still cause failure in anode. SEI-coated lithium metal anode and modified separator could only survive for a short lifetime at low areal capacity condition. The delicately coated SEI and separator could not effectively suppress the dendrite formation especially in high areal capacity condition. Carbon-based material could be a promising candidate because of good electrical conductivity and high surface area. It is worth noting that MO-CNT in this work can deliver an outstanding performance parameter, considering areal capacity and lifetime, over 10,000 mAh^2/cm^2, which is much higher than others in the literature (mostly under such parameter of 6,000 mAh^2/cm^2). For the comparison, areal capacity was selected instead of specific capacity because specific capacity widely varies depending on the amount of electrolytes (or porosity) in actual cells but this information is typically unavailable in literature.

Electrochemical impedance spectroscopy (EIS) was conducted at six different stages to further unveil the benefit of MnO_2 on CNT by comparing EIS data from MO-CNT, CNT, and Li metal (Figure 22a, Fig. S8): (1) at the initial stage, (2) after full

lithiation (0 V), (3) after Li plating up to 8 mAh/cm^2 onto the electrode, after a stripping/plating cycle with a capacity of (4) 1 mAh/cm^2, (5) 3 mAh/cm^2, and (6) 6 mAh/cm^2. Li electrode starts from stage (2) since it does not need lithiation. Charge transfer resistance (R_{ct}), in Figure 22b, represents ion migration and charge transfer through the interface between electrode and electrolyte. At the initial stage, we found that R_{ct} (300 Ω) for MO-CNT is much lower than those of P-CNT (2300 Ω) and Li metal (2650 Ω) despite the low conductivity of MnO_2. This interesting result could be attributed to the favorable wetting on MnO_2, compared with lithiophobic graphitic surface of P-CNT and native oxide layers on Li metal.[136] DFT calculations show that the interaction energy between 1,3-dioxolane (DOL) solvent molecule and MnO_2 on CNT improves from -0.26 eV (DOL and CNT system) to -1.06 eV (DOL and MnO_2/CNT system). Charge density difference (CDD) analysis (Figure 22d) demonstrates the improved charge accumulation between the O atom of DOL solvent molecule and the Mn atom of MnO_2. Bulk resistance values, which includes ionic resistance of electrolyte and separator and electrical contact resistance, for MO-CNT were consistently lower than the others regardless of the stage (Fig. S9).

After lithiation (stage 2), R_{ct} of MO-CNT significantly dropped to 50 Ω, which could be ascribed to the good affinity between MnO_2 and Li ions, yet R_{ct} of P-CNT was barely changed, alluding the wetting is still unfavorable. After lithium plating (stage 3), R_{ct} of MO-CNT was reduced a bit further and maintained thereafter. However, R_{ct} values of P-CNT and Li were still relatively large after Li plating of 3 mAh/cm^2 and then suppressed with larger Li plating (stage 5,6), which may signify unstable deposition of

Li and cracking/formation of SEI.[84] This is in accordance with the unstable polarization in the voltage profile of CNT and Li (Figure 21a). The ion diffusivity of MO-CNT in Figure 22c was remarkably enhanced after lithiation compared with those of P-CNT and Li metal.

To further unveil how Li plating/stripping became favorable by decorating MnO_2 on CNT, we studied the sequential insertion of Li in MOCNT by carrying out Monte Carlo searches[137] of the configurational space to find low energy adsorption sites for Li binding energy DFT calculations. As lithiation progresses, Li ions coordinate with O atoms and tend to be dispersed across the MnO_2 cluster, interacting with the available O atoms (Figure 22e,f,g). This tendency suppresses vertical growth of Li metal and promotes the horizontal growth of Li clusters. The benefit of this configuration is also additional lithiophilic sites at the MnO_2/CNT interface, which favor Li deposition and nucleation (Figure 22g), showing that Li-ions interact with both the CNT structure and the MnO_2 cluster.

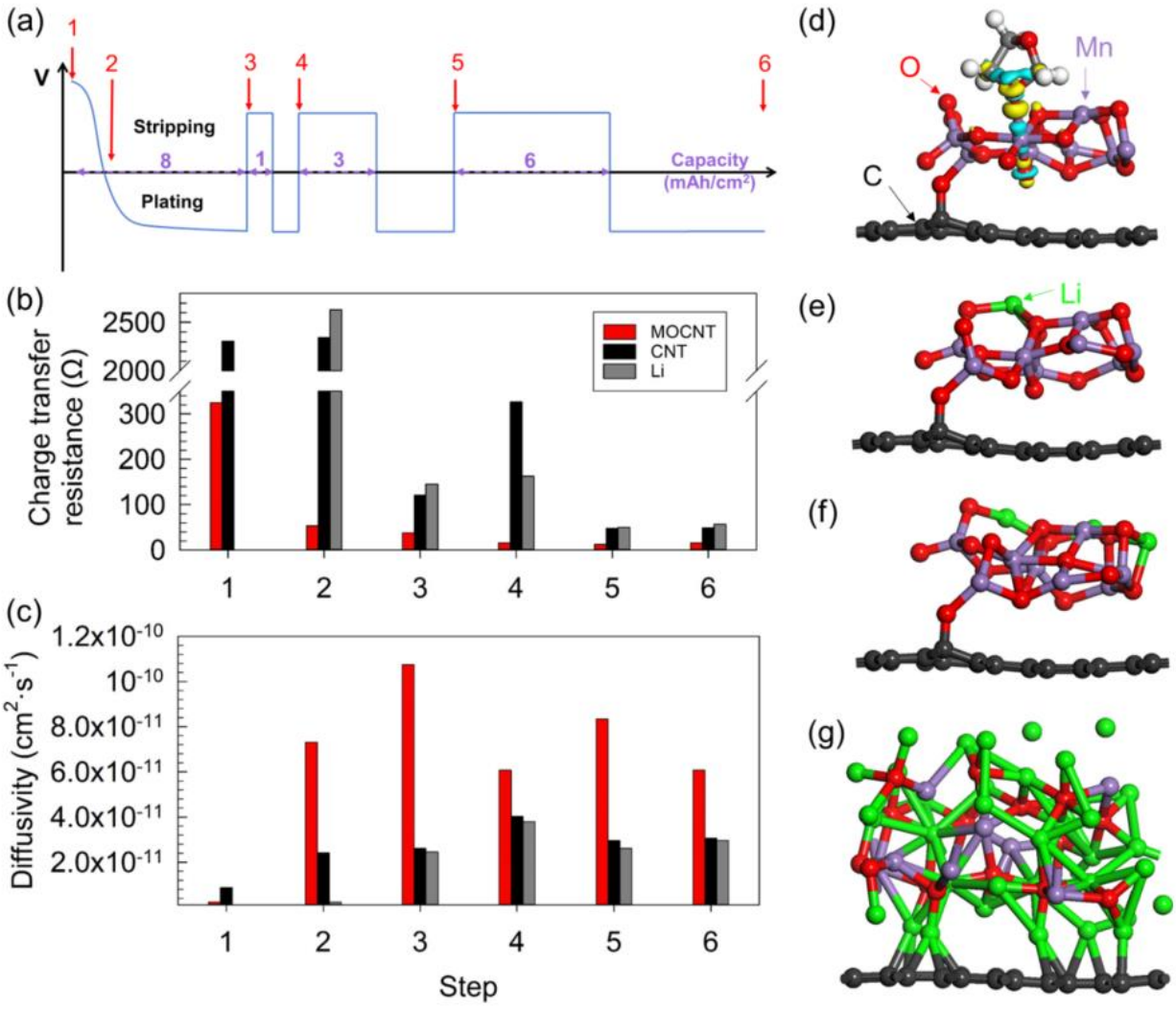

Figure 22. (a) Illustration of test points for EIS, (b) charge transfer resistance, and (c) diffusivity at the stages of (1) before lithiation, (2) after full lithiation, (3) plating of Li up to 8 mAh/cm^2, after a stripping/plating cycle with capacities of (4) 1 mAh/cm^2, (5) 3 mAh/cm^2, and (6) 6 mAh/cm^2. (d) CDD analysis of DOL solvent molecule interacting with MnO_2/CNT structure. The yellow and blue isosurfaces correspond to charge gain and lost regions, respectively. Optimized models of (e) one, and (f) three Li atoms adsorbed on the MnO_2/CNT system. (g) Lithiated MnO_2/CNT system showing Li intercalated at the interface between CNT and MnO_2. Color code: black, red, green, and purple spheres represent C, O, Li, and Mn atoms, respectively.

These behaviors can be explained from a thermodynamic standpoint. Lithium's binding energy calculations show favorable energies (around –3.5 eV) for the initial Li deposition on the MnO_2/CNT system. Taking the calculated lithium's cohesive energy as a reference point, the binding energy profile shows that after 36 Li atoms inserted (see vertical dashed lines in Fig. S10a), Li would prefer to form Li-Li bonds. This preference is because beyond this lithiation content, the Li-MnO_2/CNT interaction is weaker than the Li-Li interaction. Moreover, Fig. S10b shows that, after 36 Li atoms are inserted to the MnO_2/CNT system, the number of isolated Li groups reduces and the number of Li-Li bonds continue to increase. That is, with an increase in the number of Li in the system, there is an increased association of Li atoms. Note however, that this increased association of Li atoms results in the horizontal growth of Li clusters. On the other hand, similar to what has been reported in literature [138], our static DFT calculations at 0 K for the lithiation of the CNT-like structure (Fig. S11) show positive Li-ion binding energies except for the 1st Li-ion intercalation, indicating that Li-ions do not bind on pristine CNT-like structures. Thus, the simulations predict that the phase separation of pristine graphene and bulk Li is energetically preferred. Moreover, as calculated recently by Niu and co-workers[107], vertical growth of Li clusters takes place on a graphene surface.

4.4. Conclusion

Mossy MnO_2-decorated mesoporous CNT structures were tested as anodes for plating and stripping Li metal along with pristine CNT structures and Li metal for comparison.

This MO-CNT provided an extremely high performance parameter over 10,000 mAh^2/cm^2, which considers both cycling lifetime and areal capacity, even with large Li plating/stripping capacity of 6 mAh/cm^2 for more than 1800 hours. The conspicuous improvement can be attributed to the uniformly distributed Li insertion through large surface areas of the mossy structure, lowering the local current density and thereby suppressing dendrite formation. ElS results show MnO_2 grafting on CNT significantly improved charge transfer resistance, ion diffusivity, and bulk resistance. DFT results discover that the MnO_2/CNT system provides additional lithiophilic sites at the MnO_2/CNT interface that favors the stability of the structure with Li and Li nucleation. Moreover, the simulations provide an atomic level understanding of the DOL solvent molecule interaction with the MnO_2/CNT system that helps to understand the improve wettability of this system compared to the bare CNT system. Overall, these results provide an understanding of mechanisms involved in the lithiophilic improvement of a mesoporous CNT sponge and a demonstrated viable strategy for practical application of Li metal anode. This application is a step forward towards achieving a large capacity and stable cycling performance in Li metal-based rechargeable battery systems.

4.5. Experimental Section

Preparation of CNT electrodes: 3D porous carbon nanotubes (CNTs) were synthesized by a chemical vapor deposition (CVD) method following our earlier work.[5, 85] A crucible filled with ~0.3 g ferrocene (Sigma-Aldrich, 98%) was placed in zone 1 (upstream) of a quartz tube whose inner diameter is ~22 mm. During the growth, hydrogen (Airgas, 99.999%), ethylene (Airgas, 99.999%), and argon (Airgas, 99.999%)

gases were flowed into the tube at flow rates of 260 sccm, 80 sccm, and 80 sccm, respectively. The argon gas was passed through a bubbler filled with deionized (DI) water at room temperature. The furnace temperatures of zone 1, zone 2 and zone 3 (CNT growth zone) were 120 °C, 120 °C, and 650 °C, respectively.

Preparation of manganese oxide decorated CNT (MO-CNT) electrodes: MO-CNTs were synthesized by a facile hydrothermal reaction. 0.05M $KMnO_4$ (AMRESCO, >99%) solution was prepared in deionized (DI) water. The pH value of the solution was adjusted to 2 by adding HCl (Macron Fine Chemicals, 36.5%-38.0%). CNT slices and the reaction solution were pre-heated in a temperature-controlled oven at 90 ℃ for 30 min. The CNT slices were immersed into the solution and kept in the oven for 30 min. After the hydrothermal reaction, the CNT slices were taken out and rinsed with sufficient DI water. Finally, the MO-CNT was dried in the oven at 50 ℃ overnight before use. Typical sample thickness ranges from 200 to 500 μm.

In-operando pouch cell assembly and testing: In-operando cells were fabricated using pouch cell films with a cover glass (thickness No.1) as a viewing window (see Fig. S4). Copper foils wrapping around typical microscope glass slides (thickness: ~1 mm) were used as current collectors on top of another glass slide. CNT and lithium metal (Alfa Aesar, 99.9%) were placed in the middle with a Celgard 2400 separator in between, and then the two glass slides with the current collectors were pushed against each other. The amount of the electrolyte (1 M LiTFSI (Sigma-Aldrich, 99%) and 0.5 M $LiNO_3$ (Alfa Aesar, 99%) in a mixture of 1,3-dioxolane (Alfa Aesar, 99.5%) and 1,2-dimethoxyethane (Alfa Aesar, 99+%) (1:1 by vol.)) was 500 μL to fill in the pouch cell.

All the lithium insertion processes were carried out with a constant current density of 1 mA/cm^2 without formation cycles. Dark-field optical microscope (Olympus BX5) images were taken every 1 minute using Q capture Pro program and made a video by an image merging program (Openshot Video editor).

Electrochemical impedance spectroscopy (EIS) measurement & analysis: EIS measurements were performed with Gamry 1010E electrochemical workstation and Arbin battery tester. The impedance spectra were recorded with an amplitude of 5 mV over the frequency range from 1 MHz to 0.01 Hz. The results were fitted to typical equivalent circuit with Gamry Echem Analyst. The real part of impedance (Z_{Re}) can be expressed as:

$$Z_{Re} = \delta\omega^{-1/2} \quad (1)$$

where δ is Warburg factor and ω (unit: Ω s$^{-0.5}$) is angular frequency (= $2\pi f$, where f is frequency). From the experimentally obtained relation between Z_{Re} and $\omega^{-1/2}$, δ can be found by linear fitting.

$$\delta = \frac{RT}{An^2F^2\sqrt{2}}\left(\frac{1}{\sqrt{D}C}\right) \quad (2)$$

where R is gas constant (8.314 J K^{-1} mol^{-1}), T is temperature (298 K), A is electrode area (0.7125 cm^2), n is reactant ratio, F is Faraday constant (96500 C mol^{-1}), D is diffusivity (cm^2 s^{-1}) and C is ion concentration (mol L^{-1}). Note that A is the area facing the lithium metal. C is the initial lithium ion concentration, 1.5 M, and n is 1 for lithium ion redox reaction ($Li^+ + e^- \rightarrow$ Li (metal)). EIS data were fitted using the equivalent circuit in Fig. S1. R_u refers the electrolyte solution resistance within the cell and the intrinsic resistance, including the contact resistance and the resistance within the active materials. R_p, Y0, and W_d, represent the contact resistance, constant phase element and Warburg coefficient,

respectively.

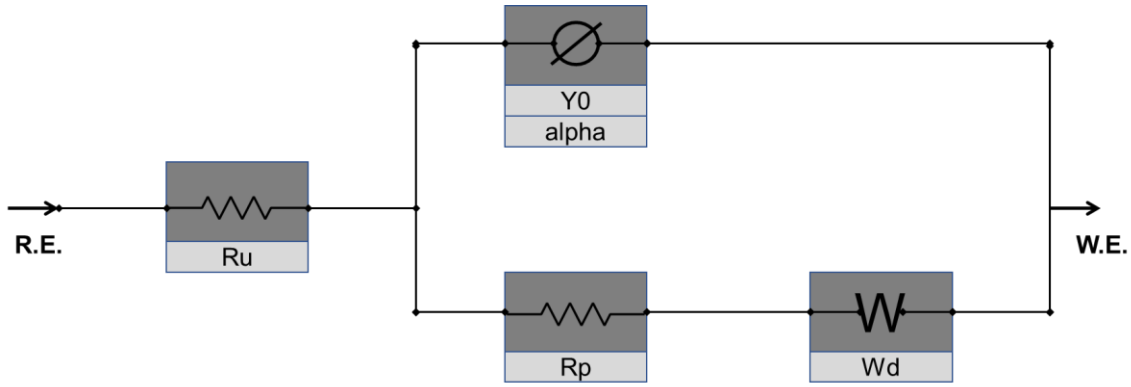

Figure 23. Equivalent circuit for EIS data.

4.6. Computational Methodology

Density functional theory (DFT) calculations were performed using the Vienna ab initio simulation package (VASP) code with the projector augmented wave (PAW) pseudopotentials.[54, 139-141] Generalized gradient approximation (GGA) of Perdew–Burke–Ernzerhof (PBE) functionals were used to implement electron exchange-correlation interactions with a kinetic energy cutoff of 400 eV.[56] The van der Wals (vdW) interaction was described with DFT-D3 method.[142] The self-consistent field (SCF) and geometry convergence tolerance were set to 1×10^{-4} and 1×10^{-3} eV, respectively. A Γ-point-centered Monkhorst−Pack reciprocal grid of 3×5×2 k-points was used for first Brillouin zone sampling.[143] On-site Coulomb interactions were included by using the DFT+U formalism of Dudarev and co-workers.[144] For Mn atoms, an on-site coulomb interaction parameter of U = 3.9 eV was implemented.[145] To avoid interactions arising from periodic boundary conditions, a vacuum space greater than 10 Å was introduced in the normal direction.

To study the interaction of a CNT/MnO_2 system with Li, the CNT structure was approximated as a 12.78 Å × 7.38 Å planar single layer graphene structure. Meanwhile, the MnO_2 system was approximated as a Mn_8O_{16} cluster carved out from an optimized MnO_2 bulk system. Moreover, we used a 12.78 Å × 14.76 Å planar single layer graphene structure to calculate the binding energy of Li atoms onto this structure. The Li binding energies were calculated using the following equation:

$$E_B = \frac{(E_{Total} - E_{Substrate} - (n \times E_{Li}))}{n} \quad (3)$$

Here, E_{Total} is the energy of the total system, $E_{Substrate}$ is the energy of the unlithiated CNT or MO-CNT structure and E_{Li} is the calculated cohesive energy of Li (-1.60 eV) and *n* is the number of Li atoms inserted. To explore the interactions of the solvent with the bare CNT structure and the CNT/MnO_2 system, we conducted an interaction energy and charge density difference (CDD) analysis of a DOL solvent molecule interacting with both systems. The interaction energy (E_{IE}) is defined in the following way:

$$E_{IE} = (E_{Total} - E_{Slab} - E_{DOL}) \quad (4)$$

Here, E_{Total}, E_{Slab} and E_{DOL} represent the energy of the total system, the energy of the slab (without DOL molecule) and the energy of the DOL molecule, respectively.

Calculation of Areal Gibbs Free Energy

$$\text{Areal Gibbs free energy } \left(\mathrm{J}/\mathrm{m}^2\right) = \frac{\text{standard Gibbs free energy} \times \text{density}}{\text{molar mass}} \times \text{thickness}(t)$$

$$Li + 2MnO_2 = LiMn_2O_4 \quad (5)$$

$$Li + LiMn_2O_4 = 2LiMnO_2 \quad (6)$$

The standard Gibbs free energy at 298 K was calculated to be -469 kJ mol^{-1} and -332 kJ mol^{-1} for reaction (5) and (6), respectively. Thickness *t* (m).

Areal Gibbs free energy for (5)

$$= \frac{-469(\mathrm{kJ/mol}) \times 1000 \times 4.02(\mathrm{g/cm^3})}{108.8(\mathrm{g/mol})} \times t \times 1000000$$

$$= -17.3 \times t \times 10^9(\mathrm{J/m})$$

Areal Gibbs free energy for (6)

$$= \frac{-332(\mathrm{kJ/mol}) \times 1000 \times 4.04(\mathrm{g/cm^3})}{93.9(\mathrm{g/mol})} \times t \times 1000000$$

$$= -14.3 \times t \times 10^9(\mathrm{J/m})$$

5. OPTIMIZED PARAMETERS FOR FAST CHARGING/DISCHARGE AND LONG CYCLE LITHIUM SULFUR BATTERY

5.1. Abstract

Lithium sulfur battery is one of the most promising candidates for next-generation energy storage device beyond lithium ion battery. Practical application of lithium sulfur battery is still hindered by several problems, including poor cycling life, sluggish charging/discharging kinetics, inferior cell-level gravimetric and volumetric energy density. Thick cathode was proposed to accommodate high sulfur loading. However, gravimetric and volumetric energy density cannot be improved due to poor sulfur utilization and excessive amount of electrolyte. In addition, recent electrical vehicles and portable electronics require fast charging/discharging, which is even more challenging for lithium sulfur battery. For this scenario of application, thin cathodes are more preferable due to fast charge transfer and better ionic diffusion. However, thick cathode is preferred for high loading of active material since it can provide sufficient pore volume to accommodate polysulfide and alleviate shutting effect. Meanwhile, high loading and thick cell could lead to poor utilization of active material due to long diffusion length for lithium ion. Additionally, large deposition of Li_2S solid could block the diffusion path and exacerbate the polarization which could shorten the lifespan of battery, especially in high c-rate application. Although the phenomena have been observed by researchers, the reasons behind are still not revealed. To facilitate the commercial application of lithium sulfur battery, we have to face the dilemma of selecting proper thickness and loading of active material for different c-rate application

and targeted lifespan. Here, we firstly studied thickness-dependent performance for high c-rate and long lifespan lithium sulfur battery. It is found that performance decays drastically after certain increasement of cathode thickness. Rate capability was investigated to find proper thickness without sacrificing the loading. We proposed a multi-layer-cathode consist of a buffer layer to alleviate Li_2S aggregation and a polysulfide reservoir layer to confine the active material. The cell with selected thickness can cycle more than 1500 times at 1C. The limiting factors for thick cathode, high c-rate application, and large loading are further investigated by COMSOL simulation. Rate capability is mainly limited by clogging issue on the cathode surface. Application of large loading is limited by poor diffusion of lithium-ion and depletion of lithium-ion inside the cathode. Both of the factors limited utilization of thick cathode.

5.2. Introduction

Polysulfides are intermediate products during the cycling the of Li-S battery. Since the polysulfides are highly soluble in the electrolyte and large concentration gradient across the separator, the shuttle effect from cathode to anode could leads to anodic corrosion, consumption of electrolyte, and loss of active material.[36, 52, 146, 147] Numerous research efforts have been devoted to confine polysulfide diffusion across the separator.[148-151] Physical and chemical adsorptions are effective approaches to immobilize polysulfide species.[152-156] Porous carbon scaffold is a promising candidate for polysulfide reservoir, benefiting from its outstanding electrical conductivity, strong mechanical property, high porosity, and light weight. In addition to physical confinement, chemical adsorptions can be realized by conductive polymer[47], heteroatom-doped carbon[5], and metal

oxides/sulfides[157-159], etc. Mechano-chemically treated carbon nanotube (CNT) with trenches along the tube has shown outstanding polysulfide attraction.[5] Free-standing, three-dimensional CNT sponge works very well as a conductive framework with outstanding polysulfide-philic performance[5]. In order to enable this technology to be readily applied in large scale fabrication and compatible with industrial infrastructure. We prepare the material with slurry method, which is developed for LIB production line. Slurry method not only enable large scale manufacturing, but also allows us to synthesis cathode with desired thickness. If the battery is applied for frequently fast charging and discharging, such as energy-grid storage, thinner cathode could satisfy the needs. If energy density is more important when used to power drone or other portable electronics, relative thick cathode can store more energy with given accessories.

Although shuttling effect of polysulfides could cause loss of active material, low Coulombic efficiency, and capacity degradation, the active material loading in a form of catholyte could benefit the performance in multiple ways.[160, 161] (1) Electrochemically active polysulfide can facilitate active material utilization. Evenly distributed polysulfides could promote fast interfacial reactions, especially in high C-rate conditions.[162] The sluggish reaction and poor sulfur utilization of solid sulfur can be localized mainly on the sulfur-carbon interface.[163] (2) Dispersing polysulfides into conductive matrix could achieve homogeneous distribution of the active material. Extensive work has been done to load solid sulfur into the framework, such as molten infusion, sulfur nano-particles, slurry of sulfur and carbon mixture, etc. However, Aggregation of elemental sulfur is

unavoidable, and, at the beginning of cell operation, the redistribution of sulfur during cycling could be problematic.

Thickness of the cathode is a critical factor for the cell-level performance.[164, 165] Thin cathode can have several advantages. Thin cathode could be applied in high C-rate scenario.[166, 167] With given sulfur to carbon ratio, the thinner cathode has better electrical conductivity due to relatively low areal sulfur loading. Fast ionic diffusion could be facilitated since less diffusion barrier and tortuosity for thin cathode.[168, 169] Due to relatively more evenly distributed end product, the "local" E/S ratio is still maintained in proper range.[170, 171] However, if the cathode is too thin, the limited sulfur loading hindered Li-S battery for commercial application. Additionally, thin cathode cannot work as effective polysulfides reservoir due to limited pore volume. It is reported that thin cathode has severe capacity decay compared to thick cathode[172], even though thin cathode could have higher initial capacity. Thus, designing a thick cathode is essential for commercial application of Li-S battery[173-175]. Thickness of an cathode needs to be carefully considered because thick cathode could lead to many drawbacks. Thicker cathode could have poor ionic diffusivity due to long and tortuous charge transfer and diffusion path. It is also one of the reasons that thick cathode could have inferior C-rate performance compared to the counterpart. One goal of applying thick cathode is to achieve high areal S loading. This could also lead to poor mechanical stability due to frequent and large volume change during discharge/charge. Additionally, high areal loading of thick cathode requires more Li stripping/plating. Thus, volume change is severer and more challenging to the mechanical stability. More unavoidable side reaction between Li and electrolyte could

shorten the anode lifespan and aggravate electrolyte depletion. Since the redistribution of end product is uneven across the cathode,[176] the aggregated precipitation could cause very lean "local" E/S ratio. The simulation and in-operando results show that Li_2S is more preferable to be deposited in the region closer to the separator while S is more accumulated around the current collector side. Overall, thickness of the cathode needs to be improved for different scenarios of application, such as high energy density, long life, and fast charge/discharge.

Adding interlayer could be effective way to limiting polysulfide diffusion, however fast lithium-ion diffusion needs to be maintained[150, 177-180]. Since the polysulfide diffusion is limited by the interlayer, more negative ΔG means better electrochemical reaction kinetics. The interlayer needs to be conductive to ensure fast charge transfer and porous for fast lithium-ion diffusion. Pristine-CNT could work as effective interlayer due to its repelling property to polysulfide, good electrical conductivity, and porous feature for fast lithium-ion diffusion.

Thickness-dependent performance test is conducted with various c-rate. The interlayer significantly improved capacity and cycling life. Scanning electron microscope (SEM) results provide details information for the hypothesis that end product deposition behaviors varies for the cathodes with different thickness. Theoretical simulation is performed to reveal how the concentration of species evolved during charge and discharge.

5.3. Results and Discussion

According to aforementioned theorem, distribution of end product could be different due to high local concentration gradient and unreacted end product. Here, we designed an experimental setup for the in-operando study. Sulfur was sandwiched between two pristine CNT sponge cathodes to construct a cathode by a cold-press method, as shown in Figure 30. With this configuration, we have successfully observed the cross-sectional morphology of cathode while cycling. The current result demonstrated that sulfur does not return to the original location once cycled, it appears that sulfur particles tend to preferentially nucleate around the current collector side while Li_2S particles tend to preferentially nucleate around the separator side of cathode. The sulfur can be clearly seen under an optical microscope before discharging as shown in Figure 24(a,b). The image of the battery at discharged state (Figure 24c,d) shows that sulfur disappeared and small Li_2S particles presented on the side closer to separator. At the charged state, the Li2S particles are gone and sulfur particles were nucleated around the edge contacting with the current collector as shown in Figure 24(e-f). It is apparent that sulfur can be easily redistributed during charging process because sulfur disappeared from original location after charge/discharge. During discharging process, Li_2S was seen more abundantly near the separator side. This is presumably because Li+ concentration is higher at the separator (anode) side. As Li+ converts to Li_2S need to consume lithium ion, this may indicate that the process is limited by ion diffusion. During charging process, the sulfur deposition was observed at the current collector side. As lithium

polysulfides donate electrons to become sulfur, this may indicate this process is limited by polarization.

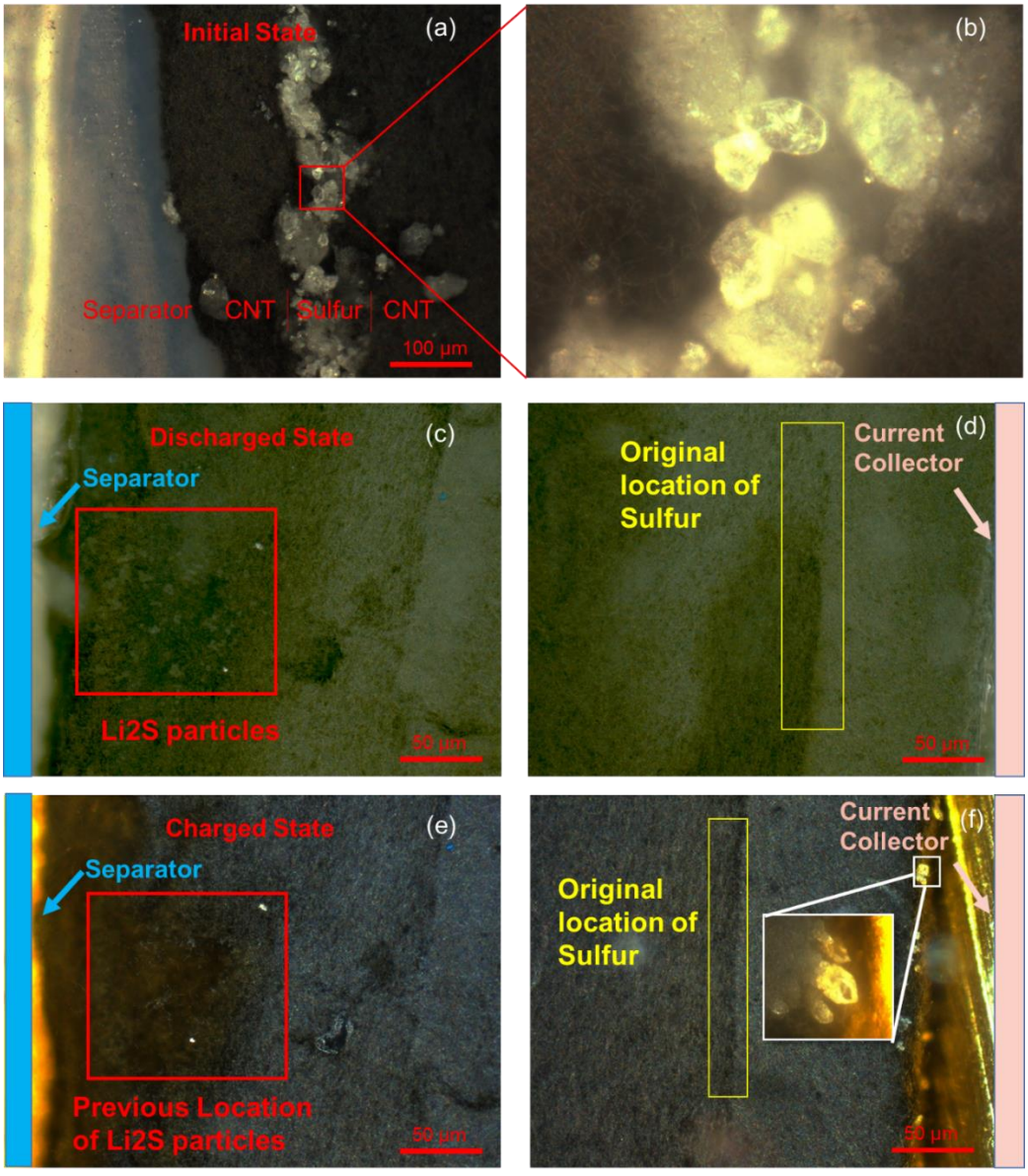

Figure 24 In-operando observation of sandwiched Li-S battery. (a) Initial location of CNT cathode and loading of sulfur. (b) Initial state of sulfur particle. (c) At discharged state, Li_2S deposition on the cathode region near the separator. (d) Disappear of sulfur at the initial location. (e) At charged state, Li_2S disappeared and sulfur particles deposited on the region near the current collector.

Since lithium-ion diffusion and polarization of species could limit the utilization of active material, it is critical to find proper configuration of cathode for different conditions, such as discharging/charging rate, loading, E/S ratio, etc. In order to find the proper parameters for high c-rate and long-cycle performance, we firstly tested the cathode with various thickness. The sulfur was loaded with 1M Li_2S_6 catholyte. Sulfur to carbon ratio was controlled to be 1:5, in which volume fraction of sulfur and carbon is 0.04 and 0.2, respectively. The cathodes with thickness of 80μm, 100μm, 140μm, 160μm, 180μm, and 220μm are tested at C-rate of 0.6C, 1.2C, and 3C, as shown in Figure 25 (a,b). As the thickness increased, the cells achieved improved specific capacity and utilization of active material since more effective polysulfide reservoir. The acid-treated CNT cathode with thickness of 180μm (ACNT-180) demonstrated most outstanding performance of 1650 mAh/g at 0.6C, 1500 mAh/g at 1.2C, and 1300 mAh/g at 3C. In the case of ANCT-180, capacity only decays 9% when C-rate increases from 0.6C to 1.2C. However, the degradation is severer at 3C, which is about 13.3%. Samples with thickness from 80μm to 180μm shows similar capacity degradation at different rates since ionic diffusion and charge transfer are still effective due to proper thickness. Beyond cathode thickness of 180μm, capacity drops drastically for all c-rates. This is due to high consumption of lithium ion for the thick cathode while lithium-ion diffusion is limited. Accumulation of Li_2S solid further narrows the diffusion path of lithium-ion and exacerbate the polarization. The depletion of lithium-ion and building-up of Li_2S are revealed by COMSOL simulation. ACNT-220 shows very low specific capacity in the first a few cycles due to unreacted material caused by insufficient Li ion inside the

cathode. In the final cycles at 0.6C, the “dead” sulfur is reactivated, specific capacity reaches 1100~1200 mAh/g, which is in the same range as the thinner counterparts. It worth noting that the thick cathodes are able to recover to 1500 mAh/g in the last 5 cycles, which demonstrated outstanding performance of the thick cathode as a polysulfide reservoir at low c-rate. The result shows that thickness of the cathode can prominently affect the sulfur utilization, which could attribute to reagent diffusion across the cathode, concentration polarization, electrical conductivity, and product redistribution. Moderate thickness should be carefully selected, especially for high c-rate performance, long cycling capability and considering applicable sulfur loading.

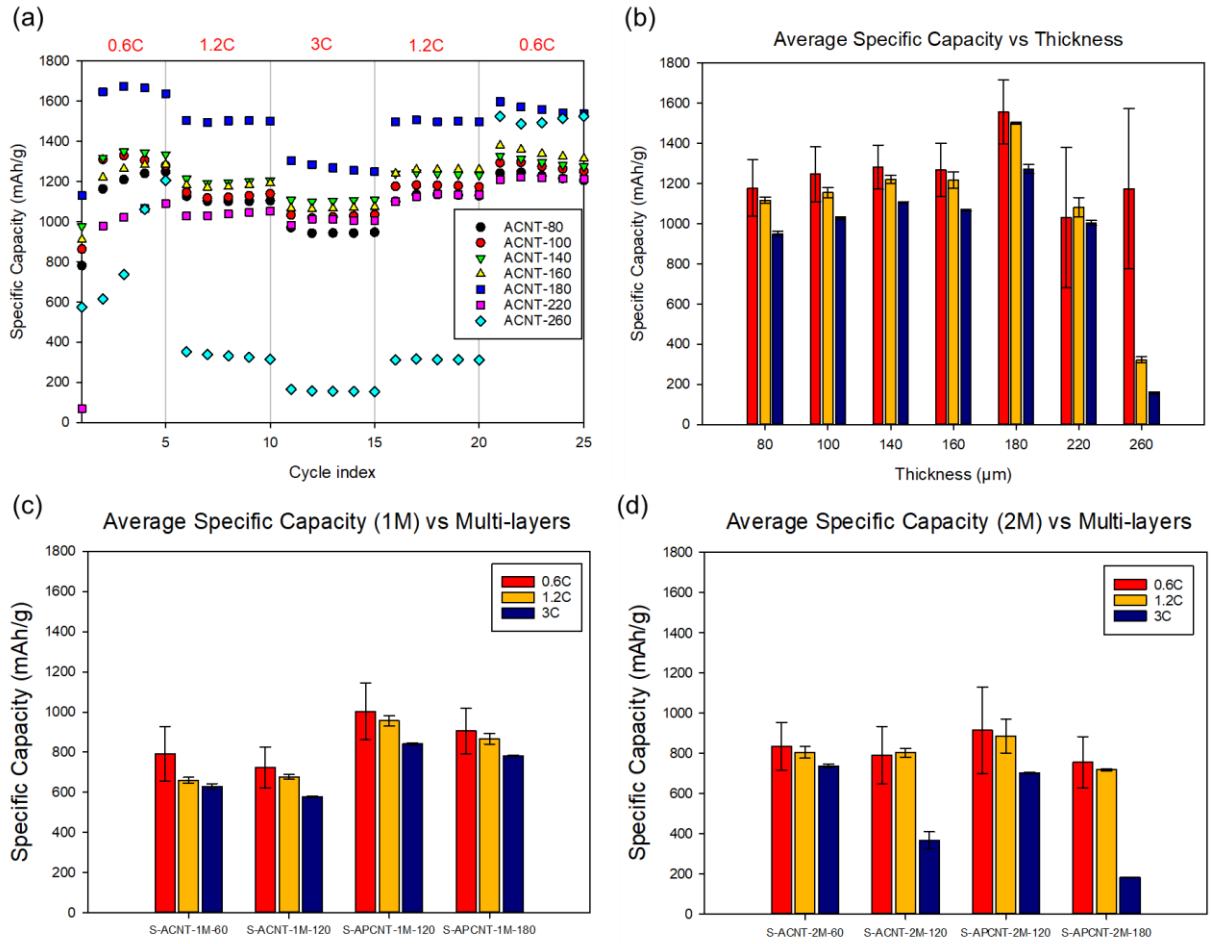

Figure 25. (a) C-rate performance for various thickness of cathode, average specific capacity for (b)various thickness of cathode, multi-layers of slurry CNT cathodes with (b)1M catholyte and (d)2M catholyte

CNT sponge is a promising candidate for Li-S cathode attribute to its outstanding electrical conductivity, and free-standing porous structure. However, it is still challenging to manufacture such material in large scale. CNT cathodes prepared by slurry method is much easier to adapter to current fabrication infrastructure. It would also provide a controllability for special cathode design. Here, we test the ACNT cathode by slurry method (S-ACNT) with various stacks. The thickness of one-layer S-ACNT is about 60μm. The samples are annotated in following order: material-cathode

configuration-catholyte concentration-thickness. For the sample of S-APCNT-1M-120 stands for 120μm thick cathode made by one layers of acid-treat CNT slurry and one interlayer of pristine CNT slurry of which electrolyte is 1M. As shown in Figure 25 (c), cathodes with acid-treated CNT slurry (S-ACNT) show similar thickness-dependent performance as acid-treated freestanding CNT cathodes (ACNT) with 1M catholyte. One layer cathode (S-ACNT-1M-60) and two layers cathode (S-ACNT-1M-120) have comparable C-rate performance with 1M catholyte. When the cathode has three stacks of layers (S-ACNT-1M-180), it shows similar behavior as thicker cathodes of ACNT, which has low specific capacity in the first few cycles, inferior capacity at high C-rate, and recovers to high specific capacity at low C-rate (as shown in Figure 31). Overall, S-ACNT-1M-120 demonstrated improved performance among cathodes with three different thickness. According to aforementioned hypothesis of the interlayer, a pristine CNT slurry is added on the cathode as an interlayer to limit polysulfide diffusion and enhance lithium-ion diffusion. The configuration is demonstrated in Figure 32. S-APCNT-1M-120 shows better performance than S-ACNT-1M-120. To further increase sulfur loading and investigate the effect of electrolyte to sulfur (E/S) ratio, the cathodes are tested with 2M and 3M catholyte, as shown in Figure 25 (d) and Figure 254, respectively. Similarly, S-APCNT-2M-120 with an interlayer deomstrates improved performance for 0.6C and 1.2C. S-ACNT-2M-120 shows significant capacity degradation at 3C, while S-APCNT-2M-120 can still achieve 650 mAh/g at high c-rate. As the concentration of polysulfide further increased to 3M and E/S ration decreased, the ion diffusion become more sluggish, which leads to poor performance at high c-rate. The

cathodes could not cycle at high c-rate but only tested with 0.1C, 0.2C and 0.5C. S-APCNT-3M-120 still shows improved performance, which further demonstrated the effect of interlayer for limiting polysulfide diffusion. However, the capacity performance is already inferior for high c-rate. It shows that molarity limit for high c-rate application should be less than 3M.

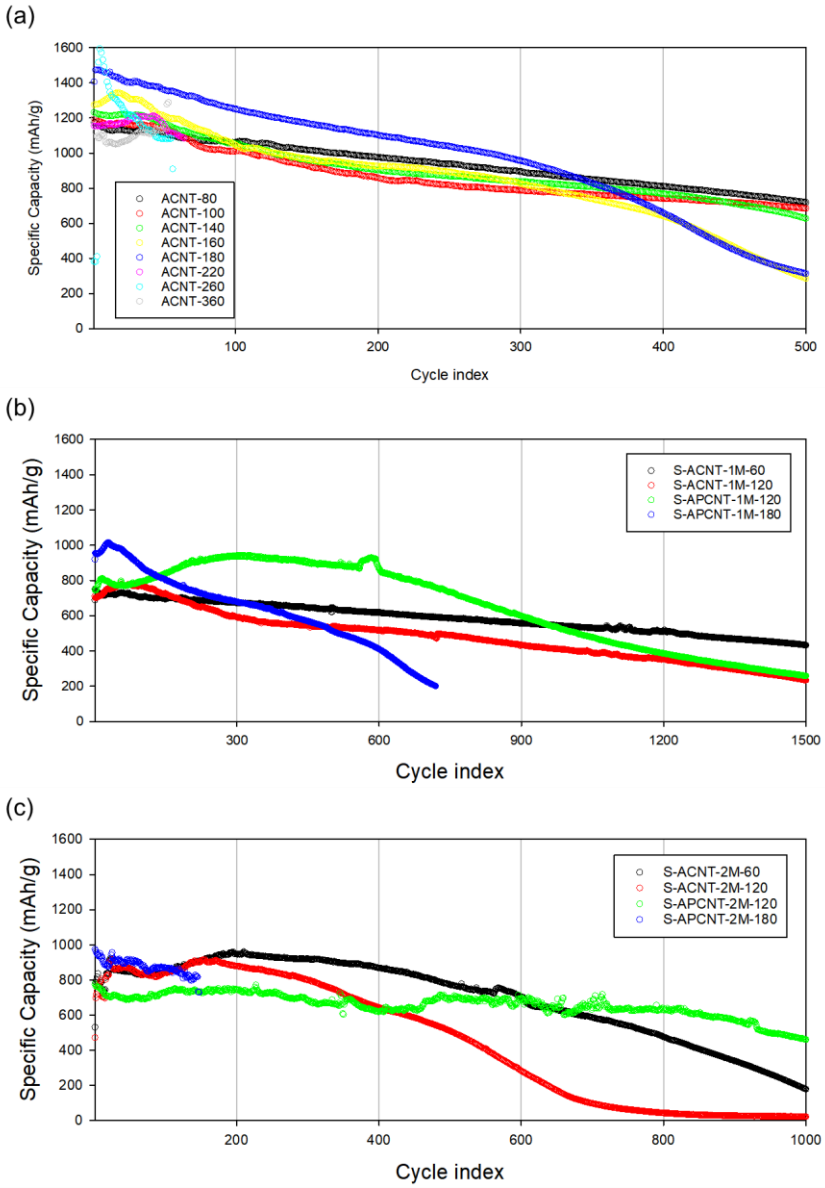

Figure 26 Cycling performance for (a) cathodes with various thickness are tested at 1C, cathodes with (b) 1M catholyte are tested at 1C, and (c) 2M catholyte are tested at 1C.

Other than charging/discharge rate and loading of Li-S battery, improving cycling life is critical for commercial application. Cycling performance of the cathodes with various thickness and molarity are tested at 1C. The result in Figure 26 (a) shows that thinner cathodes have less initial specific capacity but longer cycling life. The thin

cathodes (ACNT-80) begin with a specific capacity around 1150 mAh/g. After cycling for more than 1500 cycles, around 68% of the capacity is still maintained. Cathodes with thickness of 80μm, 100μm and 140μm show similar performance. Lithium-ion diffusion is still sufficient for this rate and loading. However, capacity degradation is severer for the thicker cathodes. ACNT-180 has high initial specific capacity around 1480 mAh/g and slowly decays before 350 cycles. After 350 cycles, both of ACNT-160 and ACNT-180 decays faster than the thinner cathodes. Even though thin cathodes show longer cycling life, thick cathodes are required to accommodate more active material and increase areal loading. Acid-treated CNT slurry is selected to fabricate the cathodes attribute to its outstanding cycling performance. The slurry cathodes are stacked to achieve various thickness and configurations. Although the cathode with two layers of acid-treated CNT (S-ACNT-1M-120) has twice loading as single layer one (S-ACNT-1M-60), the degradation of S-ACNT-1M-120 is server. S-APCNT-1M-120 is the cathode with an interlayer of pristine CNT slurry. It shows significantly improved performance for the first 1000 cycles, which demonstrated that polysulfide diffusion is alleviated benefitting from the interlayer. To further increase areal loading of active material, S-APCNT-1M-180 is fabricated with two acid-treated CNT layers and one interlayer. Even though it achieved more capacity in the beginning, the capacity decays quickly and it ended around 750 cycles. Overall, for the catholyte concentration of 1M, the cathode with thickness of 120μm made by one acid-treated CNT layer and one pristine CNT layer shows most outstanding performance. Since stacking multiple layers of slurry could not effectively improve the loading of active material, applied catholyte

with higher concentration could be another approach. According to the c-rate performance result in this work, cathodes could still achieve outstanding performance with 2M catholyte, but shows inferior capacity with 3M catholyte. Here, cathodes are tested with 2M catholyte at 1C (Figure 26 (c)), and with 3M catholyte at 0.16C (Figure 33), respectively. S-ACNT-2M-60 and S-ACNT-2M-120 shows similar capacity before 150 cycles, while the thicker one decays much faster. Lithium-ion diffusion is sluggish in the high concentration catholyte, which results more "dead sulfur" for the thick cathode case. Interlayer in S-APCNT-2M-120 alleviated polysulfide diffusion and enhanced lithium-ion diffusion. Thus, the initial capacity is around 750 mAh/g and capacity can maintain at 500 mAh/g after 1000 cycles. However, S-APCNT-2M-180 ends around 150 cycles due to thick cathode and accumulated "dead sulfur". The concentration is further increased to 3M, which the cells cycle at 0.16C. S-ACNT-3M-60 reveals poor capacity and short cycle life since the thin cathode cannot work as effective polysulfide reservoir and higher polysulfide concentration gradient, which leads to severe shutting effect. The thickest cathode (S-APCNT-3M-180) also ends very fast after 100 cycles. The reason for the shorter cycling life is caused by more sluggish ionic diffusion and more dead sulfur in the cathodes than the 2M sample. However, the cathodes with thickness of 120μm shows improved specific capacity and cycling life, especially the one with interlayer (S-APCNT-3M-120).

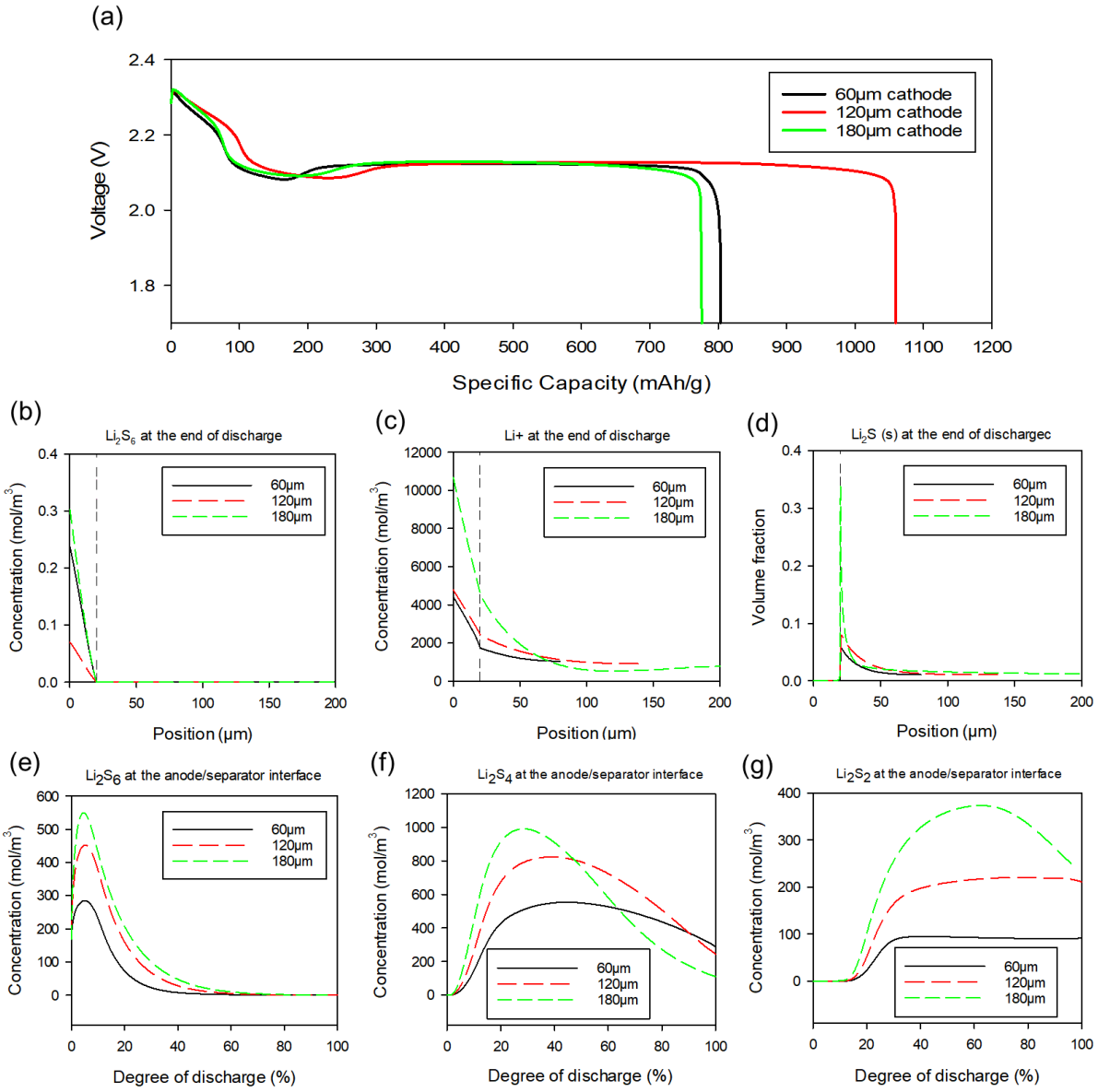

Figure 27 COMSOL simulation result for thickness-dependent performance: (a) voltage profile, (b) concentration of Li_2S_6 at the end of discharge, (c) concentration of Li+ at the end of discharge, (d) volume fraction of Li_2S solid at the end of discharge, concentration of (e) Li_2S_6, (f) Li_2S_4, and (g) Li_2S_2 at the anode/separator interface. The dash line shows the location of the interface between separator and cathode.

The thickness-dependent performance is supported by COMSOL simulation of Li-S battery. The voltage profile of cathodes with various thickness is shown in Figure 27(a). Conditions of the cell are analyzed at the beginning of discharge, end of first plateau, and end of discharge. The case with moderate thickness shows highest specific capacity, while thinner case has shorter first plateau and moderate total capacity and thicker case has moderate first plateau but inferior total capacity. The inferior capacity of thin cathode could attribute to the polysulfide diffusion, which can be verified by investigating the concentration across the separator. In the beginning, the concentrations of Li_2S_6 are the same for all the samples. In the end of first plateau, thick cathode has largest concentration gradient across the separator as shown in Figure 34(a), which indicates more high order polysulfide is easy to diffuse through the separator during first plateau. Thus, the thin and thick cathode has less capacity than moderate one for the first plateau. At the end of discharge, as shown in Figure 27(b), thin and thick cathode has large Li_2S_6 concentration at the anode/separator interface, which means polysulfide is diffused to the anode side and cannot participate in the reaction. However, moderate cathode has least Li_2S_6 concentration at the anode/separator interface, which indicates better sulfur utilization. It worth noting that lithium-ion concentration of the thick cathode is always higher, which is displayed in Figure 27(c). Thicker cathode can accommodate more active material, while it also requires more lithium-ion diffusion due to the higher consumption of lithium-ion. Thus, sluggish lithium-ion diffusion could lead to “dead sulfur” and affect the performance of thick cathode. In the end of discharge, the thick cathode has much higher concentration gradient of Li+ and lower concentration of

Li+ on the current collector side. This proved aforementioned theory that incomplete reaction on the current collector side is due to sluggish diffusion of lithium ion. Figure 34(b) shows large concentration gradient of Li_2S_4 across the thick cathode and separator at point b, which indicates that Li_2S_4 diffusion is more critical for the thick cathode. However, at end of discharge, thin cathode has higher concentration gradient of Li_2S_4 across separator (Figure 34(c). The concentration of Li_2S_2 is significantly higher around the separator at point b, which indicates the preferrable location for the product of Li_2S_2, as shown in Figure 34(c,d). This could attribute to the sufficient lithium-ion diffusion from anode side, which promotes the generation of Li_2S_2. The volume fraction of Li_2S solid, shown in Figure 27(d), is much higher around the separator. This result supports the *in-operando* observation that Li_2S solid is preferably deposit in the region around separator. The volume fraction of Li_2S could reach 35% around the separator for the thickest cathode, which means that the deposition of end product could block the diffusion path of other species, especially for the thicker cathode. The initial porosity was set to 80%, which means the porosity in this region is 76%, 64%, and 45% for cathode with thin, moderate and thick thickness, respectively. The accumulated deposition of Li_2S could cause clogging for lithium-ion diffusion pathway and loss of active material due to the insulating property. Clogging the pores in this region further exacerbate the diffusion barrier for the thick cathode, which could cause severe concentration polarization. In order to alleviate Li_2S accumulate in this region, Li_2S-repelling material would be a good candidate here. Pristine CNT (PCNT) has no-polar structure, which could be repelling to Li_2S nucleation. Thus, we applied PCNT on the

region closer to the separator as a buffer layer to alleviate Li_2S accumulation and stack ACNT on the region closer to the current collector as polysulfide reservoir. In order to achieve proper loading for outstanding cycling and c-rate performance, thickness need to be carefully designed to avoid large overpotential, clogging issue caused by deposition of Li_2S. To analyze the capacity difference depended on thickness, concentration of Li_2S_6, Li_2S_4, and Li_2S_2 at the anode/separator interface is investigated to unveil shuttling effect, which are shown in Figure 27(e-g). Thick cathode shows largest concentration fluctuation over degree of discharge, which indicates that it is more likely polysulfides are diffuse through this interface and cause loss of active material. At the end of discharge, thin cathode has higher concentration of Li_2S_4. The un-reacted polysulfide could result in less capacity for this cathode.

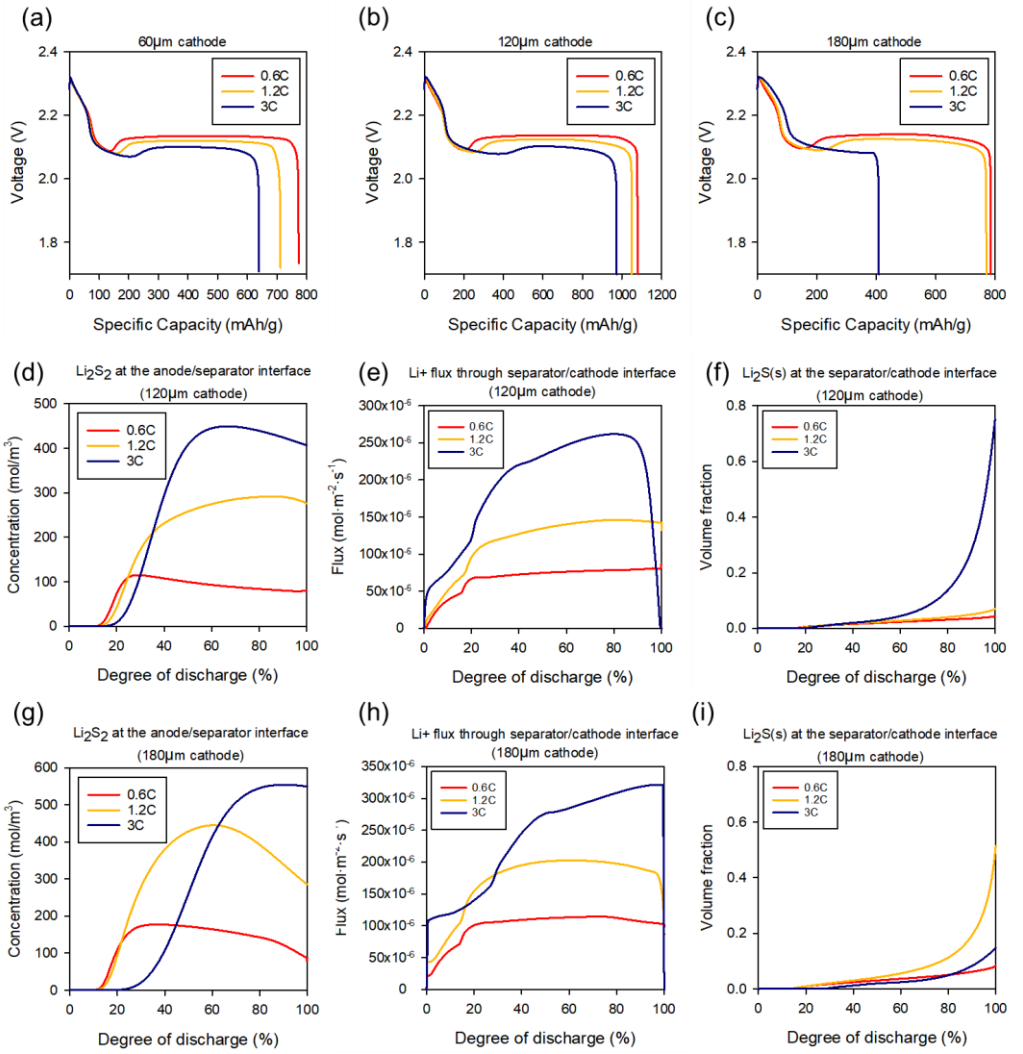

Figure 28 Simulation result of voltage profile for cathode thickness of (a) 60µm, (b)120µm, and (c)180µm, (d)Concentration of Li_2S_2 at the anode/separator interface for 120µm cathode, (e) Li+ flux diffuse through separator/cathode interface for 120µm cathode, (f) Li_2S (s) deposited at the anode/separator interface for 120µm cathode, (g)Concentration of Li_2S_2 at the anode/separator interface for 180µm cathode, (h) Li+ flux diffuse through separator/cathode interface for 180µm cathode, (i) Li_2S (s) deposited at the anode/separator interface for 180µm cathode,

To investigate the factors that limited the capacity of thick cathode at high c-rate, COMSOL simulation is conducted to reveal the mechanism. Cathodes with thickness of 60µm, 120µm, and 180µm are modeled in the COMSOL to run at 0.6C, 1.2C, and 3C.

The 60μm and 120μm cathodes show similar voltage profiles and degradation of capacity when c-rate is higher as shown in Figure 28 (a,b). 180μm cathode has poor performance at 3C, which agrees to the experimental results. Capacity contributed more from the first plateau is larger while less from the second plateau when c-rate increased. This is observed in both simulation and experimental result (Figure 35(a)). Lithium-ion concentration gradient of 180μm cathode (Figure 35(b)) is much larger than 180μm cathode (Figure 35(c)). This is attribute to the larger loading of active material for the thick cathode and higher consumption of lithium-ion during discharging. Figure 35(d)shows that clogging issue caused by the Li_2S deposition could block the diffusion pathway of lithium-ion. Deposition of Li_2S completely occupied the pore in the region around the separator, which further exacerbate the polarization. It is worth noting that Li_2S deposition profile is sharper and more accumulated at higher c-rate. The time-dependent evolution of Li_2S_2 concentration at the anode/separator interface is further investigated to find out why cathode has poor performance at high c-rate, especially for the thick electrode. In Figure 28 (d) larger concentration of Li_2S_2 at the anode/separator interface indicates that more polysulfides are diffused to the anode side for high c-rate application. Similarly, Figure 28 (e) shows concentration of Li_2S_2 at the anode/separator interface for 180μm cathode. The sudden shut down of the 3C cell (as indicated in Figure 28 (c)) could attribute to the stopped conversion of Li_2S_2. However, how the reaction stopped in still unknown. Since high c-rate and thick electrode could require large lithium-ion consumption and diffusion, it is critical to analyze how lithium-ion diffuse through the separator/cathode interface and clogging issue caused by Li_2S solid.

Lithium-ion flux through the separator/cathode interface and deposition process of Li_2S solid at the separator/cathode interface are revealed, as shown in Figure 28 (e-i). Higher flux of lithium-ion is required for the high c-rate cases as the discharge proceed. Gradually growing of Li_2S solid deposition could block the diffusion path of lithium-ion. Li_2S deposition increases rapidly after 80% of DoD (degree of discharge) for the 120μm cathode. At the same time, clogging issue drastically limited lithium-ion flux through separator/cathode interface and prevented the reaction further proceeding. For the 180μm cathode, it requires more lithium-ion flux due to higher loading. Even though at the end of discharge, the volume fraction of Li_2S is only 18%, it cannot satisfy the large required lithium-ion flux (3.2×10^{-4} $mol\cdot m^{-2}\cdot s^{-1}$).

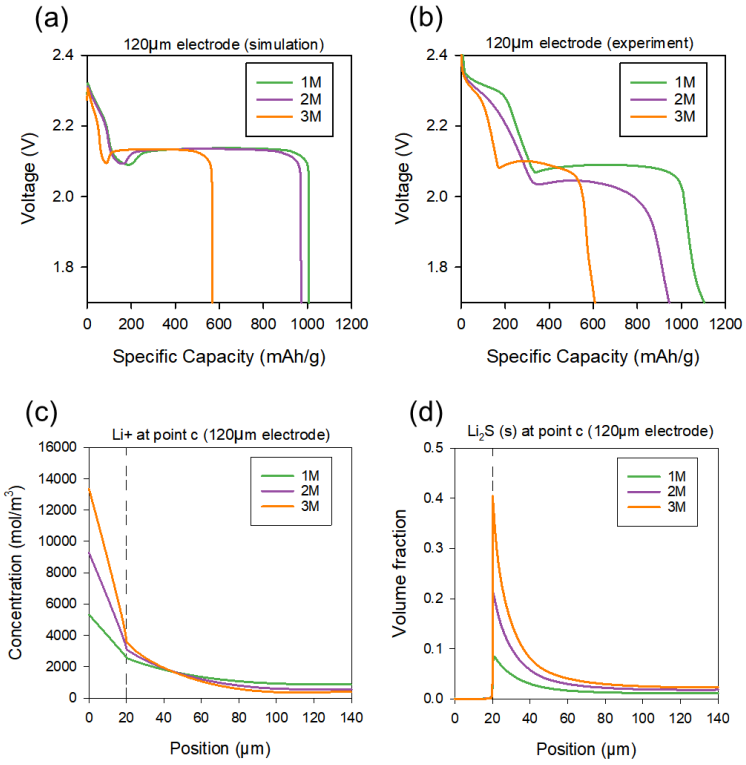

Figure 29 (a) simulation and (b) experimental results of 120µm cathode with various molarity of catholyte tested at 1C, (c) lithium-ion concentration and (d)volume fraction of Li_2S solid at the end of discharge.

Since further increasing cathode thickness to accommodate more active material shows limitation, applying more concentrated catholyte could be another approach for higher loading. However, the experiments shows that more concentrated catholyte is not suitable for high c-rate application. 120µm cathode are tested at 1C with catholyte of 1M, 2M, and 3M. Simulation (Figure 29a) and experimental (Figure 29b) show similar voltage profile of which capacity of higher concentration cases has less capacity and shorter first plateau. It indicates that polysulfide utilization is not effective in sluggish condition due to poor lithium-ion diffusion. The lithium-ion concentration profile at the end of discharge shows large gradient and extremely low concentration value, as shown

in Figure 29 (c). 3M case in Figure 29 (d) has more Li_2S deposition around the separator, however it is not as severe as the high c-rate case. The porosity in this region still has 40%, 60% and 70% for the 3M, 2M, and 1M cases, respectively.

5.4. Conclusion

Considering cathode thickness, discharging/charging rate and loading of active material, capacity of Li-S battery is mainly limited by clogging issue of Li_2S solid, lithium-ion diffusion and polarization. However, the influencing factors for each conditions varies. Thickness study of lithium sulfur battery is critical to improve the performance and realize practical application. In order to accommodate more active material and achieve higher energy density, thicker cathode is preferred for this scenario. Thinner cathode shows advantages of better c-rate performance and longer cycle life. Rate capability is mainly limited by the clogging issue of Li_2S deposition as demonstrated by COMSOL simulation results. It is essential to solve the clogging issue on the cathode surface for high c-rate Li-S battery. Applying non-polar buffering layer in this region could alleviate the accumulation of the solid, thus ensure lithium-ion diffusion path. Utilization of more concentrated catholyte and higher loading of active material could be mainly affected by the lithium-ion polarization. Introducing vertical tunnel for effective diffusion path could primarily enhance the polysulfide utilization inside the cathode if facing high catholyte concentration issue. Here, we conduct thickness-dependent study, c-rate performance test, and molarity investigation to reveal optimization procedure of Li-S cathodes. The inside details could promote more ideas to improve the performance of Li-S from different aspect.

5.5. Experimental Section

Preparation of CNT sponge and slurry electrodes:

To fabricate a three-dimensional CNT layer, cylindrical CNT sponges were synthesized by a CVD process. The detailed CVD procedure is summarized in our previous study. [85] By using the razor blade, the CNT sponge was sliced into thin layers (100 ~ 200 μm). The sliced layers were gathered into a hardened steel container (SPEX SamplePrep 8001) with two chromed steel balls (5 mm diameter, Swordfish), and through the high-energy ball milling procedure (SPEX SamplePrep 8000M Mixer Mill), the layers were chopped into CNT chunks with a diameter of few hundreds of microns. The fabricated CNT chunks were mixed with Polyvinylidene Fluoride (PVDF, Mw ~534,000, Sigma Aldrich) at a weight ratio of 95:5 in N-methyl-2-pyrrolidinone (NMP, > 99%, Sigma Aldrich) solvent. Then the mixture was stirred manually in a glass mortar for 5 minutes to form a steady slurry since using the magnetic stirring or sonicating bath gives rise to the damage on the CNT chunk structure. The fabricated slurry was coated on Cu foil with an initial thickness of around a few hundred microns with blade casting method, then the slurry-coated foil was transferred to a vacuum oven for drying under 60 ℃ for 12 hours. The fully dried slurry layer on the Cu substrate was cut into circular shapes with a diameter of 9.5 mm (3/8 inch), and each CNT slurry layer was detached by adding a drop of Sulfuric Acid (BDH Chemicals, 95-98%) to the slurry layer. After dropping the acid agent, the slurry on the Cu foil is floated in deionized water to separate the free-standing CNT slurry layer from the Cu foil. Finally, by rinsing the free-standing CNT slurry layer

with Ethyl Alcohol (Anhydrous, ≥ 99.5 %, Sigma Aldrich) and drying under 60 ℃ for additional 3 hours, the free-standing 3D-CNT layer was obtained.

For the mechano-chemically acid-treated CNT layer, a vacuum filtration set up with a solution composed of $KMnO_4$ (AMRESCO, >99%) and sulfuric acid (BDH Chemicals, 95-98%) was applied to conduct a mechanochemical treatment method to generate trench-wall CNT with functional groups on the surface of the aforementioned sliced thin CNT layers (details can be found in our previous paper [5]). After rinsing the layers with deionized water and drying at 60 ℃ for 12 hours, the acid-treated CNT layers were obtained. The subsequent ball milling, slurry preparation, and free-standing layer detachment process are the same as the previous 3D CNT layer preparation. Through this, unique CNT free-standing layers with partially unzipped additional functional groups attached surface are obtained.

Test conditions are summarized in Table 1.

Table 1 Test condition of samples.

Sample	Electrode thickness	Catholyte concentration (mol/L)	Catholyte volume (μL)	Sulfur Loading (mg/cm2)
1	60	1	10	0.46
2	120	1	20	0.91
3	180	1	30	1.37
4	60	2	10	0.91
5	120	2	20	1.83
6	180	2	30	2.74
7	60	3	10	1.37
8	120	3	20	2.74
9	180	3	30	4.11

In-operando pouch cell assembly and testing: In-operando cells were fabricated using pouch cell films with a cover glass (thickness No.1) as a viewing window (see Fig. S4). Copper foils wrapping around typical microscope glass slides (thickness: ~1 mm) were used as current collectors on top of another glass slide. CNT and lithium metal (Alfa Aesar, 99.9%) were placed in the middle with a Celgard 2400 separator in between, and then the two glass slides with the current collectors were pushed against each other. The amount of the electrolyte (1 M LiTFSI (Sigma-Aldrich, 99%) and 0.5 M $LiNO_3$ (Alfa Aesar, 99%) in a mixture of 1,3-dioxolane (Alfa Aesar, 99.5%) and 1,2-dimethoxyethane (Alfa Aesar, 99+%) (1:1 by vol.)) was 500 μL to fill in the pouch cell. All the lithium insertion processes were carried out with a constant current density of 1 mA/cm^2 without formation cycles. Dark-field optical microscope (Olympus BX5) images were taken every 1 minute using Q capture Pro program and made a video by an image merging program (Openshot Video editor).

Simulation Section

The battery performance will be simulated in COMSOL with meso-scale results. Representative reactions of a lithium sulfur battery are listed below: Eq (1) to Eq (2).

$$\boldsymbol{Li \leftrightarrow Li^{+} + e^{-}} \quad \textbf{Eq (5)}$$

$$\boldsymbol{\frac{1}{2}S_8^0 + e^{-} \leftrightarrow \frac{1}{2}S_8^{2-}} \quad \textbf{Eq (6)}$$

$$\boldsymbol{\frac{3}{2}S_8^{2-} + e^{-} \leftrightarrow 2S_6^{2-}} \quad \textbf{Eq (3)}$$

$$\boldsymbol{S_6^{2-} + e^{-} \leftrightarrow \frac{3}{2}S_4^{2-}} \quad \textbf{Eq (4)}$$

$$\boldsymbol{\frac{1}{2}S_4^{2-} + e^{-} \leftrightarrow S_2^{2-}} \quad \textbf{Eq (5)}$$

$$\boldsymbol{\frac{1}{2}S_2^{2-} + e^{-} \leftrightarrow S^{2-}} \quad \textbf{Eq (6)}$$

For a multicomponent electrolyte system in a porous medium, the material balance on an individual species is given by:

$$\frac{\partial \varepsilon C_i}{\partial t} = - \nabla \cdot N_i + r_i - R_i$$

where ε is the pore volume of the electrode, C_i is the concentration of the species i, $- \nabla \cdot N_i$ represents the flux of species into the system, r_i indicates the productions or consumption of the species by electrochemical reactions, and R_i is the precipitation rate of the species.

For the flux term N_i, diffusion and migration are both considered:

$$\frac{N_i}{\varepsilon} = - D_i \nabla C_i - z_i \frac{D_i}{RT} F C_i \nabla \varphi_2$$

where z_i is the charge number and φ_2 is the liquid phase potential.

The reaction rate of species i, r_i, is determined by the current density of related electrochemical reactions j :

$$r_i = - a \sum_j \frac{s_{i,j} \, i_j}{n_j F}$$

where $s_{i,j}$ is the stoichiometric coefficient for species i in reaction j, i_j is the current density, n_j is the number of electrons transferred, a is the surface area of the porous electrode, which described in this relation:

$$a = a_0 \left(\frac{\varepsilon}{\varepsilon_0}\right)^{\xi}$$

in which, a_0 is the initial surface area, ε_0 is the initial porosity, and ξ is the empirical parameter describing the morphology of the precipitate, which is set to 1.5 in this work. The current density of related electrochemical reaction j, i_j, is determined by Bulter-Volmer equation:

$$i_j = i_{0,\,jref} \left\{ \prod_i \left(\frac{C_i}{Ci,ref}\right)^{p_{i,j}} \exp\left(\frac{\alpha_{aj}F}{RT}\eta_j\right) - \prod_i \left(\frac{C_i}{Ci,ref}\right)^{q_{i,j}} \exp\left(\frac{\alpha_{cj}F}{RT}\eta_j\right) \right\}$$

where the overpotential for reaction j is given by:

$$\eta_j = \varphi_1 - \varphi_2 - U_{j,ref}$$

in which φ_1 is the potential in solid phase, φ_2 is the potential in liquid phase, and $U_{j,ref}$ is the open circuit potential for reaction j at the reference concentration $C_{j,ref}$.

$$U_{j,ref} = U_j^{\theta} - \frac{RT}{n_j F} \sum_i s_{i,j} ln\left[\frac{C_{j,ref}}{1000}\right]$$

Current density (i_j) depends upon the difference between the potential of the electrode (φ_1) and the potential in the solution adjacent to the electrode surface (φ_2) relative to the open-circuit potential for reaction ($U_{j,ref}$) evaluated at the surface concentrations of species ($C_{j,ref}$).

The liquid phase current density, i_e, is related to the flux of the species:

$$i_e = F \sum_i z_i \, N_i$$

Additionally, the charge can only be enter or leave the liquid phase by electrochemical reactions at the solid/liquid interface:

$$\nabla \cdot i_e = a \sum_j i_j$$

The solid phase charge-transfer is purely by electronic conduction, which is defined by Ohm's law:

$$i_s = -\sigma \nabla \varphi_1$$

Considering charge is conserved in the cathode, the charge leaving one phase must be qual to the one entering the other phase:

$$\nabla \cdot i_e + \nabla \cdot i_s = 0$$

Finally, the rate of production of consumption of species i due to precipitation and dissolution, R_i, is defined:

$$R_i = \sum_k \gamma_{i,k} \, R'_k$$

where R'_k is the rate of precipitation of the solid species k, $\gamma_{i,k}$ is the number of moles of ionic species i in the solid species k.

$$R'_k = k_k \varepsilon_k \left(\prod_i C_i^{\gamma_{i,k}} - K_{sp,k} \right)$$

where $K_{sp,k}$ is the solubility product of k in the electrolyte and k_k is the rate constant.

As the precipitate occupies the pore volume of the electrode, the porosity change can be defined as:

$$\frac{\partial \varepsilon}{\partial t} = -\sum_k \tilde{V}_k \, R_k'$$

where $\tilde{V}_k$ is the partial molar volume.

Boundary condition:

At the cathode/current collector interface ($x = L$), the flux of all the species are zero.

$$N_i = 0 \; at \; x = L$$

At the cathode/current collector interface ($x = L$), all the current density is carried by the solid phase, which is equal to the external current density applied to the system. This means that the solution phase current density at this boundary is zero.

$$-\sigma \nabla \varphi_1 = I_{app} \; at \; x = L$$

$$i_e = 0 \; at \; x = L$$

At the separator/cathode interface ($x = L_s$), the flux of each species is continuous

$$N_{i,separator} = N_{i,cathode} \; at \; x = L_s$$

At the separator/cathode interface ($x = L_s$), all the current is carried by solution phase alone, which is also continuous.

$$i_{e,separator} = i_{e,cathode} \; at \; x = L_s$$

$$-\sigma \nabla \varphi_1 = 0 \; at \; x = L_s$$

At the anode/separator interface, we assume there is no polysulfide shuttle effect, which means that there is only Li^+ transported over the separator.

$$N_i = 0 \; at \; x = 0$$

For Li^+, the flux boundary condition of the concentration of Li+ written as:

$$N_1 = \frac{i_1}{F} \; at \; x = 0$$

i_1 is given by Butler-Volmer equation for the anode reaction.

The potential of anode is set to 0.

$$\varphi_1 = 0 \; at \; x = 0$$

Because the only species with nonzero flux at this boundary is Li^+, the liquid-phase current density at $x = 0$ is given by

$$i_e = FN_1 \; at \; x = 0$$

The parameters are listed in **Error! Reference source not found.** to Table 8.

Transport properties of the species are described by diffusion coefficients. The transport properties could affect the polarization of each species across the electrode, especially for high c-rate application.

Table 2 Transport properties.[181]

D_Li_1p	0.88e-12[m^2/s]	Diffusion coefficient, Li+
D_S8	0.88e-11[m^2/s]	Diffusion coefficient, S_8
D_S8_2m	3.5e-12[m^2/s]	Diffusion coefficient, S_8^{-2}
D_S6_2m	3.5e-12[m^2/s]	Diffusion coefficient, S_6^{-2}
D_S4_2m	1.75e-12[m^2/s]	Diffusion coefficient, S_4^{-2}
D_S2_2m	0.88e-12[m^2/s]	Diffusion coefficient, S_2^{-2}
D_S_2m	0.88e-12[m^2/s]	Diffusion coefficient, S^{-2}
D_A_1m	3.5e-12[m^2/s]	Diffusion coefficient, salt anion

The reference concentration could affect the equilibrium potential and current of each reaction. Parameters are modified from the values employed by Kumaresan et al[182], since the experiments are started with Li_2S_6 catholyte.

Table 3 Initial and reference concentration.

c_Li_1p_ref	1500[mol/m^3]	Reference concentration, Li+
c_S8_ref	0.019[mol/m^3]	Reference concentration, S_8
c_S8_2m_ref	0.18[mol/m^3]	Reference concentration, S_8^{-2}
c_S6_2m_ref	0.32[mol/m^3]	Reference concentration, S_6^{-2}
c_S4_2m_ref	0.02[mol/m^3]	Reference concentration, S_4^{-2}
c_S2_2m_ref	5.23e-7[mol/m^3]	Reference concentration, S_2^{-2}
c_S_2m_ref	8.27e-10[mol/m^3]	Reference concentration, S^{-2}
c_A_1m_ref	1000[mol/m^3]	Reference concentration, salt anion

Thickness of separator (L_sep) is set to 20μm. Thickness of electrode varies from 60μm to 180μm for thickness-dependent study.

Table 4 Electrode and separator parameters.

L_sep	20e-6[m]	Separator thickness
L_pos	60 120 180e-6[m]	Electrode thickness
A_cell	0.7e-4[m^2]	Cell area

Initial porosity of separator (epsl_sep_0) is 50%. Initial porosity of electrode (epsl_pos_0) is 80%. Initial volume fractions of S_8(s) and Li_2S(s) are set to a non-zero value.

Table 5 Initial porosity and volume fraction of solid in the separator and electrode.

epsl_sep_0	0.5	Electrolyte volume fraction of separator without deposits
epsl_pos_0	0.8	Electrolyte volume fraction of positive electrode without deposits
eps_S8_s_sep_0	1.00E-12	Initial volume fraction in separator of S_8(s)
eps_S8_s_pos_0	1.00E-12	Initial volume fraction in electrode of S_8(s)
eps_Li2S_s_sep_0	1.00E-07	Initial volume fraction in separator of Li_2S(s)
eps_Li2S_s_pos_0	1.00E-07	Initial volume fraction in electrode of Li2S(s)

Precipitation and dissolution parameters of S_8(s) and Li_2S(s) reflect how fast the solid nucleates and dissolve.

Table 6 Precipitation and dissolution parameters.[182]

k_S8_s	5[1/s]	Rate constant, S_8(s) deposition-dissolution
Ksp_S8_s	19[mol/m^3]	Solubility product
k_Li2S_s	3.45e-5[m^6*mol^-2/s]	Rate constant, Li_2S(s) deposition-dissolution
Ksp_Li2S_s	1e2[mol^3*m^-9]	Solubility product

Table 7 Kinetics and thermodynamics properties.[182]

Eeq_Li_ref	0[V]-R_const*T/F_const*log((c_Li_1p_ref/1[M])^(-1))	Equilibrium potential at reference concentrations, Li/Li+ reaction
Eeq_1_ref	2.41[V]-R_const*T/F_const*log((c_S8_ref /1[M])^(-1/2) *(c_S8_2m_ref/1[M])^(1/2))	Equilibrium potential at reference concentrations, reaction 1
Eeq_2_ref	2.35[V]-R_const*T/F_const*log((c_S8_2m_ref/1[M])^(-3/2)*(c_S6_2m_ref/1[M])^2)	Equilibrium potential at reference concentrations, reaction 2

Table 7 Continued

Eeq_3_ref	2.23[V]-R_const*T/F_const*log((c_S6_2m_ref/1[M])^(-1) *(c_S4_2m_ref/1[M])^(3/2))	Equilibrium potential at reference concentrations, reaction 3
Eeq_4_ref	2.03[V]-R_const*T/F_const*log((c_S4_2m_ref/1[M])^(-1/2) *(c_S2_2m_ref/1[M])^(1))	Equilibrium potential at reference concentrations, reaction 4
Eeq_5_ref	2.01[V]-R_const*T/F_const*log((c_S2_2m_ref/1[M])^(-1/2) *(c_S_2m_ref /1[M])^(1))	Equilibrium potential at reference concentrations, reaction 5
i0_Li_ref	0.5[A/m^2]	Exchange current density at reference concentrations, Li/Li+ reaction
i0_1_ref	1.9[A/m^2]	Exchange current density at reference concentrations, reaction 1

Table 7 Continued

i0_2_ref	0.02[A/m^2]	Exchange current density at reference concentrations, reaction 2
i0_3_ref	0.02[A/m^2]	Exchange current density at reference concentrations, reaction 3
i0_4_ref	2e-4[A/m^2]	Exchange current density at reference concentrations, reaction 4
i0_5_ref	2e-9[A/m^2]*0+2e-7[A/m^2]	Exchange current density at reference concentrations, reaction 5

C-rate values are set to 0.6C, 1.2C, and 3C for rate performance simulation. Initial concentrations of Li_2S_6 (c_S6_2m_pos_0) are set to (1/6), (2/6), and (3/6)[mol/L] based on the molarity of Li_2S_6 solute. Molarity based on S are 1M, 2M, and 3M, respectively.

Volume of Li_2S_6 catholyte is 10μL per 60μm thick electrode, of which the area is $0.7cm^2$ for each electrode.

Table 8 Test conditions for the samples.

C	0.6C 1.2C 3C	C-rate
c_S6_2m_pos_0	(1/6) (2/6) (3/6)[mol/L]	Initial concentration of Li_2S_6
V_S6_2m_pos_0	10e-6 20e-6 30e-6 [L]	Volume of catholyte
L_pos	60 120 180e-6[m]	Electrode thickness

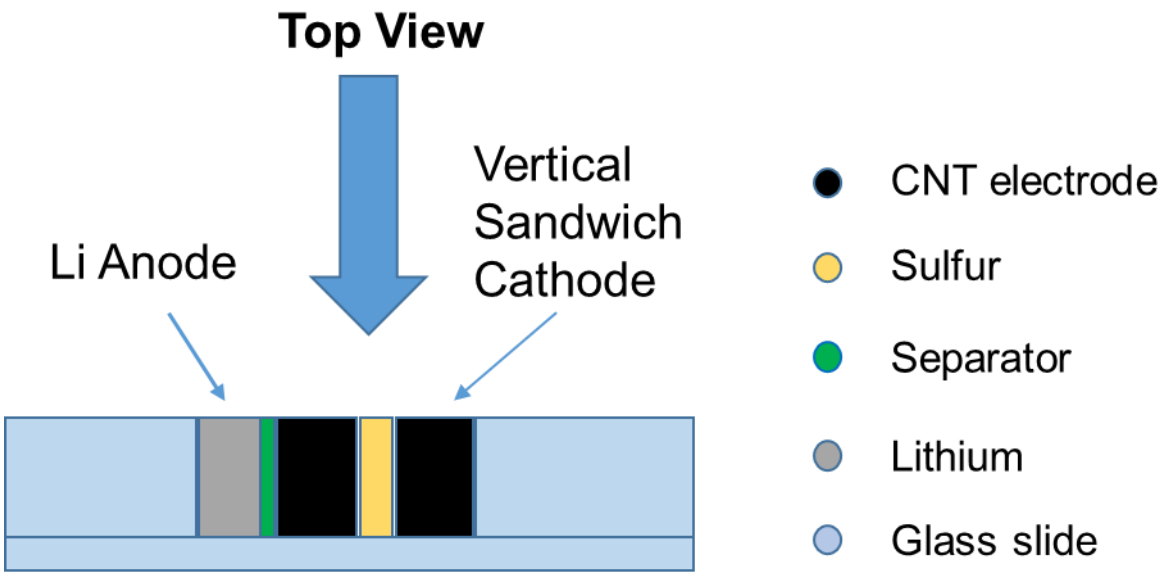

Figure 30 Illustration of in-operando setup.

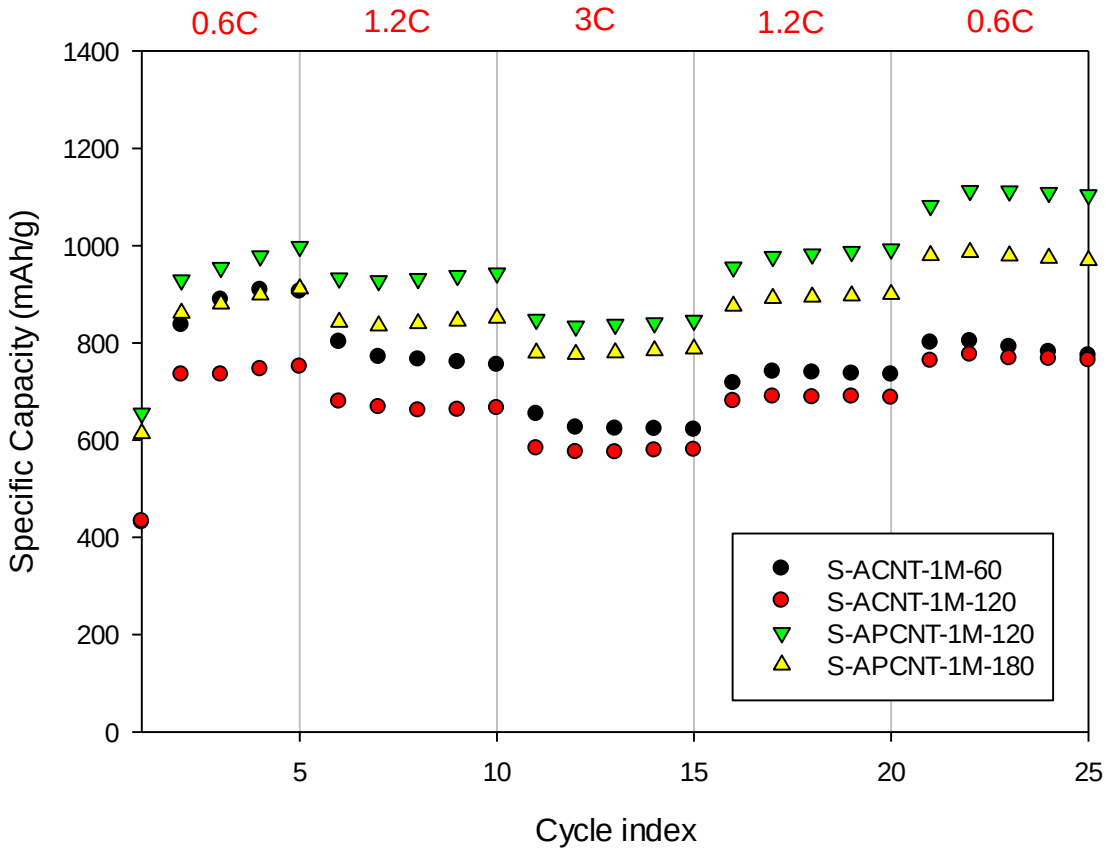

Figure 31 C-rate performance of slurry electrodes with various thickness: one layer (S-ACNT-60), two layers (S-ACNT-120), three layers (S-ACNT-180), and one layer of PCNT and one layer of ACNT (S-APCNT-120).

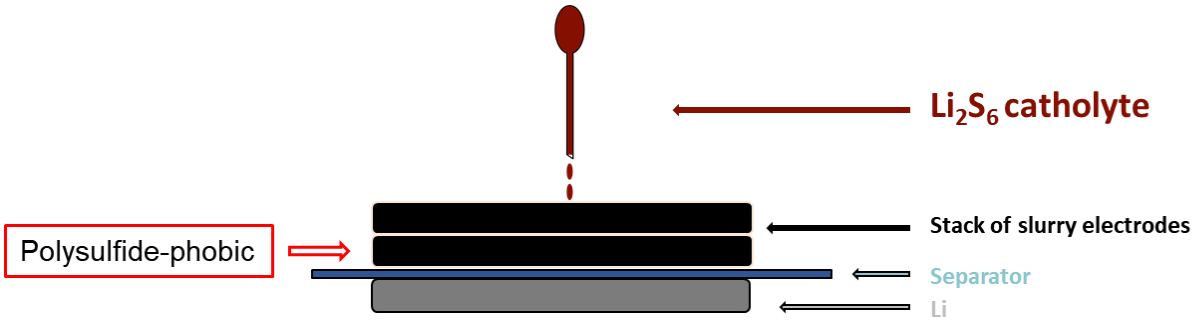

Figure 32 Illustration of slurry electrode configuration.

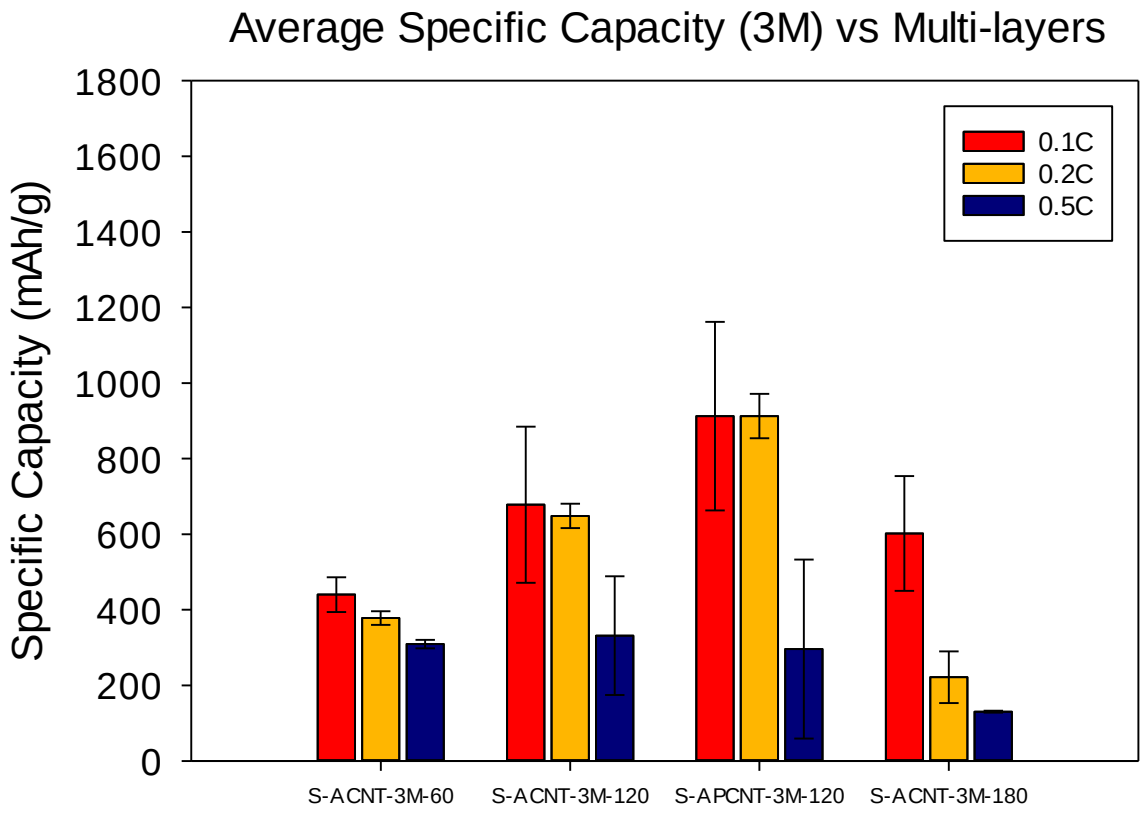

Figure 33 Average specific capacity for multi-layers of slurry CNT electrodes with 3M catholyte

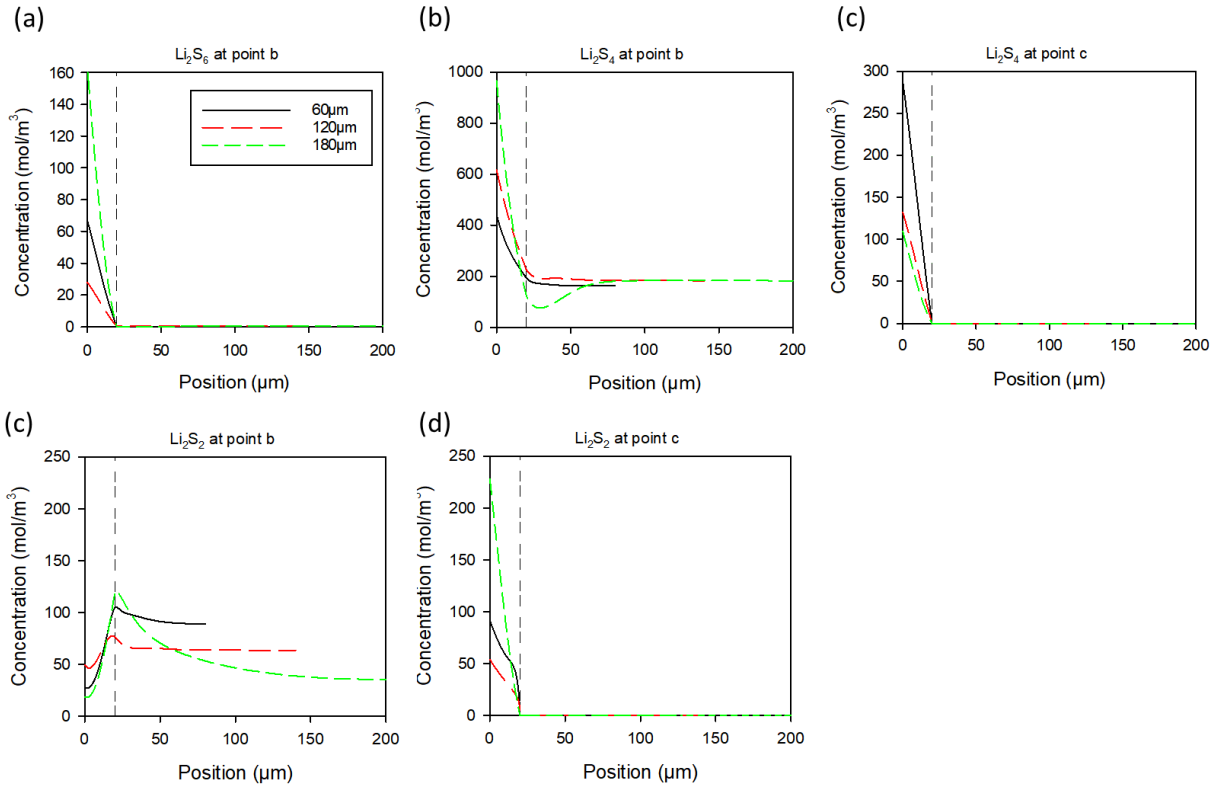

Figure 34 COMSOL simulation result for thickness-dependent performance: (a) concentration of Li_2S_6 at point b, (b) concentration of Li_2S_4 at point c, (c) concentration of Li_2S_2 at point b, and (d) concentration of Li_2S_2 at point c.

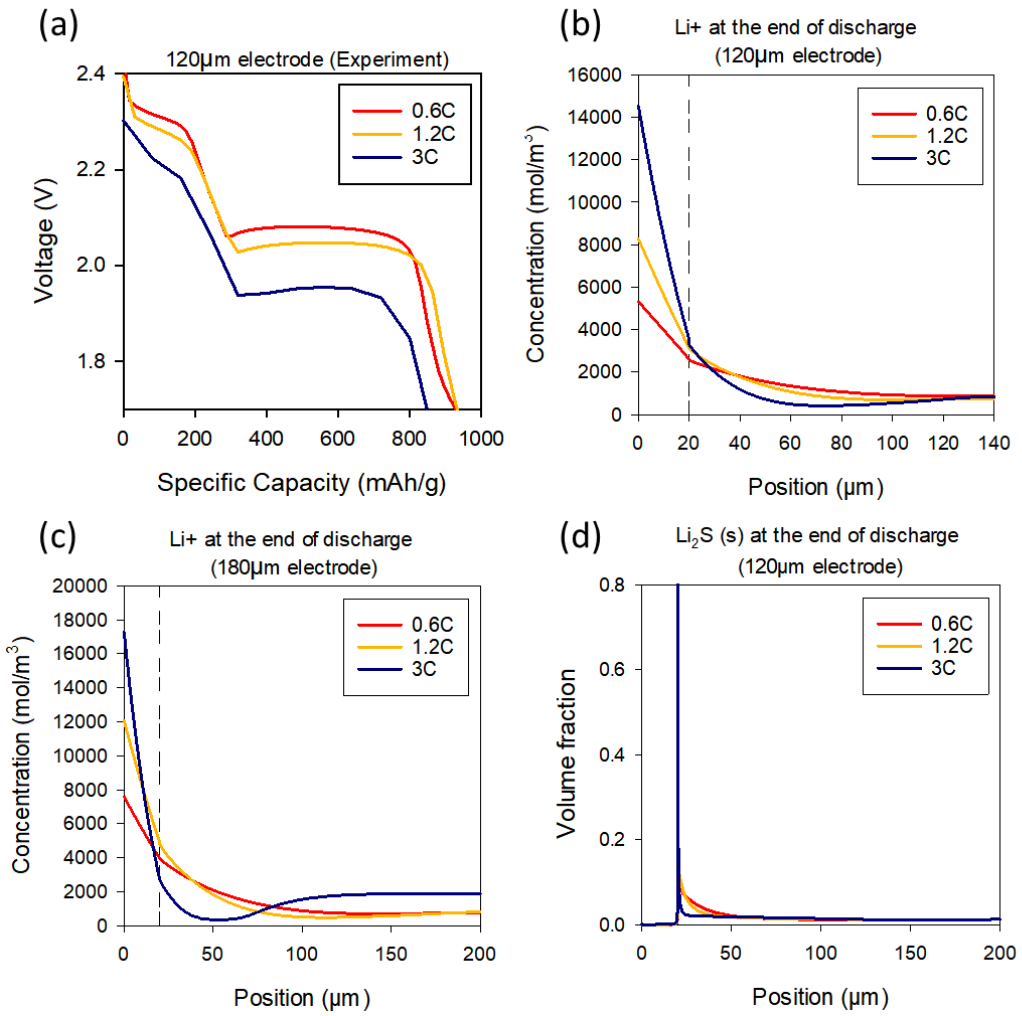

Figure 35 (a) Experiment outcome of c-rate performance for 120µm cathode, lithium ion concentration profile at the end of discharge for (b) 120µm cathode and (c) 180µm cathode, Li_2S solid deposition at the end of discharge.

REFERENCES

1. L. Sun, M. Li, Y. Jiang, W. Kong, K. Jiang, J. Wang and S. Fan, *Nano Letters*, 2014, **14**, 4044-4049.
2. K. Jiang, J. Wang, Q. Li, L. Liu, C. Liu and S. Fan, *Advanced Materials*, 2011, **23**, 1154-1161.
3. K. Liu, Y. Sun, L. Chen, C. Feng, X. Feng, K. Jiang, Y. Zhao and S. Fan, *Nano Letters*, 2008, **8**, 700-705.
4. J. Guo, Y. Xu and C. Wang, *Nano Letters*, 2011, **11**, 4288-4294.
5. G. Yang, J. Tan, H. Jin, Y. H. Kim, X. Yang, D. H. Son, S. Ahn, H. Zhou and C. Yu, *Advanced Functional Materials*, 2018, **28**, 1800595.
6. K. Jin, X. Zhou, L. Zhang, X. Xin, G. Wang and Z. Liu, *The Journal of Physical Chemistry C*, 2013, **117**, 21112-21119.
7. J. Yang, J. Xie, X. Zhou, Y. Zou, J. Tang, S. Wang, F. Chen and L. Wang, *The Journal of Physical Chemistry C*, 2014, **118**, 1800-1807.
8. Y. Zhao, F. Yin, Y. Zhang, C. Zhang, A. Mentbayeva, N. Umirov, H. Xie and Z. Bakenov, *Nanoscale Research Letters*, 2015, **10**, 450.
9. J. W. Kim, H. Jeon and J. Lee, *The Journal of Physical Chemistry C*, 2018, **122**, 23045-23052.
10. S. Deng, Y. Yan, L. Wei, T. Li, X. Su, X. Yang, Z. Li and M. Wu, *ACS Applied Energy Materials*, 2019, **2**, 1266-1273.

11. D. Chen, X.-Y. Yue, X.-L. Li, J. Bao, Q.-Q. Qiu, X.-J. Wu, X. Zhang and Y.-N. Zhou, *ACS Applied Materials & Interfaces*, 2020, **12**, 2354-2361.

12. Y. Yang, Y. Zhong, Q. Shi, Z. Wang, K. Sun and H. Wang, *Angewandte Chemie International Edition*, 2018, **57**, 15549-15552.

13. X. Liang, C. Hart, Q. Pang, A. Garsuch, T. Weiss and L. F. Nazar, *Nature Communications*, 2015, **6**, 5682.

14. G. Li, X. Wang, M. H. Seo, M. Li, L. Ma, Y. Yuan, T. Wu, A. Yu, S. Wang, J. Lu and Z. Chen, *Nature Communications*, 2018, **9**, 705.

15. J. Song, T. Xu, M. L. Gordin, P. Zhu, D. Lv, Y.-B. Jiang, Y. Chen, Y. Duan and D. Wang, *Advanced Functional Materials*, 2014, **24**, 1243-1250.

16. J. Song, Z. Yu, M. L. Gordin and D. Wang, *Nano Letters*, 2016, **16**, 864-870.

17. X. Liang, C. Y. Kwok, F. Lodi-Marzano, Q. Pang, M. Cuisinier, H. Huang, C. J. Hart, D. Houtarde, K. Kaup, H. Sommer, T. Brezesinski, J. Janek and L. F. Nazar, *Advanced Energy Materials*, 2016, **6**, 1501636.

18. Z. Li, C. Zhou, J. Hua, X. Hong, C. Sun, H.-W. Li, X. Xu and L. Mai, *Advanced Materials*, 2020, **32**, 1907444.

19. Z. Yuan, H.-J. Peng, T.-Z. Hou, J.-Q. Huang, C.-M. Chen, D.-W. Wang, X.-B. Cheng, F. Wei and Q. Zhang, *Nano Letters*, 2016, **16**, 519-527.

20. F. Y. Fan and Y.-M. Chiang, *Journal of The Electrochemical Society*, 2017, **164**, A917-A922.

21. J. Ren, Y. Huang, H. Zhu, B. Zhang, H. Zhu, S. Shen, G. Tan, F. Wu, H. He, S. Lan, X. Xia and Q. Liu, *Carbon Energy*, 2020, **2**, 176-202.

22. Y. Mao, G. Li, Y. Guo, Z. Li, C. Liang, X. Peng and Z. Lin, *Nature Communications*, 2017, **8**, 14628.

23. H. B. Wu, S. Wei, L. Zhang, R. Xu, H. H. Hng and X. W. Lou, *Chemistry – A European Journal*, 2013, **19**, 10804-10808.

24. O. Shekhah, J. Liu, R. A. Fischer and C. Wöll, *Chemical Society Reviews*, 2011, **40**, 1081-1106.

25. J. Zhou, R. Li, X. Fan, Y. Chen, R. Han, W. Li, J. Zheng, B. Wang and X. Li, *Energy & Environmental Science*, 2014, **7**, 2715-2724.

26. J. Zhou, X. Yu, X. Fan, X. Wang, H. Li, Y. Zhang, W. Li, J. Zheng, B. Wang and X. Li, *Journal of Materials Chemistry A*, 2015, **3**, 8272-8275.

27. J. Zheng, J. Tian, D. Wu, M. Gu, W. Xu, C. Wang, F. Gao, M. H. Engelhard, J.-G. Zhang, J. Liu and J. Xiao, *Nano Letters*, 2014, **14**, 2345-2352.

28. J. Lee, J. H. Kwak and W. Choe, *Nature Communications*, 2017, **8**, 14070.

29. X. Zhu, F. Zhang, L. Zhang, L. Zhang, Y. Song, T. Jiang, S. Sayed, C. Lu, X. Wang, J. Sun and Z. Liu, *Advanced Functional Materials*, 2018, **28**, 1705015.

30. X. Ni, T. Qian, X. Liu, N. Xu, J. Liu and C. Yan, *Advanced Functional Materials*, 2018, **28**, 1706513.

31. J. Sun, Y. Sun, M. Pasta, G. Zhou, Y. Li, W. Liu, F. Xiong and Y. Cui, *Advanced Materials*, 2016, **28**, 9797-9803.

32. W. Chen, T. Qian, J. Xiong, N. Xu, X. Liu, J. Liu, J. Zhou, X. Shen, T. Yang, Y. Chen and C. Yan, *Advanced Materials*, 2017, **29**, 1605160.

33. J. Liu, T. Qian, M. Wang, X. Liu, N. Xu, Y. You and C. Yan, *Nano Letters*, 2017, **17**, 5064-5070.

34. J. Liu, T. Qian, M. Wang, J. Zhou, N. Xu and C. Yan, *Nano Letters*, 2018, **18**, 4598-4605.

35. Q. Pang, X. Liang, C. Y. Kwok, J. Kulisch and L. F. Nazar, *Advanced Energy Materials*, 2017, **7**, 1601630.

36. Z. W. Seh, Y. Sun, Q. Zhang and Y. Cui, *Chemical Society Reviews*, 2016, **45**, 5605-5634.

37. J. Nelson, S. Misra, Y. Yang, A. Jackson, Y. Liu, H. Wang, H. Dai, J. C. Andrews, Y. Cui and M. F. Toney, *Journal of the American Chemical Society*, 2012, **134**, 6337-6343.

38. S. Waluś, C. Barchasz, R. Bouchet, J.-C. Leprêtre, J.-F. Colin, J.-F. Martin, E. Elkaïm, C. Baehtz and F. Alloin, *Advanced Energy Materials*, 2015, **5**, 1500165.

39. J.-J. Chen, R.-M. Yuan, J.-M. Feng, Q. Zhang, J.-X. Huang, G. Fu, M.-S. Zheng, B. Ren and Q.-F. Dong, *Chemistry of Materials*, 2015, **27**, 2048-2055.

40. N. Xu, T. Qian, X. Liu, J. Liu, Y. Chen and C. Yan, *Nano Letters*, 2017, **17**, 538-543.

41. J.-H. Tian, T. Jiang, M. Wang, Z. Hu, X. Zhu, L. Zhang, T. Qian and C. Yan, *Small Methods*, 2020, **4**, 1900467.

42. C. Arneson, Z. D. Wawrzyniakowski, J. T. Postlewaite and Y. Ma, *The Journal of Physical Chemistry C*, 2018, **122**, 8769-8779.

43. J. C. Burgos, P. B. Balbuena and J. A. Montoya, *The Journal of Physical Chemistry C*, 2017, **121**, 18369-18377.

44. S. Perez Beltran and P. B. Balbuena, *ChemSusChem*, 2018, **11**, 1970-1980.

45. G. Zheng, Q. Zhang, J. J. Cha, Y. Yang, W. Li, Z. W. Seh and Y. Cui, *Nano Letters*, 2013, **13**, 1265-1270.

46. Z. W. Seh, Q. Zhang, W. Li, G. Zheng, H. Yao and Y. Cui, *Chemical Science*, 2013, **4**, 3673-3677.

47. W. Li, Q. Zhang, G. Zheng, Z. W. Seh, H. Yao and Y. Cui, *Nano Letters*, 2013, **13**, 5534-5540.

48. Z. W. Seh, J. H. Yu, W. Li, P.-C. Hsu, H. Wang, Y. Sun, H. Yao, Q. Zhang and Y. Cui, *Nature Communications*, 2014, **5**, 5017.

49. D. Rao, Y. Wang, L. Zhang, S. Yao, X. Qian, X. Xi, K. Xiao, K. Deng, X. Shen and R. Lu, *Carbon*, 2016, **110**, 207-214.

50. X. Yao, J. Xu, Z. Hong, G. Li, X. Wang, F. Lu, W. Wang, H. Liu, C. Liang, Z. Lin and W. Wang, *The Journal of Physical Chemistry C*, 2018, **122**, 3263-3272.

51. E. P. Kamphaus and P. B. Balbuena, *The Journal of Physical Chemistry C*, 2016, **120**, 4296-4305.

52. A. Manthiram, Y. Fu, S.-H. Chung, C. Zu and Y.-S. Su, *Chemical Reviews*, 2014, **114**, 11751-11787.

53. Q. Zhang, Y. Wang, Z. W. Seh, Z. Fu, R. Zhang and Y. Cui, *Nano Letters*, 2015, **15**, 3780-3786.

54. G. Kresse and J. Furthmüller, *Physical Review B*, 1996, **54**, 11169-11186.

55. P. E. Blöchl, *Physical Review B*, 1994, **50**, 17953-17979.

56. J. P. Perdew, K. Burke and M. Ernzerhof, *Physical Review Letters*, 1996, **77**, 3865-3868.

57. X. Liang and L. F. Nazar, *ACS Nano*, 2016, **10**, 4192-4198.

58. X. Zhang, Y. Yang and Z. Zhou, *Chemical Society Reviews*, 2020, **49**, 3040-3071.

59. K. Yan, Z. Lu, H.-W. Lee, F. Xiong, P.-C. Hsu, Y. Li, J. Zhao, S. Chu and Y. Cui, *Nature Energy*, 2016, **1**, 16010.

60. Q. Zhang, J. Luan, Y. Tang, X. Ji, S. Wang and H. Wang, *Journal of Materials Chemistry A*, 2018, **6**, 18444-18448.

61. J. Pu, J. Li, K. Zhang, T. Zhang, C. Li, H. Ma, J. Zhu, P. V. Braun, J. Lu and H. Zhang, *Nature Communications*, 2019, **10**, 1896.

62. R. Zhang, X.-B. Cheng, C.-Z. Zhao, H.-J. Peng, J.-L. Shi, J.-Q. Huang, J. Wang, F. Wei and Q. Zhang, *Advanced Materials*, 2016, **28**, 2155-2162.

63. *Advanced Energy Materials*, 2014, **4**.

64. C.-P. Yang, Y.-X. Yin, S.-F. Zhang, N.-W. Li and Y.-G. Guo, *Nature Communications*, 2015, **6**, 8058.

65. R. Mukherjee, A. V. Thomas, D. Datta, E. Singh, J. Li, O. Eksik, V. B. Shenoy and N. Koratkar, *Nature Communications*, 2014, **5**, 3710.

66. L. Liu, Y.-X. Yin, J.-Y. Li, N.-W. Li, X.-X. Zeng, H. Ye, Y.-G. Guo and L.-J. Wan, *Joule*, 2017, **1**, 563-575.

67. H.-K. Kang, S.-G. Woo, J.-H. Kim, S.-R. Lee and Y.-J. Kim, *Electrochimica Acta*, 2015, **176**, 172-178.

68. S.-H. Wang, Y.-X. Yin, T.-T. Zuo, W. Dong, J.-Y. Li, J.-L. Shi, C.-H. Zhang, N.-W. Li, C.-J. Li and Y.-G. Guo, *Adv Mater*, 2017, **29**, 1703729.

69. J. Noh, J. Tan, D. R. Yadav, P. Wu, K. Y. Xie and C. Yu, *Nano Letters*, 2020, **20**, 3681-3687.

70. Y. Deng, H. Lu, Y. Cao, B. Xu, Q. Hong, W. Cai and W. Yang, *Journal of Power Sources*, 2019, **412**, 170-179.

71. S. Matsuda, Y. Kubo, K. Uosaki and S. Nakanishi, *Carbon*, 2017, **119**, 119-123.

72. G. Yang, Y. Li, Y. Tong, J. Qiu, S. Liu, S. Zhang, Z. Guan, B. Xu, Z. Wang and L. Chen, *Nano Letters*, 2019, **19**, 494-499.

73. J. Lang, Y. Jin, X. Luo, Z. Liu, J. Song, Y. Long, L. Qi, M. Fang, Z. Li and H. Wu, *Journal of Materials Chemistry A*, 2017, **5**, 19168-19174.

74. S. Liu, X. Xia, S. Deng, L. Zhang, Y. Li, J. Wu, X. Wang and J. Tu, *Energy Storage Materials*, 2018, **15**, 31-36.

75. A. Wang, X. Zhang, Y.-W. Yang, J. Huang, X. Liu and J. Luo, *Chem*, 2018, **4**, 2192-2200.

76. S. Liu, A. Wang, Q. Li, J. Wu, K. Chiou, J. Huang and J. Luo, *Joule*, 2018, **2**, 184-193.

77. W. Liu, Y. Xia, W. Wang, Y. Wang, J. Jin, Y. Chen, E. Paek and D. Mitlin, *Advanced Energy Materials*, 2019, **9**, 1802918.

78. A. A. Assegie, C. C. Chung, M. C. Tsai, W. N. Su, C. W. Chen and B. J. Hwang, *Nanoscale*, 2019, **11**, 2710-2720.

79. F. Liu, R. Xu, Z. Hu, S. Ye, S. Zeng, Y. Yao, S. Li and Y. Yu, *Small*, 2019, **15**, 1803734.

80. W. Go, M.-H. Kim, J. Park, C. H. Lim, S. H. Joo, Y. Kim and H.-W. Lee, *Nano Letters*, 2019, **19**, 1504-1511.

81. R. Zhang, X.-R. Chen, X. Chen, X.-B. Cheng, X.-Q. Zhang, C. Yan and Q. Zhang, *Angewandte Chemie International Edition*, 2017, **56**, 7764-7768.

82. J. Wang, H. Wang, J. Xie, A. Yang, A. Pei, C.-L. Wu, F. Shi, Y. Liu, D. Lin, Y. Gong and Y. Cui, *Energy Storage Materials*, 2018, **14**, 345-350.

83. G. Róg, W. Kucza and A. Kozłowska-Róg, *The Journal of Chemical Thermodynamics*, 2004, **36**, 473-476.

84. B. Yu, T. Tao, S. Mateti, S. Lu and Y. Chen, *Adv Funct Mater*, 2018, **28**, 1803023.

85. G. Yang, W. Choi, X. Pu and C. Yu, *Energy & Environmental Science*, 2015, **8**, 1799-1807.

86. N. L. Rangel, J. C. Sotelo and J. M. Seminario, 2009, **131**, 031105.

87. D. V. Kosynkin, A. L. Higginbotham, A. Sinitskii, J. R. Lomeda, A. Dimiev, B. K. Price and J. M. Tour, *Nature*, 2009, **458**, 872-876.

88. F. Hao, A. Verma and P. P. Mukherjee, *Journal of Materials Chemistry A*, 2018, **6**, 19664-19671.

89. B. Wu, J. Lochala, T. Taverne and J. Xiao, *Nano Energy*, 2017, **40**, 34-41.

90. J.-N. J. P. r. A. Chazalviel, 1990, **42**, 7355.

91. F. Shi, A. Pei, A. Vailionis, J. Xie, B. Liu, J. Zhao, Y. Gong and Y. Cui, *Proceedings of the National Academy of Sciences*, 2017, **114**, 12138-12143.

92. G. Bieker, M. Winter and P. Bieker, *Physical Chemistry Chemical Physics*, 2015, **17**, 8670-8679.

93. F. Shi, A. Pei, D. T. Boyle, J. Xie, X. Yu, X. Zhang and Y. Cui, *Proceedings of the National Academy of Sciences*, 2018, **115**, 8529-8534.

94. S. S. Zhang, *ACS Applied Energy Materials*, 2018, **1**, 910-920.

95. R. Bhattacharyya, B. Key, H. Chen, A. S. Best, A. F. Hollenkamp and C. P. Grey, *Nature Materials*, 2010, **9**, 504-510.

96. W. Xu, J. Wang, F. Ding, X. Chen, E. Nasybulin, Y. Zhang and J.-G. Zhang, *Energy & Environmental Science*, 2014, **7**, 513-537.

97. Y. Son, T. Lee, B. Wen, J. Ma, C. Jo, Y.-G. Cho, A. Boies, J. Cho and M. De Volder, *Energy & Environmental Science*, 2020, DOI: 10.1039/D0EE02230F.

98. T. Yang, L. Li, F. Wu and R. Chen, *Adv Funct Mater*, 2020, **30**, 2002013.

99. T. Zhou, J. Shen, Z. Wang, J. Liu, R. Hu, L. Ouyang, Y. Feng, H. Liu, Y. Yu and M. Zhu, *Adv Funct Mater*, 2020, **30**, 1909159.

100. Y. An, Y. Tian, H. Wei, B. Xi, S. Xiong, J. Feng and Y. Qian, *Adv Funct Mater*, 2020, **30**, 1908721.

101. X. Zhou, W. Huang, C. Shi, K. Wang, R. Zhang, J. Guo, Y. Wen, S. Zhang, Q. Wang, L. Huang, J. Li, X. Zhou and S. Sun, *ACS Applied Materials & Interfaces*, 2018, **10**, 35296-35305.

102. C. Sun, T. Wu, J. Wang, W. Li, J. Jin, J. Yang and Z. Wen, *Journal of Materials Chemistry A*, 2018, **6**, 19159-19166.

103. Z. Liang, D. Lin, J. Zhao, Z. Lu, Y. Liu, C. Liu, Y. Lu, H. Wang, K. Yan, X. Tao and Y. Cui, *Proceedings of the National Academy of Sciences*, 2016, **113**, 2862.

104. X.-Y. Yue, X.-L. Li, W.-W. Wang, D. Chen, Q.-Q. Qiu, Q.-C. Wang, X.-J. Wu, Z.-W. Fu, Z. Shadike, X.-Q. Yang and Y.-N. Zhou, *Nano Energy*, 2019, **60**, 257-266.

105. L. Liu, Y.-X. Yin, J.-Y. Li, S.-H. Wang, Y.-G. Guo and L.-J. Wan, *Adv Mater*, 2018, **30**, 1706216.

106. J. Chang, J. Shang, Y. Sun, L. K. Ono, D. Wang, Z. Ma, Q. Huang, D. Chen, G. Liu, Y. Cui, Y. Qi and Z. Zheng, *Nat Commun*, 2018, **9**, 4480.

107. C. Niu, H. Pan, W. Xu, J. Xiao, J.-G. Zhang, L. Luo, C. Wang, D. Mei, J. Meng, X. Wang, Z. Liu, L. Mai and J. Liu, *Nat Nanotechnol*, 2019, **14**, 594-601.

108. G. Huang, J. Han, F. Zhang, Z. Wang, H. Kashani, K. Watanabe and M. Chen, *Adv Mater*, 2019, **31**, 1805334.

109. G. Jiang, N. Jiang, N. Zheng, X. Chen, J. Mao, G. Ding, Y. Li, F. Sun and Y. Li, *Energy Storage Materials*, 2019, **23**, 181-189.

110. H. Ye, Z.-J. Zheng, H.-R. Yao, S.-C. Liu, T.-T. Zuo, X.-W. Wu, Y.-X. Yin, N.-W. Li, J.-J. Gu, F.-F. Cao and Y.-G. Guo, *Angewandte Chemie International Edition*, 2019, **58**, 1094-1099.

111. Z. Cao, B. Li and S. Yang, *Adv Mater*, 2019, **31**, 1901310.

112. M. Wan, S. Kang, L. Wang, H.-W. Lee, G. W. Zheng, Y. Cui and Y. Sun, *Nat Commun*, 2020, **11**, 829.

113. J. Kim, J. Lee, J. Yun, S. H. Choi, S. A. Han, J. Moon, J. H. Kim, J.-W. Lee and M.-S. Park, *Adv Funct Mater*, 2020, **30**, 1910538.

114. S. Wu, T. Jiao, S. Yang, B. Liu, W. Zhang and K. Zhang, *Journal of Materials Chemistry A*, 2019, **7**, 5726-5732.

115. P. Zou, Y. Wang, S.-W. Chiang, X. Wang, F. Kang and C. Yang, *Nat Commun*, 2018, **9**, 464.

116. Y. Ma, Y. Gu, Y. Yao, H. Jin, X. Zhao, X. Yuan, Y. Lian, P. Qi, R. Shah, Y. Peng and Z. Deng, *Journal of Materials Chemistry A*, 2019, **7**, 20926-20935.

117. F. Zhao, X. Zhou, W. Deng and Z. Liu, *Nano Energy*, 2019, **62**, 55-63.

118. X. Ke, Y. Cheng, J. Liu, L. Liu, N. Wang, J. Liu, C. Zhi, Z. Shi and Z. Guo, *ACS Applied Materials & Interfaces*, 2018, **10**, 13552-13561.

119. X.-Y. Yue, W.-W. Wang, Q.-C. Wang, J.-K. Meng, X.-X. Wang, Y. Song, Z.-W. Fu, X.-J. Wu and Y.-N. Zhou, *Energy Storage Materials*, 2019, **21**, 180-189.

120. J.-H. Kim, Y.-H. Lee, S.-J. Cho, J.-G. Gwon, H.-J. Cho, M. Jang, S.-Y. Lee and S.-Y. Lee, *Energ Environ Sci*, 2019, **12**, 177-186.

121. T. Dong, J. Zhang, G. Xu, J. Chai, H. Du, L. Wang, H. Wen, X. Zang, A. Du, Q. Jia, X. Zhou and G. Cui, *Energy & Environmental Science*, 2018, **11**, 1197-1203.

122. Y. Liu, D. Lin, Z. Liang, J. Zhao, K. Yan and Y. Cui, *Nat Commun*, 2016, **7**, 10992.

123. J. Bae, Y. Qian, Y. Li, X. Zhou, J. B. Goodenough and G. Yu, *Energ Environ Sci*, 2019, **12**, 3319-3327.

124. Y. He, H. Xu, J. Shi, P. Liu, Z. Tian, N. Dong, K. Luo, X. Zhou and Z. Liu, *Energy Storage Materials*, 2019, **23**, 418-426.

125. X. Shen, Y. Li, T. Qian, J. Liu, J. Zhou, C. Yan and J. B. Goodenough, *Nat Commun*, 2019, **10**, 900.

126. R. Pathak, K. Chen, A. Gurung, K. M. Reza, B. Bahrami, J. Pokharel, A. Baniya, W. He, F. Wu, Y. Zhou, K. Xu and Q. Qiao, *Nat Commun*, 2020, **11**, 93.

127. Y.-C. Yin, Q. Wang, J.-T. Yang, F. Li, G. Zhang, C.-H. Jiang, H.-S. Mo, J.-S. Yao, K.-H. Wang, F. Zhou, H.-X. Ju and H.-B. Yao, *Nat Commun*, 2020, **11**, 1761.

128. J.-Y. Hwang, S.-J. Park, C. S. Yoon and Y.-K. Sun, *Energ Environ Sci*, 2019, **12**, 2174-2184.

129. E. Cha, M. D. Patel, J. Park, J. Hwang, V. Prasad, K. Cho and W. Choi, *Nat Nanotechnol*, 2018, **13**, 337-344.

130. C. Yan, X.-B. Cheng, Y.-X. Yao, X. Shen, B.-Q. Li, W.-J. Li, R. Zhang, J.-Q. Huang, H. Li and Q. Zhang, *Adv Mater*, 2018, **30**, 1804461.

131. M. M. U. Din and R. Murugan, *Scientific Reports*, 2019, **9**, 16795.

132. C. Fu, V. Venturi, J. Kim, Z. Ahmad, A. W. Ells, V. Viswanathan and B. A. Helms, *Nature Materials*, 2020, **19**, 758-766.

133. T. Xu, P. Gao, P. Li, K. Xia, N. Han, J. Deng, Y. Li and J. Lu, *Advanced Energy Materials*, 2020, **10**, 1902343.

134. P. Albertus, S. Babinec, S. Litzelman and A. Newman, *Nature Energy*, 2018, **3**, 16-21.

135. P. Zou, S.-W. Chiang, H. Zhan, Y. Sui, K. Liu, S. Hu, S. Su, J. Li, F. Kang and C. Yang, *Advanced Functional Materials*, 2020, **30**, 1910532.

136. P. C. Howlett, N. Brack, A. F. Hollenkamp, M. Forsyth and D. R. MacFarlane, *Journal of The Electrochemical Society*, 2006, **153**, A595.

137. R. L. C. Akkermans, N. A. Spenley and S. H. Robertson, *Molecular Simulation*, 2013, **39**, 1153-1164.

138. E. Lee and K. A. Persson, *Nano Lett*, 2012, **12**, 4624-4628.

139. G. Kresse and J. Hafner, *Physical Review B*, 1993, **47**, 558-561.

140. G. Kresse and J. Hafner, *Physical Review B*, 1994, **49**, 14251-14269.

141. G. Kresse and J. Furthmüller, *Computational Materials Science*, 1996, **6**, 15-50.

142. S. Grimme, J. Antony, S. Ehrlich and H. Krieg, *The Journal of Chemical Physics*, 2010, **132**, 154104.

143. H. J. Monkhorst and J. D. Pack, *Physical Review B*, 1976, **13**, 5188-5192.

144. S. L. Dudarev, G. A. Botton, S. Y. Savrasov, C. J. Humphreys and A. P. Sutton, *Physical Review B*, 1998, **57**, 1505-1509.

145. A. L. Dzubak, C. Mitra, M. Chance, S. Kuhn, G. E. JellisonJr., A. S. Sefat, J. T. Krogel and F. A. Reboredo, *The Journal of Chemical Physics*, 2017, **147**, 174703.

146. Q. Pang, A. Shyamsunder, B. Narayanan, C. Y. Kwok, L. A. Curtiss and L. F. Nazar, *Nature Energy*, 2018, **3**, 783-791.

147. Y. Diao, K. Xie, S. Xiong and X. Hong, *Journal of The Electrochemical Society*, 2012, **159**, A421-A425.

148. G. Li, S. Wang, Y. Zhang, M. Li, Z. Chen and J. Lu, *Advanced Materials*, 2018, **30**, 1705590.

149. Z. Li, H. B. Wu and X. W. Lou, *Energy & Environmental Science*, 2016, **9**, 3061-3070.

150. J.-Q. Huang, Q. Zhang and F. Wei, *Energy Storage Materials*, 2015, **1**, 127-145.

151. Q. Li, H. Yang, A. Naveed, C. Guo, J. Yang, Y. Nuli and J. Wang, *Energy Storage Materials*, 2018, **14**, 75-81.

152. H. Wang, B. D. Adams, H. Pan, L. Zhang, K. S. Han, L. Estevez, D. Lu, H. Jia, J. Feng, J. Guo, K. R. Zavadil, Y. Shao and J.-G. Zhang, *Advanced Energy Materials*, 2018, **8**, 1800590.

153. H.-J. Peng, T.-Z. Hou, Q. Zhang, J.-Q. Huang, X.-B. Cheng, M.-Q. Guo, Z. Yuan, L.-Y. He and F. Wei, *Advanced Materials Interfaces*, 2014, **1**, 1400227.

154. S.-Y. Li, W.-P. Wang, H. Duan and Y.-G. Guo, *Journal of Energy Chemistry*, 2018, **27**, 1555-1565.

155. H. Zhang, Z. Zhao, Y. Liu, J. Liang, Y. Hou, Z. Zhang, X. Wang and J. Qiu, *Journal of Energy Chemistry*, 2017, **26**, 1282-1290.

156. R. Xu, Y. Sun, Y. Wang, J. Huang and Q. Zhang, *Chinese Chemical Letters*, 2017, **28**, 2235-2238.

157. Y. Zheng, Y. Yi, M. Fan, H. Liu, X. Li, R. Zhang, M. Li and Z.-A. Qiao, *Energy Storage Materials*, 2019, **23**, 678-683.

158. X. Tao, J. Wang, C. Liu, H. Wang, H. Yao, G. Zheng, Z. W. Seh, Q. Cai, W. Li, G. Zhou, C. Zu and Y. Cui, *Nature Communications*, 2016, **7**, 11203.

159. X. Shang, P. Guo, T. Qin, M. Liu, M. Lv, D. Liu and D. He, *Advanced Materials Interfaces*, 2018, **5**, 1701602.

160. M. Sadd, M. Agostini, S. Xiong and A. Matic, *ChemPhysChem*, 2022, **23**, e202100853.

161. X. Yu, Z. Bi, F. Zhao and A. Manthiram, *ACS Applied Materials & Interfaces*, 2015, **7**, 16625-16631.

162. X. Pu, G. Yang and C. Yu, *Journal of The Electrochemical Society*, 2015, **162**, A1396-A1400.

163. X. Pu, G. Yang and C. Yu, *Advanced Materials*, 2014, **26**, 7456-7461.

164. X. N. Tang, Z. H. Sun, H. C. Yang, H. T. Fang, F. Wei, H. M. Cheng, S. P. Zhuo and F. Li, *JOURNAL OF ENERGY CHEMISTRY*, 2019, **31**, 119-124.

165. X.-L. Fan, L.-Q. Ping, F.-L. Qi, Z. A. Ghazi, X.-N. Tang, R.-P. Fang, Z.-H. Sun, H.-M. Cheng, C. Liu and F. Li, *Carbon*, 2019, **154**, 90-97.

166. Y. Xia, T. S. Mathis, M.-Q. Zhao, B. Anasori, A. Dang, Z. Zhou, H. Cho, Y. Gogotsi and S. Yang, *Nature*, 2018, **557**, 409-412.

167. L. Zhu, W. Zhu, X.-B. Cheng, J.-Q. Huang, H.-J. Peng, S.-H. Yang and Q. Zhang, *Carbon*, 2014, **75**, 161-168.

168. B. Anasori, M. R. Lukatskaya and Y. Gogotsi, *Nature Reviews Materials*, 2017, **2**, 16098.

169. R. Raccichini, A. Varzi, S. Passerini and B. Scrosati, *Nature Materials*, 2015, **14**, 271-279.

170. M. R. Lukatskaya, B. Dunn and Y. Gogotsi, *Nature Communications*, 2016, **7**, 12647.

171. Y. Gogotsi and P. Simon, *Science*, 2011, **334**, 917-918.

172. D. Lv, J. Zheng, Q. Li, X. Xie, S. Ferrara, Z. Nie, L. B. Mehdi, N. D. Browning, J.-G. Zhang, G. L. Graff, J. Liu and J. Xiao, *Advanced Energy Materials*, 2015, **5**, 1402290.

173. M. Hagen, S. Dörfler, P. Fanz, T. Berger, R. Speck, J. Tübke, H. Althues, M. J. Hoffmann, C. Scherr and S. Kaskel, *Journal of Power Sources*, 2013, **224**, 260-268.

174. Z. Yuan, H.-J. Peng, J.-Q. Huang, X.-Y. Liu, D.-W. Wang, X.-B. Cheng and Q. Zhang, *Advanced Functional Materials*, 2014, **24**, 6105-6112.

175. T. Xu, J. Song, M. L. Gordin, H. Sohn, Z. Yu, S. Chen and D. Wang, *ACS Applied Materials & Interfaces*, 2013, **5**, 11355-11362.

176. S. Drvarič Talian, G. Kapun, J. Moškon, A. Vizintin, A. Randon-Vitanova, R. Dominko and M. Gaberšček, *Chemistry of Materials*, 2019, **31**, 9012-9023.

177. L. Chai, J. Wang, H. Wang, L. Zhang, W. Yu and L. Mai, *Nano Energy*, 2015, **17**, 224-232.

178. M.-Q. Zhao, C. E. Ren, Z. Ling, M. R. Lukatskaya, C. Zhang, K. L. Van Aken, M. W. Barsoum and Y. Gogotsi, *Advanced Materials*, 2015, **27**, 339-345.

179. Z. Ling, E. Ren Chang, M.-Q. Zhao, J. Yang, M. Giammarco James, J. Qiu, W. Barsoum Michel and Y. Gogotsi, *Proceedings of the National Academy of Sciences*, 2014, **111**, 16676-16681.

180. J. Luo, W. Zhang, H. Yuan, C. Jin, L. Zhang, H. Huang, C. Liang, Y. Xia, J. Zhang, Y. Gan and X. Tao, *ACS Nano*, 2017, **11**, 2459-2469.

181. T. Zhang, M. Marinescu, S. Walus and G. J. Offer, *Electrochimica Acta*, 2016, **219**, 502-508.

182. K. Kumaresan, Y. Mikhaylik and R. E. White, *Journal of The Electrochemical Society*, 2008, **155**, A576.